Investigation on Light-driven Photocatalyst-based Materials for Wastewater Cleaning and Environmental Remediation

Xia Hua

A thesis submitted to De Montfort University for

the degree of Doctor of Philosophy (PhD)

Institute of Energy and Sustainable Development (IESD)

De Montfort University, Leicester, UK

March 2016

Author's declaration

I declare that the work in this thesis was carried out in accordance with the regulations of De Montfort University. No part of this thesis has been submitted for any other degree or qualification at De Montfort University, or any other academic institutions.

Permission to copy or use whole or part of the work contained herein must be solicited except for the purpose of private study or academic purposes in which case the author must be explicitly acknowledged.

The work contained in this thesis is as a result of my own effort unless otherwise stated.

Signature of author: _____

Xia Hua

Leicester, May 2016

Acknowledgements

I would like to my gratitude to my supervisor team in De Montfort University. Dr Shashi Pual, Head of Emerging Technologies Research Centre (EMTERC), as the first supervisor, giving me valuable suggestions on my research and written works. Dr Xudong Zhao and Dr Yi Zhang, used to belong to Institute of Energy and Sustainable Development (IESD), giving me the opportunity to do this international PhD project. My gratitude also to my oversea supervisor Dr Mindong Chen, who is the dean of School of Environmental Science and Engineering, Nanjing University of Information Science and Technology (NIUST). Thanks to him for the assistant of providing experimental equipment with my research work. I would also like to thank Dr Fei Teng, who offers me the opportunity to work in his group at NIUST, and giving me guidance on research work and scientific paper written.

A specially thank to my dear parents for their support and love throughout all these years.

Thanks again for all my supervisors and colleagues in both De Montfort University and Nanjing University of Information Science and Technology.

Supervisor team: Dr Shashi Paul, Dr Yi Zhang, Dr Xudong Zhao, Dr Mindong Chen (oversea), Dr Fei Teng (oversea).

Abstract

As a promising and green method, wastewater purification techniques based on photocatalyst have received much attention in recent years. However, problems such as low quantum efficiency, limited light responding range and recovery problems limit the further applications of photocatalyst-based materials. In this study, a Ag_3PO_4 photocatalyst with tube-like structure has been synthesized by self-assembly at room temperature. The properties of the catalyst are investigated by scanning electron microscope (SEM), X-ray diffraction (XRD), transmission electron microscope (TEM) and N_2 adsorption-desorption. The photocatalytic activities of the tube-like Ag_3PO_4 are mainly studied by degradations of methyl orange (MO) and rhodamine B (RhB) organic dyes. The effects of pH values and stabilities on photocatalytic performance are studied as well. The results reveal that the tube-like Ag_3PO_4 exhibits greatly high activities for the degradation of RhB solution under acidic condition. The excellent activities of the photocatalyst are due to the small dimension, unique nanostructure and specific surface property. Importantly, Ag_3PO_4 photocatalysts are found with unexpected photocatalytic activity (completion degradation of RhB-MO mixed dyes in 28 h) under natural indoor weak light, of which the light intensity (72 cd) is one in a thousand that of a 300 W Xe lamp ($68.2*10^3$ cd). The degradation of simulated wastewater containing organic dyes and inorganic ions by Ag_3PO_4 under indoor weak light also reveals the potential of Ag_3PO_4 in practical applications of wastewater cleaning and environmental remediation by solar energy-driven photocatalysis.

Table of Contents

INVESTIGATION ON LIGHT-DRIVEN PHOTOCATALYST-BASED MATERIALS FOR WASTEWATER CLEANING AND ENVIRONMENTAL REMEDIATION I

AUTHOR'S DECLARATION I

ACKNOWLEDGEMENTS II

ABSTRACT III

TABLE OF CONTENTS IV

LIST OF FIGURES VII

LIST OF TABLES XII

LIST OF ACRONYMS XIII

CHAPTER 1 OVERVIEW OF THESIS 1

1.1 ORGANIZATION OF THESIS 3

1.2 IMPORTANT OUTCOMES 4

1.3 PUBLICATIONS AND PAPERS IN PREPARATION 6

1.3.1 Publications *6*

1.3.2 Papers in preparation *6*

CHAPTER 2 PHOTOCATALYST-BASED MATERIALS 7

2.1 BACKGROUND OF PHOTOCATALYST 12

2.2 PHOTOCATALYSIS PRINCIPLES 14

2.2.1 Photocatalytic oxidation *14*

2.2.2 Photosensitized oxidation *18*

2.3 SYNTHESIS METHODS 20

2.3.1 Thermal methods *21*

2.3.2 Sol-gel methods *27*

2.3.3 Solid-state reaction *31*

2.4 APPLICATIONS OF PHOTOCATALYSTS 33

2.4.1 Water purification *33*

2.4.2 Self-cleaning *38*

2.4.3 Anti-bacterial *40*

2.5 SUMMARY OF CHAPTER 2 43

CHAPTER 3 SILVER PHOSPHATE PHOTOCATALYSTS 44

3.1 STRUCTURE AND PROPERTIES OF SILVER PHOSPHATE 45

3.2 FACET CONTROL OF SILVER PHOSPHATE 49

3.3 SIZE AND MORPHOLOGY 53

3.3.1 Effect of precipitants *55*

3.3.2 Effect of additives *56*

3.3.3 Templates *57*
3.3.4 Effect of other factors *59*
3.4 MODIFICATIONS OF SILVER PHOSPHATE 60
3.4.1 Metal deposition *61*
3.4.2 Ion doping *64*
3.4.3 Coupling materials *66*
3.4.4 Carbon materials *74*
3.5 SUMMARY OF CHAPTER 3 77

CHAPTER 4 EXPERIMENTAL TECHNIQUES AND ANALYSIS METHODOLOGIES **78**

4.1 PRECIPITATION METHOD 78
4.2 CHARACTERIZATION TECHNIQUES OF PHOTOCATALYST 80
4.2.1 X-ray Diffraction *80*
4.2.2 Scanning electron microscope *82*
4.2.3 Transmission electron microscope *84*
4.2.4 UV-vis spectrum *86*
4.2.5 Nitrogen adsorption-desorption *87*
4.2.6 Thermogravimetric analysis *90*
4.3 PHOTOCATALYSTS USED IN THIS WORK 92
4.4 EVALUATION OF PHOTOCATALYTIC ACTIVITY 94
4.4.1 Evaluation under visible light *95*
4.4.2 Evaluation under natural indoor weak light *97*
4.5 STABILITY TEST 99
4.6 SUMMARY OF CHAPTER 4 100

CHAPTER 5 AG_3PO_4 MICROTUBES WITH IMPROVED PHOTOCATALYTIC PROPERTIES UNDER VISIBLE LIGHT IRRADIATION **101**

5.1 MORPHOLOGY AND PROPERTIES OF SPMS 102
5.1.1 Characterization of SPMs *102*
5.1.2 Formation mechanism of SPMs *108*
5.2 PHOTOCATALYTIC ACTIVITY OF SPMS 110
5.2.1 Individual dye degradation by SPMs *110*
5.2.2 Mixture dye degradation by SPMs *117*
5.3 INFLUENCES OF DOSAGE AND PH VALUE 119
5.3.1 Effect of dosage *119*
5.3.2 Effect of pH on the degradation of individual dyes *121*
5.3.3 Effect of pH values on mixture dye degradation *126*
5.3.4 Stabilities under different pH *128*
5.4 SUMMARY OF CHAPTER 5 132

CHAPTER 6 WASTEWATER CLEANING BY SILVER PHOSPHATE UNDER NATURAL INDOOR WEAK LIGHT **134**

6.1 DEGRADATION OF INDIVIDUAL DYE SOLUTION 134
6.1.1 Under artificial visible light irradiation *135*
6.1.2 Under natural indoor weak light *139*

6.2 DEGRADATION OF MIXED DYE SOLUTION 140
6.2.1 Under visible light irradiation by an artificial Xe lamp *141*
6.2.2 Under natural indoor weak light *142*
6.3 EFFECTS OF INORGANIC SALTS 146
6.4 STABILITIES AND DEGRADATION MECHANISM 150
6.5 SUMMARY OF CHAPTER 6 156
CHAPTER 7 CONCLUSIONS AND SUGGESTIONS FOR FUTURE WORK **158**
7.1 CONCLUSIONS 158
7.2 SUGGESTIONS FOR FUTURE WORK 160
REFERENCE **162**
APPENDICES **181**
APPENDIX A: INDOOR WEAK LIGHT 181
APPENDIX B: PHYSICAL CONSTANTS 181

List of Figures

Fig 2.1 Photocatalytic mechanism and band structure of semiconductor.

Fig 2.2 Photo-reactors: immersion well photo-reactor (left); fluidized bed photo-reactor (right) [76, 77].

Fig 2.3 Dives in Misericordia, Rome [81].

Fig 2.4 Water droplet on ordinary and hydrophobic surfaces [82].

Fig 2.5 Comparison in antialage of photocatalyst properties [84].

Fig 3.1 XRD pattern for standard Ag_3PO_4. Inset: simulated unit cell of Ag_3PO_4 (blue for P, yellow for Ag, red for O).

Fig 3.2 Band structure and redox ability of Ag_3PO_4.

Fig 3.3 Oxygen generation of water by Ag_3PO_4 tetrahedrons, cubes and dodecahedrons under 300W Xe lamp, with the electron scavenger of $AgNO_3$ [94].

Fig 3.4 Ag_3PO_4 prepared by different precipitating agents: (a) Na_3PO_4, pH=12.10; (b) Na_2HPO_4, pH=9.50; (c) NaH_2PO4, pH=4.94 [110].

Fig 3.5 SEM images of Ag3PO4 morphologies: (a) particles [112]; (b) cubes [113]; (c) dodecahedrons [114]; (d) branches [111]; (e) tetrahedrals [109]; (f) tetrapods [115]

Fig 3.6 Schematic illustration of the preparation of Ag3PO4 polyhedrons by using different seeds [106].

Fig 3.7 SEM images of Ag/Ag_3PO_4 composites prepared with different amounts of ammonia: (a) 0.01 M, (b) 0.005 M, (c) none. (d) Schematic illustration of the preparations of Ag/Ag_3PO_4 with different morphologies. [135]

Fig 3.8 Band structure of Bi-Ag3PO4 (A) and density of states of Bi atom (B). [131]

Fig 4.1 Schematic illustration of the SEM work mechanism.

Fig 4.2 Schematic illustration of the TEM work mechanism.

Fig 4.3 SEM images of the as-prepared Ag_3PO_4 samples: (a) Dendrites; (b) Tetrapods; (c) Microtubes and (d) Dodecahedrons.

Fig 4.4 Degradation of MO over Ag_3PO_4 by visible light irradiation

Fig 4.5 Schematic illustration of reaction device for evaluation of photocatalytic activity under visible light.

Fig 4.6 Diagrammatic sketch of natural indoor weak light degradation of simulated wastewater by Ag_3PO_4.

Fig 5.1 XRD patterns (a) and SEM images of the silver phosphate porous microtubes (SPMs) (b) low magnification with an inset; (c, d) high magnification.

Fig 5.2 SPMs after calcination, Inset: image with high magnification.

Fig 5.3 SPMs after ultrasonic treatment at different times: (a) 5 h, (b) 10 h.

Fig 5.4 Nitrogen ad-desorption curves of SPMs.

Fig 5.5 Structure and surface property of SPMs: (a) TEM image; (b) HRTEM image; (c) SAED image

Fig 5.6 Schematic formation diagram of SPMs.

Fig 5.7 Degradation and kinetic curves of organic dyes by SPMs, tetrapods, solid Ag_3PO_4 and P25 powder under visible light irradiation($\geq$420 nm): RhB (a, b); MO (c, d)

Fig 5.8 Schematic diagram of light scattering of the SPMs (a), UV-vis diffuse

reflectance spectra (UV-DRS) of the SPMs and solid Ag_3PO_4 (b) and Tauc plot curve of the SPMs (c).

Fig 5.9 Molecular structures of RhB (left) and MO (right).

Fig 5.10 Thermogravimetric curves of Ag_3PO_4 tetrapods and SPMs range from 50 to 700 ºC.

Fig 5.11 Mixed dye degradation by SPMs under visible light irradiation (>420 nm): (a) RhB; (b) MO.

Fig 5.12 Degradation efficiency of RhB and MO with different catalyst dosages in 10 min.

Fig 5.13 Degradation and apparent kinetic curves of RhB and MO by the SPMs: (a, b) RhB; (c, d)MO.

Fig 5.14 UV-vis absorption spectra of RhB (a) and MO (b) at different pH values: 1, 7 and 12.

Fig 5.15 Degradation curves of RhB with different amounts of DMSO: (a) pH=7; (b) pH=1.

Fig 5.16 Degradation and apparent kinetic curves of RhB-MO mixture solution over Ag_3PO_4: (a, b) pH= 1, (c,d) pH=7, (e, f) pH= 12.

Fig 5.17 Adsorption of RhB-MO mixture solution by SPMs in 30 min.

Fig 5.18 Degradation curves of RhB by the SPMs for 5 cycles under different pH values (a) pH=1, (b) pH=7, (c) pH=12 and XRD patterns of the recovered SPMs (d).

Fig 6.1 Degradation curves and reaction kinetic curves of individual dye over Ag_3PO_4 dendrites (X1), microtubes (X2), tetrapods (X3) and dodecahedrons (X4) under visible light irradiation (≧420 nm): (a,b) Rhodamine B (RhB); (c,d) Methyl orange

(MO).

Fig 6.2 Degradation curves and reaction kinetic curves of individual dye over Ag_3PO_4 dendrites (X1), microtubes (X2), tetrapods (X3) and dodecahedrons (X4) under indoor weak daylight: (a,b) RhB; (c,d) MO.

Fig 6.3 UV-vis absorption spectra of RhB/MO mixture dyes at different irradiation times over Ag_3PO_4 samples under visible light irradiation (≧420 nm): (a) Dendrites; (b) Tetrapods; (c) Microtubes; (d) Dodecahedrons.

Fig 6.4 UV-vis absorption spectra of RhB/MO mixture dyes over Ag_3PO_4 samples under natural indoor weak daylight: (a) Dendrites; (b) Tetrapods; (c) Microtubes; (d) Dodecahedrons.

Fig 6.5 Absorption spectra of RhB/MO mixture dyes solutions containing different inorganic salts over Ag_3PO_4 dendrites under artificial visible light (Xe lamp) (≧420 nm): (a) KCl; (b) K_2SO_4; (c) $BaCl_2$; (d) $Ba(NO_3)_2$.

Fig 6.6 Degradation of mixture dye solution with the addition of $K_2Cr_2O_7$ by X1 under Xe lamp irradiation (≧420 nm).

Fig 6.7 (a) Degradation curves of RhB by Ag_3PO_4 dendrites for 5 cycles under weak daylight (24 h for each run) and artificial visible light (10 min for each run) (≧420 nm); (b) X-ray diffraction (XRD) patterns of Ag_3PO_4 dendrites (X1) and tetrapods (X3) after reactions under natural indoor weak daylight and Xe lamp (≧420 nm).

Fig 6.8 Absorption spectra of RhB/MO mixture dyes over Ag_3PO_4 at night (a light density of 28 cd): (a) Fresh Ag_3PO_4 dendrites; (b) Ag/Ag_3PO_4.

Fig 6.9 SEM images of Ag_3PO_4 samples collected after reactions under natural indoor

weak light (a-d) and artificial Xe light source (e-h): (a,e) X1; (b,f) X2; (c,g) X3; (d,h) X4.

Fig 6.10 Degradation curves of RhB and MO with additions of scavengers ($Na_2C_2O_4$ for trapping hole and DMSO for trapping hydroxyl radical) by Ag_3PO_4 photocatalyst under visible light (a, b) and indoor weak daylight (c, d).

List of Tables

Table 2.1 Different photo-reactors for water cleaning and their advantages.

Table 3.1 Raw materials (additives) and sizes of Ag_3PO_4 crystals with different morphologies.

Table 3.2 Band structures of semiconductors coupled with Ag_3PO_4

Table 5.1 Degradation efficiency of RhB and MO by Ag_3PO_4 dendrites at pH values of 1, 7 and 12

Table 6.1 Zeta potential measurements of the samples at pH 6 (which is the pH value of solution used in degradation process)

Table 6.2 Inorganic ions concentrations in 200 mL RhB/MO mixture solutions containing KCl, K_2SO_4, $BaCl_2$, $Ba(NO_3)_2$ and $K_2Cr_2O_7$

List of Acronyms

Ag	Silver
Ag (I)	Silver Ion
Ag_2O	Silver Oxide
AOPs	Advanced Oxidation Processes
$AgNO_3$	Silver Nitrate
Ag_3PO_4	Silver phosphate
$BaSO_4$	Barium sulfate
BiOCl	Bismoclite
BiOI	Bismuth iodide
$BiPO_4$	Bismuth Phosphate
Cd	Cadmium
CdS	Cadmium Sulfide
C_3N_4	Carbon Nitride
CO_2	Carbon Dioxide
DRS	Diffused Reflection Spectra
EC	European Community
Fe_2O_3	Ferric oxide
g-C_3N_4	graphite-like Carbon Nitride
H^+	Hydrion
H_2	Hydrogen
H_2O	Water

HRTEM	High-resolution Transmission Electron Microscope
Ir	Iridium
MO	Methyl Orange
N_2	Nitrogen
NaOCl	Sodium Hypochlorite
NOx	Nitrogen oxide
Na_2HPO_4	Disodium hydrogen phosphate
O_2	Oxygen
$O_2^{\bullet-}$	Superoxide Anion
OH^-	Hydroxyl
$OH^\bullet$	Hydroxyl radical
PCO	Photocatalytic Oxidation
PEG	Polyethylene Glycol
Pt	Platinum
P25	Degussa P25 Powder
PO_4^{3-}	Phosphate radical
RhB	Rhodamine B
SAED	Selective Area Electron Diffraction
SEM	Scanning Electron Microscope
SO_2	Sulfur Dioxide
SPMs	Silver phosphate Microtubes
SPR	Surface Plasmon Resonance

TEM	Transmission Electron Microscope
TiO_2	Titanium dioxide
UV	Ultraviolet
UV-A	Ultraviolet A
UV-C	Ultraviolet C
VOCs	Volatile Organic Compounds
XRD	X-ray Diffraction
TGA	Thermogravimetry Analysis

Chapter 1 Overview of Thesis

This thesis describes the research background, principles, preparation methods and current applications of photocatalyst-based materials, particularly silver phosphate. The development and research status of silver phosphate have been reviewed. And a tube-like silver phosphate photocatalyst has been prepared in an attempt to enhance the photocatalytic performance of silver phosphate via morphology control. Contaminants oxidation by photocatalysis has been an attractive issue in the past decades due to its low cost, high efficiency, high stability and strong oxidizing power [1-3]. Currently, there is a demand for a catalyst which can cope with all these advantages and can be utilized entirely by natural sunlight. Silver phosphate is one of the most promising photocatalyst to meet with the requirement. Therefore, experiments and evaluations are necessary to demonstrate that silver phosphate can be applied in wastewater treatment as an efficient light-driven catalyst, thereby providing a method to solve environmental issues caused by industrial wastewater discharge.

It has been demonstrated [4] that silver phosphate is one of the most efficient photocatalyst due to its high quantum efficiency, strong oxidizing power and visible light response. To fulfill the requirements of practical applications in industrial utilization, the photocatalytic performance of silver phosphate needs to be further improved. Morphology control is considered to be an effective strategy for the development of nanomaterials attributed to that morphology and nanostructure can significantly affect the properties of materials such as exposed planes, surface area,

conductivity and reactivity [5-7]. A suitable morphology or nanostructure can endow a material with advanced properties in comparison with the same material in irregular structure. Hence, an ideal morphology is necessary for silver phosphate to further enhance its photocatalytic efficiency. As it is known, silver salts are unstable by heating or exposure to light irradiation [8]. However, the stability of silver phosphate has not been systematically studied yet. The effects of light irradiation density, nanostructure and pH value on the stability of silver phosphate during photocatalytic reaction should be investigated. Otherwise, the high quantum yields of silver phosphate endow it with high utilization efficiency of light energy for oxidation process [9-11]. It has possibility to apply silver phosphate in oxidation reaction by entirely using natural solar energy. Hence, degradations of simulated wastewater containing organic dyes and inorganic ions by silver phosphate under indoor weak light are performed in this work to evaluate the possibility of applying silver phosphate in natural light energy-driven industrial wastewater cleaning.

In this thesis, a silver phosphate photocatalyst with tube-like structure has been synthesized by self-assembly at room temperature. The properties of the catalyst were investigated by scanning electron microscope (SEM), X-ray diffraction (XRD), transmission electron microscope (TEM) and N_2 adsorption-desorption. It was found polyethylene glycol 200 (PEG 200) as a solvent played an important role in the crytal growth process, as well as the formation of the hollow structure. The photocatalytic activities of the tube-like silver phosphate were mainly studied by degradations of rhodamine B (RhB), methyl orange (MO) organic dyes and their mixture solution.

The effects of pH values on organic dyes degradation efficiency were studied. And the photocatalytic acitivty and stability of silver phosphate under acidic, neutral and alkaline conditions are studied as well. Importantly, silver phosphate was found with unexpected photocatalytic degradation efficiency for RhB, MO and RhB-MO mixture dye solution under natural indoor weak light, without any artificial light source. Moreover, influences of inorganic ions on the degradation of wastewater containing organic dyes by silver phosphate have been investigated. The stability of silver phosphate under natural indoor weak light was studied by comparing with that under a 300 W Xe lamp.

1.1 Organization of thesis

The thesis is divided into 7 chapters, containing the history, theory, synthesis, experiments, characterization and results of this work. Apart from this overview chapter, the rest chapters are briefly introduced as follows:

Chapter 2 introduces the research background, theory, functions and methodology of photocatalyst. The photocatalysis principles and synthesis methods of materials are explained. The current applications of photocatalyst and their limitations are presented.

Chapter 3 Silver phosphate, the material mainly investigated in this thesis, is introduced in this chapter. The structure, properties, methodology and previous work of silver phosphate are reviewed.

In Chapter 4, the preparation method of silver phosphate used in this work is

presented, as well as the experimental techniques used for characterizations. The test methods and conditions are explained here.

Chapter 5 presents a systematic investigation on the self-assembly tube-like silver phosphate, including the morphology, formation mechanism, effects of pH values and stabilities of the material.

Chapter 6 presents the degradation of wastewater containing organic dyes by silver phosphate under either visible light or natural indoor weak light. The influence of inorganic ions on degradation efficiency is studied. The stability of silver phosphate is investigated by comparing sample property before and after photo reaction.

Finally, chapter 7 gives conclusions of this work and preparations for future work in this area.

1.2 Important outcomes

In this work, silver phosphate porous microtubes have been synthesized using a facile precipitation method at room temperature. The formation of the porous hollow structure was attributed to the utilization of PEG 200. A possible explanation for the formation mechanism of the microtubes was given. SEM and TEM revealed the porous hollow structure of sample, and the fact that the microtubes further consist of a large number of nanoparticles with an average diameter of 100 nm. The results of the photocatalytic activity evaluation have demonstrated that under visible light irradiation, the silver phosphate microtubes exhibit excellent performance for organic

dyes (9 minutes for 10 mg L^{-1} rhodamine B solution) degradation due to its unique morphology. It was also found that the silver phosphate microtubes favor for the degradation of cationic dye due to the specific surface property. Furthermore, degradations of organic dyes were conducted under different pH values. Acidic condition was confirmed that favors for the degradation of dyes by silver phosphate. And stability of silver phosphate is preferable under neutral condition.

Although some photocatalysts (e.g. TiO_2 thin film) have been applied to wastewater cleaning, the degrading efficiency is fairly low. Moreover, there is a need for artificial light source to supply sustained UV light, which increases the expense and energy consumption. In this work, silver phosphate was designed as an effective photocatalyst utilized for industrial wastewater (mainly eliminated from dyeing industries) purification due to its super-high photocatalytic activity. Importantly, organic dyes were found that can be effectively degraded by silver phosphate photocatalyst under natural weak light in an indoor environment, without artificial light source. Under indoor weak light, rhodamine B, methyl orange and their mixture were completely degraded by silver phosphate in 24, 24 and 28 hours, respectively. The influences of inorganic salts on dyes degradation were investigated, contributing to the industrial wastewater purification. The results obtained have brought a step close to the practical wastewater cleaning by using solar energy via photocatalyst-based materials.

1.3 Publications and papers in preparation

1.3.1 Publications

- "Interesting porous Ag_3PO_4 microtubes with improved photocatalytic properties" X. Hua, S. Paul, F. Teng, Catalysis Communications, 2014, 52: 49-52. (Impact factor 3.699)

- "A new application of high-efficient silver-salts based photocatalyst under natural indoor weak light for wastewater cleaning" X. Hua, S. Paul, F. Teng, Water Research, 2015, 81:366-374. (Impact factor 5.528)

1.3.2 Papers in preparation

- "Controllable synthesis of silver phosphate photocatalyst with assistance of organic solvents and their growth mechanism" intend to be submitted to Crystal Growth & Design (ACS Publications)

- "Synthesis process of silver phosphate photocatalyst via morphology control: A Review" intend to be submitted to Inorganic Chemistry (ACS Publications)

Chapter 2 Photocatalyst-based materials

Environmental protection has received much attention from different fields since the problems caused by the atmospheric pollution and wastewater discharge affecting not only human beings' daily life but also social development [12-15]. For example, the discharge of industrial wastewater has a significant impact on rivers, lakes and oceans, resulting in damages of ecosystem and drinking water source. The heavy metal ions (e.g. Hg, Cr, Cu) and organics in industrial wastewater may cause a series of diseases even death once drunk by human or animals [16]. Among the different kinds of industrial wastewaters, water containing dyes from textile industries has one of the largest families of organic pollutants. These dyes can be sorted by their structures, such as acidic, basic, azo, diazo, anthroquinone based and metal complex dyes [17]. Most of the dyes are highly visible and toxic, causing non aesthetic appearance and environmental damage. Every year, more than 100000 kinds of dyes ammounting approximately 7×10^5 ton are generated from industrial purposes [18, 19]. 1-20% of these dyes are wasted during the production process and released with wastewater [20-22]. The released dyes are resistant to light, soil and other natural environment due to their stable chemical structures [23, 24]. Thus they can be maintained in the environment for years, even decades, resulting in persistent damage to water system and ecosystem.

As the wastewater decontamination grows in importance, great efforts have been

done to deal with the wastewater problems caused by dyes. In UK, it has been stated that zero synthetic chemicals should be released into the marine environment since 1997 [17]. This law aims to ensure that dye-containing discharge from industries fulfills the required standard before releasing. European Community (EC) regulations are also becoming more and more stringent against dyes discharge problems [25]. To reach the more and more strict standard of industrial discharge, an effective and environmental friendly strategy for wastewater treatment is urgently needed. During the past few decades, different treatment methods for dye-containing wastewater have been developed by scientists. These methods can be classified as physical methods, chemical methods and biological methods. The most used physical methods for dye decolorization are adsorption technologies. The adsorption technique uses a particular material such as activated carbon, peat, silica gel and membranes to adsorb dyes, thereby decolorizing the wastewater [26, 27]. In the past, it used to be an efficient way to remove pollutants from water. However, adsorption of dyes can not absolutely eliminate the damage and risk caused by dyes. Further treatment for dye decomposition is still needed. Moreover, the performance or activity of the used materials would reduce as the reaction time increases. The recovery and regeneration of some materials such as activated carbon with nanosized pores and membranes are very expensive [28]. Some other material such as peat needs long reaction time and is accompanied with high sludge production [29]. Since last century, chemical methods have been employed to deal with industrial wastewaters. Different from physical adsorption, chemical methods can decolorize dyes by destroying the aromatic ring of

the dye molecules. Reagents with strong reducing or oxidizing power are usually used in the traditional chemical methods. The most used reagents are hydrogen peroxide, ozonation and NaOCl [30, 31]. Nevertheless, traditional chemical methods also have disadvantages. For example, fentons reagent generates high sludge due to the aggregation of reagents. The method of incineration is used to deal with the sludge. Although the incineration of sludge can produce electronic power, it also produces atmospheric pollutants due to the incomplete combustion [32]. Oxidation by ozonation is an efficient and suitable method for pollutants degradation. However, the half-life of ozonation is as short as only 20 min. And the regeneration of ozonation is not cost-efficient, limiting its applications in practical wastewater treatment [30]. Utilization of NaOCl can effectively degrade organic polluants by attacking the amino group by the active hypochlorite radical. Anyway, the discharge of chlorine into environment causes pollution, and the by-product of aromatic amines can lead to cancer [33]. Cucurbituril, a cyclic polymer of formaldehyde and glycoluril, is discovered with good sorption capacity for various types of textile dyes. It can form complexes with aromatic rings thereby decolorizing the wastewater [34]. However, the high generation expense of cucurbituril limits its widely application in wastewater treatment. In 1994 [35], decolorization of dyes by white rot fungi was first reported, which is a biological treatment method. White rot fungi can degrade dyes via enzymes, thereby decolorizing the effluent containing dyes. Although this biological method is environmentally friendly and has an acceptable cost, it requires a fermentation process. The duration of the fermentation process depends on various of fungi, temperature

and amount of effluent. When the volume of effluent is too large, the reaction might stop that attribute to the fermentation can not continue. Hence the biological method for dye removal is considered to be less efficient compared with the physical and chemical methods. Up to now, there is not a commercially feasible and effective method to deal with the wastewater problems.

Recent years, advanced oxidation processes (AOPs) have been applied to deal with the wastewater problems, which is a green method to oxidize organic contaminants with strong oxidative radical species [36, 37]. Among the AOPs, photocatalytic technology is one of the most promising strategies for wastewater cleaning which fulfills the aims of environmental friendly and sustainable development. Semiconductor materials could produce photon electron and “hole” on its surface under light irradiation. Water molecules can gain or loose electrons by reacting with the photon electron and “hole” to form hydroxyl radicals or superoxide anion, both of which are powerful oxidative species. The powerful oxidative species could degrade most of organic compounds into water and carbon dioxide which are harmless to environment. Importantly, photocatalysts could absorb and degrade organic pollutants in wastewater and atmosphere only with the assistance of light, namely, solar energy, which is renewable and widely exist in nature. Comparing with traditional wastewater purification methods, the photocatalytic technology has several advantages: a) the degradation efficiency of the photocatalytic processes is extremely high due to the strong redox power of the active species generated by the photocatalyst; b) the photocatalytic process is safe and environmental friendly

attribute to that most photocatalysts are inorganic metal oxides which are nontoxic, and the by-products of the photocatalytic process are much less harmful compared with the traditional methods; c) the photocatalytic processes are energy-efficient due to the use of solar light, which is renewable and abundant; d) most of the photocatalysts can be recycled and reused after the photocatalytic reaction, which fulfills the economic principle of industrial production. Among various oxide semiconductor photocatalysts, titanium dioxide is the most widely used due to its outstanding properties such as rich source, strong oxidizing power and non-toxicity [38-41]. However, in practical applications, the performance of titanium dioxide is unsatisfactory for several reasons. Firstly, the photocatalytic efficiency of titanium is much lower than that in theory due to the high recombination ratio of photon electrons and holes produced by ultraviolet irradiation. Researchers have attempted to solve this problem through complexing, metal doping and deposition on carbons. However, the outcomes indicate that more investigations and methods are still needed. Furthermore, the energy band gap of TiO_2 is 3.02 eV, indicating TiO_2 can be activated by ultraviolet light below 380 nm, of which is only 5% of the solar energy. The low efficiency of light utilization also limits the practical application of TiO_2.

2.1 Background of photocatalyst

Photocatalysts have been investigated by researchers for over 60 years. As the term “photocatalyst” implies, they are substances which can accelerate chemical reactions under the excitation of photons. Chlorophyll is the most common natural photocatalyst in the environment. It can promote the photosynthesis of plants, which transforms water and carbon dioxide into oxygen and carbohydrate. In this way, the organic compounds which are harmful to the environment and human beings can be resolved. Meanwhile, the oxygen and carbohydrate needed by the plants can be manufactured. The known photocatalysts can be mainly classified as four categories including the metal oxides, the metal sulfides, the metal nitrides and the metal phosphides. Among the large family of photocatalysts, titanium dioxide (TiO_2) is the most famous and oldest photocatalyst. As early as 1964, the first work of photocatalytic oxidation of tetralin by a TiO_2 suspension was reported by Kato et al [42]. After that, photocatalytic oxidation of organic compounds by oxygen adsorbed on TiO_2 had drawn attention by researches. However, the most famous event to promote the study of photocatalysis was that the discovery of photocatalytic water splitting by TiO_2, which was reported by Fujishima and Honda in 1972 [43]. In 1986, Fujishima et al. [44] reported tumor cells’ photokilling by TiO_2 particles. In 1991, TiO_2 coated with organic chromophore groups was reported as an efficient solar cell by O’Regan et al. [45]. In 1995, Fujishima et al. [38] discovered the superhydrophilic properties of the TiO_2 films coated with silica under UV light irradiation. Highly hydrophilic TiO_2 surface with excellent anti-fogging and self-cleaning properties was

reported by Wang et al. [46] in 1998. Thus, the functions of water splitting, pollutants degradation, anti-bacterial, solar cell and anti-fogging by TiO_2 have been developed and investigated. After that, Sonawane et al. [47] synthesized TiO_2 films coped with iron which can degrade methyl orange solution under sunlight irradiation in 2004. In the next year, hydrogen generation by mesoporous TiO_2 has been realized, which open a door of energy production by photocatalytic reaction. In 2009, rutile TiO_2 was prepared by Mizukoshi et al. [48] in a sulfuric acid electrolyte. Sulfur doping could reduce the band gap width of TiO_2, which enables photodegradation of organic dye solution under visible light with the wavelength above 420 nm. Degussa P25 was then developed and widely used in industrial application, of which the phase ratio of anatase and rutile is 4:1.

There is no doubt large amounts of investigations on photocatalysts have been done to understand and improve the photocatalytic process over the last five decades. TiO_2 based materials have been well developed to meet needs from different fields. In addition, novel photocatalysts (e.g. bismuth oxides [49], silver phosphate [9] and carbon nitride [50]) with advanced properties and high efficiency are discovered every year, contributing to the widespread applications in the photocatalytic technology. Among such applications, the utilization of photocatalysts in pollutants removal is particularly important. Due to the rapid development of industrialization, the environmental problems caused by industrial pollutants become more and more serious as well. Although relevant laws and standards were promulgated to pretect the environment from industrial pollution, the existing methods for pollutants removal

always come with high costs and low efficiences. The specific advantages of photocatalytic technologies such as nontoxic, stable, inexpensive and reusable make photocatalyst-based materials become the most promising method to protect environment from industrial pollutions.

2.2 Photocatalysis principles

The degradation mechanism of organic pollutants by photocatalyst is introduced in this section. In our understanding, there are mainly two reaction mechanisms in the photocatalytic degradation process, photocatalytic oxidation and photosensitized oxidation. Both of them are discussed here.

2.2.1 Photocatalytic oxidation

Semiconductor materials are different from electric conductors or insulators. Semiconductors have a valence band and a conduction band. The electrons in the valence band can not move into conductive band without passing a certain external energy, namely, the band gap energy. When a semiconductor is irradiated with light energy greater than its band gap energy, conduction band electron and valence band hole are generated. It is worth noting that the free energy of the electron-hole pair is smaller than that of band gap energy. Because a certain amount of energy is comsumed by the conduction band and valence band during the generation of electron-hole pair. The photogenerated electron could reduce molecules or react with electron acceptors such as O_2 adsorbed on semiconductor surface, reducing it into

superoxide radical anion ($O_2^{\bullet-}$). The photogenerated hole could oxidize the organic molecules to form R^+, or react with OH^- or H_2O on semiconductor surface and oxidizing them into $OH^\bullet$ radicals. Both of $O_2^{\bullet-}$ and $OH^\bullet$ radicals have a strong redox power which in response to decompose organic substances such as dyes. The powerful redox ability can degrade organic dyes into harmless compounds of carbon dioxide and water. According to this, the relevant reactions (TiO_2 for example) occuring on semiconductor surface are presented as follows:

$TiO_2 + UV \rightarrow e^- + h^+$ (1)

$h^+ + H_2O \rightarrow H^+ + OH^\bullet$ (2)

$h^+ + OH^- \rightarrow OH^\bullet$ (3)

$e- + O_2 \rightarrow O_2^{\bullet-}$ (4)

$Dye + h^+ \rightarrow$ oxidation products (5)

$Dye + e^- \rightarrow$ reduction products (6)

$Dye + OH^\bullet \rightarrow$ degradation products (7)

When TiO_2 is irradiated with ultraviolet energy, the conduction band and valence band can be activated to generate photo-induced electrons and holes. The hole in the valence band oxidizes hydroxyl and water to form free hydroxyl radical, which is the strongest oxidative species in nature. Otherwise, the photo-induced electron can reduce dissolved oxygen in water to form superoxide anion with strong reducing power. The superoxide could further react with electron to form peroxide, which has strong redox power. The formed superoxide anion can reduce pollutants into some

reduction products, even reduce water into hydrogen, namely, hydrogen production by water splitting. Sometimes pollutants could be directly reduced by photon electrons if the reduction potential of conduction band is high enough. Normally, the free hydroxyl radical is responsible for the oxidation of organic dyes. The oxidative potential of hydroxyl radical is as high as 2.80 V, which can oxidize most of organic substances and even some inorganic compounds. Moreover, some photocatalyst such as Ag_3PO_4 could oxidize organic dyes on its valence band directly by photo-induced hole. Importantly, the reducing and oxidizing power of electrons and holes are determined by the position of conduction band and valence band of the semiconductor. **Fig 2.1** presents the band structure of semiconductor which could help understand the definition of position.

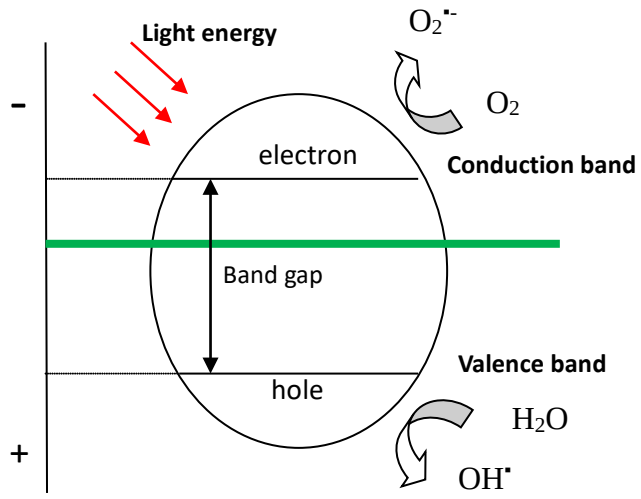

Fig 2.1 Photocatalytic mechanism and band structure of semiconductor.

As it is known, either oxidative reaction or reductive reaction is accompanied with electron transfer. The tendency of a substance gaining or losing electron in a system is known as redox potential of the substance in this system. Normally, the

potential difference between the solution with 1 mol L^{-1} hydrongen ions and a $1*10^5$ PA hydrogen saturation platinum electrode is determined to be zero attributing to that the redox potential is a relative value in different systems. The more positive the potential of a substance compared with the potential of hydrogen ions, the stronger tendency of this substance to loss electron in the system. On the contrast the more negative the potential of a substance compared with the potential of hydrogen ions, the stronger tendency of this substance to acquire electron in the system. The green horizontal line in **Fig. 2.1** stands for oxidation-reduction potential of hydrogen ions. As it is known, the ability of losing and gaining electorn represent the oxidative and reduction power of a substance. Therefore, the conduction band with negative potential means it has the reducing power, while the valence band with positive potential means it has the oxidizing power. The higher the position of conduction band, the stronger reducing power the conduction band and the electron possess. On the contrary, the lower the position of valence band, the stronger oxidizing power the valence band and the hole possess. For example, TiO_2 has a conduction band of -0.50 eV and a valence band of 2.70 eV, while Fe_2O_3 has a conduction band of 0.20 eV and a valence band of 2.30 eV. According to the understanding of redox potential, the conduction band of TiO_2 has stronger oxidative power than that of Fe_2O_3 and the valence of band of TiO_2 has stronger reduction power than that of Fe_2O_3. In a word, the redox potential of a semiconductor is determined by the positions of its conduction and valence band. Specifically, when the conduction band of a semiconductor is below the oxidation-reduction potential of hydrogen, the

semiconductor can not be used in hydrogen production. For example, Ag_3PO_4 has a conduction band of +0.45 eV and valence band of +2.9 eV. Its valence band has an extremely high oxidative power for the degradation of organic pollutants due to the high positive potential. However, the conduction band of Ag_3PO_4 is below the oxidation-reduction potential of hydrogen and with positive potential. Hence it does not possess the ability of hydrogen production.

2.2.2 Photosensitized oxidation

The photosensitized oxidation by visible light (>420 nm) is different from that photocatalytic reaction under ultraviolet irradiation. It is acknowledged that some azo dyes could absorb light with wavelength over 420 nm, namely, visible light. Under light illuminance, some dye molecules can be excited to singlet or triplet states, generating photo induced electrons. The photon electrons transport onto the conduction band of semiconductor, thereby forming the cationic dye radicals ($Dye^{\bullet+}$). The cationic dye radicals react with OH^- in the solution forming $OH^\bullet$ to oxidize the dye molecules. Otherwise, the electrons on the conduction band can form $O_2^{\bullet-}$, then $O_2^{\bullet-}$ react with water to form $HO_2^\bullet$. The cationic dye radicals can also react with $O_2^{\bullet-}$ or $HO_2^\bullet$ to generate intermediates and then finally converted to degradation products. The relevant reactions of photosensitized oxidation (TiO_2 for example) are shown as follows:

$$Dye + TiO_2 + UV/vis \longrightarrow Dye^{\bullet+} + e^- \quad (8)$$

$$Dye^{\bullet+} + OH^- \longrightarrow Dye + OH^\bullet \quad (9)$$

$$Dye + 2OH^{\bullet} \longrightarrow H_2O + \text{oxidation products} \quad (10)$$

$$e^- + O_2 \longrightarrow O_2^{\bullet -} \quad (11)$$

$$O_2^{\bullet -} + H^+ \longrightarrow HO_2^{\bullet} \quad (12)$$

$$Dye^{\bullet +} + HO_2^{\bullet} \longrightarrow \text{intermediates} \longrightarrow \text{degradation products} \quad (13)$$

$$Dye^{\bullet +} + O_2^{\bullet -} \longrightarrow \text{intermediates} \longrightarrow \text{degradation products} \quad (14)$$

The process of photosensitized oxidation is more complex when compared with that of photocatalytic oxidation. Sometime these two oxidation process take place together, making the photocatalytic process even more complicated. When this happen it is hard to say which one takes the domination or is more effective. Methods can be used to find out photosensitized or photocatalytic oxidation processes during the oxidizing process due to their different oxidizing species. Researchers use scavengers to capture certain oxidizing species when the degradation is taking place [51, 52]. For example, sodium oxalate can be used to capture hydroxide radicals in solution. If the degradation rate of dyes does not decrease when adding sodium oxalate, this is an indication that the photosensitized oxidation is dominant, otherwise, the degradation could be attributed to photooxidation. Furthermore, the detection of intermediates during the degradation process is another way to distinguish photo-oxidation from photosensitized oxidation. Comparing the reaction formulas of the two oxidation process, it was found that the degradation by photosensitized oxidation is generally accompanied by some intermediates. These intermediates can be detected by liquid phase mass spectrometry, or they cause a blue shift for the

pollutant peak in its reflectance spectra. However, mass spectrometry and reflectance spectra can not definitively conclude that the degradation of pollutants is ascribed to photo-oxidation or photosensitized oxidation. This is because in some cases, other intermediates emerge during the photo-oxidation process. The length of reaction time could also make a difference between the two oxidation process. As described above, photocatalytic oxidation can occur rapidly once the semiconductor activated by light illuminance. Nevertheless, there is normally a activation duration before the photosensitized oxidation [53]. In the case of photosensitized oxidation, the degradation curve is smooth at the first several minutes/hours, then the degradation rate becomes faster as the time increases. It is difficult to conclude that which of the oxidation pathways is more effective than the other one. But it is undeniable that photosensitized oxidation does increase the oxidizing efficiency in the overall reaction. And the photosensitized oxidation is important for the better utilization of solar energy, especially for some wide band gap semiconductors which can not be activated by visible light.

2.3 Synthesis methods

There are a number of methods to synthesize semiconductors. In this section, several mostly used synthesis methods for photocatalysts are stated, including thermal method, sol-gel method and solid-state method. The mechanisms, reaction conditions and examples of these synthesis techniques are introduced.

2.3.1 Thermal methods

In as early as 1845, researchers have grown quartz in a pressure cooker, opening the door of thermal methods systhesis [54]. Then Bunsen et al. [55] reported the preparation of barium and strontium carbonate under the conditions of 200 ^{o}C and 15 atmospheres. A glass tube was used as container while ammonium chloride was used as a solvent. In 1905, Spezia et al. [56] reported the large crystal (15 mm) by heating sodium silicate and natural crystal in a silver vessel at 320-350 ^{o}C after 200 days. After that, thermal methods have been widely used in the preparation of various minerals. Thermal methods include hydrothermal [57], solvothermal [58], microwave [59], mechano-thermal [60] and seed-hydrothermal [61]. Hydro-solvent thermal methods involve the chemical reaction of substance in aqueous system under appropriate temperature (100-1000 ^{o}C) and pressure (1-100 MPa). Hence a container which can bear high temperature, high pressure and chemical corrosion, e.g. autoclave with polytetrafluoroethene inner tank, is needed for the reagents. The autoclaves are usually steel cylinders with an insert made of carbon-free iron, platinum quartz or Teflon which depends on the required temperature and solution category. Normally, an iron salt and a salt of metal are dissolved in water or organic solvent under stirring and the pH is adjusted due to metal category. The uniform mixture is moved into an autoclave and heated for 12-48 h, then cool down to room temperature. This duration is known as the crystal growth process. The precipitate is collected by centrifugation and washed with deionized water or ethanol, followed by drying for several hours under 60-80 degrees Celsius. For seed-hydrothermal treatment, a seed of metal oxide

takes place of iron salt which mixes with a salt of metal, then placed into clave and use the same procedure described above.

Crystal growth is a major step in the crystallization process of thermal synthesis which involves the reaction and combination of atoms, ions and the formation of crystal lattice. The process of crystal growth can be divided into two stages, the nucleation process and the growth process. Nucleation is the first stage that determines if a new thermodynamic phase can form. When the medium of a system is supersaturated and approach the critical value, random fine nucleus appear and decay continuously due to the balance between different phases. This process will last until an unusual large nucleus appears due to the partial changes of temperature, concentration or impurities. The large nucleus approaches the critical value which is more favourable for its new phase to grow, instead of transforming back to its initial phase. The large nucleus then grows up and goes into the next stage of crystal growth. Anyway, the appearance of large nucleus is also a stochastic process which may not happen if the system is not evolving with time and nucleation occurs in one step. It is like rain droplets would not change into ice below -30 ^{o}C during dropping, even though ice is the stable state for water below 0 ^{o}C. Nucleation can be further classified as heterogeneous nucleation occurring on surface of the system, and homogeneous nucleation occurring away from surface of the system. Heterogeneous nucleation is much more common than homogeneous due to the free energy barrier. Free energy of a system refers to the energy can be used to perform work in this system. The nucleation process will slow the free energy barrier, which caused by the

free energy consumed for the growing of nucleus surface. Under the condition of homogeneous nucleation, nucleus is away from liquid or solid surface so that the free energy barrier is high attributing to that homogeneous nucleus is like a sphere and with large surface area. Otherwise, under the condition of heterogeneous nucleation, the surface area of nucleus is small as well as the free energy barrier. Thus, nucleation is much faster in heterogeneous process than that in homogeneous process. Moreover, owing to the habit of heterogeneous nucleation, the number of nucleus can be controlled. In hydrothermal synthesis, the use of scratched container, seed crystal and template all can provide nucleation sites thereby increasing the number and promoting the growth of nucleus. The nucleus then goes to the next stage of crystal growth. The growth habit of a crystal is dependent on its internal structure. Different internal structures can lead to crystal growth in different directions and form different facets. When the entire surface of a plane reaches equilibrium with a driving force, a lateral growth will happen to the crystal. When the lateral growth happen, the plane can maintain till the equilibrium is broken down. On the other hand, the crystal will advance to other directions instead of lateral growth when the surface can not reach the equilibrium with driving force. Cahn et al. [62] indicated that every surface or interface in a crystalline medium has a critical driving force. A crystal will advance to itself if the driving force in its surface or interface exceeds the critical driving force, while lateral growth will happen if the driving force not exceeds the critical value. For extremely diffuse suface, the critical driving force is very small so that the driving force at surface can easily exceed it, leading to advance growth of crystal. For sharp

surface, the critical driving force is very large so that lateral growth will take place.

Comparing with other synthesis methods, materials prepared via thermal method have the advantages of high crystallinity, structure controllable and less crystal defects. In hydro-solvent thermal synthesis, there is a temperature difference between the upper portion and the lower portion of the autoclave. The temperature difference causes a connection between the top and bottom of the autoclave, taking the saturated solution in high temperature to the low temperature crystallization area. The solution cools down and transports to the bottom, forming a cycle system. In this way, nucleus or seed crystal grow continuously into large size. The reaction condition of thermal methods also favors for investigating the regular pattern of reaction and the structures and properties of products. As it is known, the properties of materials are highly dependent on the preparation conditions such as temperature, pressure, pH value, concentration of metal ions and solvent, reaction duration and category of reagents. In hydro-solvent thermal method reaction, the pH value, concentration of metal ions and solvent can be adjusted by preparation of precursor. Temperature and length of reaction can be controlled by an external heating device. By modifying single reaction condition, the influence of each factor on the crystal growth and properties of samples can be investigated, which is important for preparation of specific material. Importantly, ion product of water under high temperature and high pressure is much higher than that under normal temperature and pressure, indicating that many substances which are insoluble under normal condition can be dissolved in water during the hydrothermal condition. And the solubility of substance is different under

different temperature. Therefore, identical crystals with different structure, size and crystalinity can be obtained by controlling the temperature. Moreover, the hydro-solvent thermal method is particularly suitable for the synthesis of materials which are not stable at their melting point ascribed to the relatively mild environment compared with under air condition. Also, the hydro-solvent thermal method is an ideal method to prepare single crystals with large dimension and high crystalinity. Because long reaction time and gentle heating condition can provide a mild reaction environment, thus suppressing the nucleation process and encouraging the crystal growth. In this way, crystals with large dimension and high crystalinity can be obtained. Overall, the hydro-solvent thermal method is suitable for the preparation of materials with well developed crystalline grain, uniform size distribution and controllable structure. However, the instrument of autoclave is expensive and the nucleation and growth processes can not be observed during the reaction. Hence researchers can only propose a possible nucleation or growth mechanism of the material synthesized by thermal method via analyzing the properties of the reagents.

Under hydro-solvent thermal condition, preparation of materials can be further divided into thermal oxidation, thermal precipitation, thermal composition, thermal reduction, thermal decomposition and thermal crystallization due to different reaction process. These reaction processes are explained as follows:

1) Thermal oxidation: obtain precipitation by oxidizing metal or alloy with water or solvent under high temperature and pressure. For example, the temperature of silicon oxidation is above 800 ^{o}C and the process needs the

participation of H_2O vapor or molecular O_2. The reaction equation is as follows:

$$Si + 2H_2O \rightarrow SiO_2 + 2H_2 \quad (15)$$

$$Si + O_2 \rightarrow SiO_2 \quad (16)$$

2) Thermal precipitation: some compounds are difficult to precipitate under room temperature or pressure. Under thermal condition, precipitation of these compounds could be easily obtained. For example, aluminum ion is difficult to precipitate at room temperature due to its low hydrolysis degree. Under thermal condition, heating will promote the hydrolysis process thereby obtaining the precipitant of aluminum.

3) Thermal compostion: using two or more than two kinds of substances to synthesize another substance by regulating reaction factor between an extremely wide range. Most of the synthesis of metal salts with acid ions (e.g. PO_4^{3-}, WO_4^{2-}, Br^-) via thermal method can be sorted into thermal compostion. For example, Pan et al. [63] reported the synthesis of $BiPO_4$ using $Bi(NO_3)_3 \cdot 5H_2O$ and Na_3PO_4 via a hydrothermal method.

4) Thermal reduction: some metal oxides can be reduced into nano size metal particles by changing the temperature or proper reagents. For example, Fe_2O_3 can be reduced into metallic Fe by CO at 500-800 ^{o}C. CO can be produced by heating $H_2C_2O_4$ of which the decomposition temperature is above150 ^{o}C. By heating Fe_2O_3 and $H_2C_2O_4$ gradually, Fe_2O_3 can be reduced by the CO produced during the decomposition of $H_2C_2O_4$, thereby obtaining metallic

Fe.

5) Thermal decomposition: under thermal condition, some substance can be decomposed into two or more than two compounds by increasing the temperature (e.g. $CaCO_3 \rightarrow CaO + CO_2$). The generated compounds can be separated easily by filtration or dissolution.

2.3.2 Sol-gel methods

In 1846, Ebelmen [64] firstly prepared the gel of tetraethoxysilane by mixing $SiCl_4$ and ethynol in wet air environment. Then Dislich [65] reported a multi-component glass by the hydrolysis of metal alkoxide. Besides, Yoldas et al. [66] have prepared transparent porous alumina film by sol-gel method as well. After that, the sol-gel process is widely used in fabrications of glass, metal oxides and functional ceramic powder. This process involves conversion of monomers into colloidal solution and then integrates into discrete particles or polymer to form a gel-like material. The gel-like material can be transformed into crystal particles or film via different methods of drying, centrifugation or just allow time for sedimentation. In this way, metal ions can be mixed homogeneously at molecular level at the precursor stage, which endows material with specific properties. The crystal category or phase and activity of sample are highly depended on the quality of gel and the sintering time. In case of glassy and ceramic fabrications, typical precursors are metal alkoxides and metal chlorides. The precursor solution can transform into a gel-like network via hydrolysis and polycondensation reactions. The hydrolysis of precursors can be

understood by the equation:

$$X(OY)n+mH_2O \rightarrow X(OH)m(OY)n-m+mYOH \qquad (17)$$

By changing reaction conditions, both of particles and polymers can be obtained. There are two chemical conditions for the hydrolysis and polycondensation reactions of precursors, the base-catalyzed sols and acid-catalyzed sols. Under base-catalzed condition, the particles in gel-like network can grow into colloids, of which the solid particles disperse at different degrees in liquid medium. The stable suspension of colloids favors for the generation of highly ordered microstructure by self-assembly. Otherwise, the acid-catalyzed condition favors for the formation of continuous network of precursor, of which the excellent physical properties are suitable for high performance glass. The remaining liquid in gel of both colloid and polymer can be removed by dring process. An additional thermal treatment is necessary for the obtained solid to enhance the stability and mechanical properties of crystal.

Polymerization is another important process which benefits from sol-gle method. Alkoxides are usually used as precursors because they can react with water by hydrolysis. In the case of $Si(OC_2H_5)_4$ (TEOS), the hydrolysis reaction follows equation 18. If the amount of water increases, the hydrolysis can further proceed to equation 19. And for the complete hydrolysis reaction, intermediate products may form such as $[(OC_2H_5)_2\text{-Si-}(OH)_2]$ or $[(OC_2H_5)_3\text{-Si-OH}]$. The intermediates can be easily linked by Si-O-Si to form a polymer. The polymerization process of an alkoxide can be illustrated by the equation 20.

$Si(OC_2H_5)_4+H_2O \rightarrow HO\text{-}Si(OC_2H_5)_3+HO\text{-}C_2H_5$ (18)

$Si(OC_2H_5)_4+2H_2O \rightarrow SiO_2+ 4(HO\text{-}C_2H_5)$. (19)

$(OC_2H_5)_3\text{-}Si\text{-}OH+HO\text{-}Si\text{-}(OC_2H_5)_3 \rightarrow [(OC_2H_5)_3\text{-}Si\text{-}O\text{-}Si\text{-}(OC_2H_5)_3]+ H_2O$ (20)

This type of reaction can occur continuously, combining hundreds of $HO\text{-}Si\text{-}(OC_2H_5)_3$ monomers into a polymer with huge molecules. Furthermore, silicon alkoxide can form different types of polymers by polymerization process due to its tetrafunctional structure. The polymerization by sol-gel method can occur under both acidic and basic conditions.

Sol-gel method has been usually used in the fabrication of titanium dioxide by using titanium n-butoxide as precursor. The hydrolysis of titanium n-butoxide is similar with that of silicon alkoxide. Owing to the rapid hydrolysis of titanium n-butoxide, hydrolysis inhibitor such as acetic acid is usually used in the sol-gle synthesis. The acetic acid can react with titanium n-butoxide to form $(CH_3COO)nTi(OC_4H_9)_4\text{-}n$. The reaction can be understood by equation as follows:

$Ti(OC_4H_9)_4+ n(CH_3COOH) \rightarrow (CH_3COO)nTi(OC_4H_9)_4\text{-}n+ nC_4H_9OH.$ (21)

The formed $(CH_3COO)nTi(OC_4H_9)_{4\text{-}n}$ will further react with water for hydrolysis and condensation, thus slow down the direct hydrolysis of titanium n-butoxide. Typically, titanium n-butoxide is mixed with acetic acid and absolute ethanol to prepare a precursor. After stirring for 30 min, an uniform bright yellow transparent liquid is obtained. The liquid is moved into a 40 ºC water bath. Then a mixture of deionized water and absolute ethanol is added into the liquid precursor drop by drop

with a certain rate. The liquid phase precursor will change to a gel-like mixture. The mixture transforms to bright yellow solid crystal after aging and dring process. Then grinding and sintering of the solid crystal are performed. Finally, white titanium dioxide powders are obtained. By controlling sintering temperature, titanium dioxide with different crystal phases (rutile or anatase) can be designed and obtained. In our study, we adjusted either pH value or concentration of metal ions in a wide range, expecting to obtain silver salts via sol-gel method, which has not been reported in literatures. Anyway, the formation of silver salts particles in solution is too fast due to the active silver ions. The drastic reaction leads to rapid destruction of integrated network of gel precursor, forming crystal particles with large dimension without the gel process.

In summary, compared with thermal method, one of the most important advantages of sol-gel method is that densification of material can be achieved at a quite low temperature. The densification property of prepared material can be attributed to the slow mild reaction condition of sol-gel process. Otherwise, the low expense and fine control of chemical composition endow the sol-gel method with large numbers of applications in industry and manufacture. It can be used in ceramics processing, optics, biosensors and reactive materials. It is also an effective separation technology for the phase separation of mixture consists of compounds in different states.

2.3.3 Solid-state reaction

Solid-state reaction is also called dry media reaction or solventless reaction, which involves two solid metal oxide powders for heating treatment. Solid-state reaction is a typical homogeneous reaction which involves the same phase of reagent and product. If the reagent and product are in different phase, the reaction is defined as heterogeneous reaction. Owing to the thermal motion of interior material, molecules and atoms may instantaneously deviate from their normal equilibrium position, leading to a diffusion especially at the surface. For example, when two pieces of polishing copper and zinc plates cling together at 493 K for 12 h, a 0.3 mm diffusion layer will form at the interface of the two materials. Based on this theory, the reaction between two stable substances becomes possible. By heating Al_2O_3 and MgO mixture to 1773 K, $MgAl_2O_4$ nucleus will form at the interface of the two materials. As the time increases, more Mg^{2+} and Al^{3+} ions diffuse to the interface and generate more $MgAl_2O_4$ nucleus and promote the growth of $MgAl_2O_4$ crystal. Finally, a thick layer of $MgAl_2O_4$ crystal forms at the contact surface of MgO and Al_2O_3. Another type of solid state reaction occur betwen two active metal salts. The powders are evenly blended and calcined at 400~1000 ºC for various periods of time. One or both of the two salts will be oxidized or reduced under high temperature, further reacting with each other and producing new compound. The reaction could be understood by the formulas below:

$$XCO_3 \rightarrow XO + CO_2 \quad (22)$$

$$XO + YO_2 \rightarrow XYO_3 \quad (23)$$

The property of material prepared via solid-state reaction is highly dependant on the reaction conditions and the property of solid reactants. And for the selection of solid reactants, the reactivity, thermodynamic free energy, surface area and structural property are all important factors which can affect the property of final product. Normally, reactants need to be grinded into fine grained powders before reaction, thus increasing the surface area to enhance reaction rate. The fine grained powders are further mixed by using agate mortar and pestle. Then acetone or alcohol is added into the mixture to obtain a thoroughly mixed paste. The acetone or alcohol can be easily removed by evaporation. The mixture solids are then transferred into crucibles or boats made from noble metal. The container is moved into furnace to be heated at various temperatures and times, which depends on the reactivity of reactants. In recent years, solid state reaction at room or low temperature has attracted much interest in material synthesis. Ling et al. [67] reported the synthesis of $CuCl_2$ $(C_7H_9N)_2$ at a low temperature of 20 ºC via solid state reaction. Light blue $CuCl_2$ and white C_7H_9N were grinded and sifted separately. Then the powders were mixed with a molar ratio of 1:2 and put into a test tube. By shaking the tube for just several seconds, brown $CuCl_2$ $(C_7H_9N)_2$ precipitant was formed.

Although the solid-state reactions are easy to carried out, there are also some disadvantages and concerns. As it is know, solids are much more stable than liquids and gases due the limited diffusion of ions. Anyway, the solid-state reaction occurs on the contact interface of two solid reactants. The two solids can not react and exchange ions with each other at room temperature. Hence heating programme is necessary to

activate the ions of solid reactants. When the temperature is as high as the melting point of the reactants, the diffusion of ions at the contact interface would be easy to carry out. At this stage, the nucleation of new substance starts and the crystal nuclear grows as the time increase. However, due to the slow nucleation and growth rate, single crystal is hard to be obtained. Instead, it is more like to obtain products with polycrystalline property. Because the generation of single crystal normally requires rapid growth of nucleus. Therefore, solid-state method is not suitable for preparation of material if a single crystal is expected. Furthermore, sometimes the reaction is accompanied by gas emitting and sometimes the gas is hazardous such as SO_2. And the air pressure in furnace gets higher and higher as the reaction time increasing, implying safety concerns.

2.4 Applications of photocatalysts

Photocatalyst semiconductors possess a number of special properties that endow them with applications in a wide range of fields. In this section, three of the main functions of photocatalysts for the building construction and environmental remediation are introduced, which are water purification, self-cleaning and anti-bacterial. The work mechanisms of these functions are explained in detail, and some practical applications of the photocatalysts are stated.

2.4.1 Water purification

It has been reported [20, 68, 69] that approximately as high as 20 % of textile

dyes and other dyestuffs of the total world dye production are released into the environment every year. Most of them are contained in the wastewater discharge after dyeing process. These organic dyes and their byproducts would significantly empoison rivers, lakes and oceans, resulting in damages of ecosystem and drinking water source. The halohydrocarbon and benzene series in dyes could be responsible for cancers [70]. Physical adsorption, biological treatment and membrane separation have been applied in wastewater purification to reduce the loss and damage. However, the traditional methods have the disadvantages of high expense, low efficiency and environmental infriendly. Therefore it is still a challenge to find an effective and low-cost strategy to remove these hazardous compounds in wastewaters.

It was found that photocatalytic oxidation (PCO) process could effectively degrade organic pollutants into harmless substances [22, 52, 63, 71, 72]. In these years, the most widely used photocatalyst in wastewater treatment is TiO_2 due to its high activity, high stability, low price and non-toxicity. The mode of TiO_2 application greatly influences the efficiency of wastewater purification system. Normally, artificial light source is necessary to activate TiO_2 settled in reactors since TiO_2 can only absorbs light of wavelength less than 384 nm. In most reactors, UV-A (320-380 nm) radiation is provided by fluorescent low-pressure mercury lamps [73]. It was reported [74, 75] that the using efficiency of UV-C (200-280 nm) is higher than that of UV-A due to the shorter wavelength. Nevertheless, UV-C with short wavelength is usually cut off by the reactor material. Hence lamps emitting UV-C radiation have not been widely spread. There are many kinds of photo-reactors for wastewater

purification system, such as immersion well photo-reactor, annular photo-reactor, multi-lamp photo-reactor, film type photo-reactor and fluidized bed photo-reactor[73]. Several kinds of photo-reactors and their advantages are listed in **Table 2.1**.

Table 2.1 Different photo-reactors for water cleaning and their advantages

Reactor type	advantages
Immersion well photo-reactor	Simple to carry out, can be used in lab scale
Film type photo-reactor	High reaction surface area
Fluidized bed photo-reactor	good utilization of light

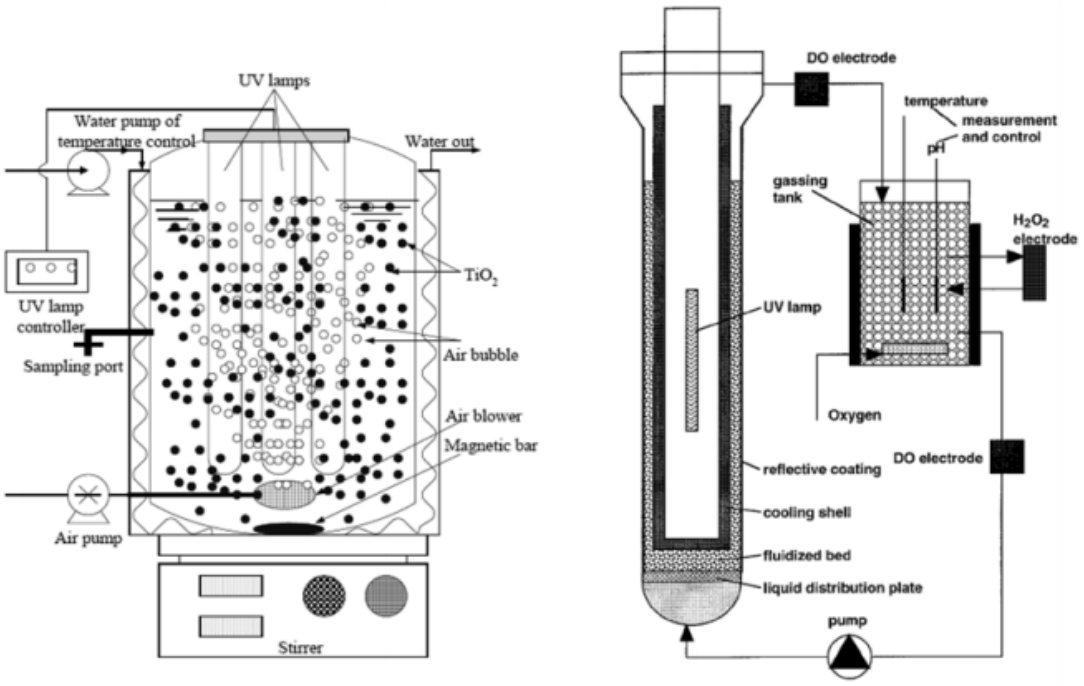

Fig 2.2 Photo-reactors: immersion well photo-reactor (left); fluidized bed photo-reactor (right) [76, 77]

Dye sensitization is an effective process which enables wide band gap semiconductors absorbing visible light and promotes the excitation process. The process mechanism of surface sensitization has been introduced in section 2.2.2. It is

acknowledged that some dye molecules can be excited by visible light irradiation into excited state. When the dye molecules are highly dispersed on the surface of photocatalyst, the excited state can inject an electron to the surface of semiconductor. This charge injection can activate the band (commonly conduction band) of semiconductor to generate oxidative species to carry out the oxidation process. By this way, the dye molecules on photocatalyst surface can be degraded by injecting electrons into photocatalyst, namely, self-degradation of dyes. Thus, wide band gap photocatalyst such as TiO_2 can oxidize organic dyes under natural sunlight.

It is obviously that highly efficient charge injection by excited state of dyes can enhance the degradation efficiency of photocatalyst. Moreover, surface sensitization can extend the responding range of photocatalyst, which is important to the applications of photocatalyst using solar light. However, the charge injection efficiency is affected by many factors including catalyst surface area, crystallinity and the properties of dyes and catalyst nanoparticles. Importantly, a back electron-transfer from photocatalyst to dye^+ would take place due to the recombination of electron and dye^+, reducing the charge injection efficiency as well as the oxidation process. It is reported by Nishikiori et al. [78] that increasing of crystallinity of TiO_2 nanoparticles would improve the surface quality of nanoparticles, thus increasing the electron injection efficiency. Nevertheless, as the crystallinity of TiO_2 increases, the back electron transfer is also enhanced and led to the decrease of quantum yield of photon-current conversion. This is because the surface of amorphous TiO_2 serves like trapping state for electrons due to the alkoxide groups in amorphous TiO_2. The

trapping state surface can slow down the recombination rate of electrons and oxidized dye molecules. As the crystallinity of TiO_2 increases, most of the trapping states are eliminated and led to faster back electron transfer rate, thus reducing the charge injection efficiency. The categories of dyes are also important in dye-assistant photocatalytic degradation process. Rhodamine B (RhB) is one of the mostly used dye in industrial dyeing process. The molecular formula of RhB is $C_{28}H_{31}ClN_2O_3$. Fu et al. [79] have used Bi_2WO_6 to investigate the intermediate products of RhB. The results indicate that RhB can be adsorbed on catalyst surface by carboxyl. Under light irradiation, the decolorization is mainly due to the destruction of staining group, which normally accompanied with de-ethylation. The intermediate products of RhB degradation include oxalic acid, benzoic acid and alizaric acid. Then the intermediate products are further oxidized into carbon dioxide and water by catalyst. Normally, the destruction of staining group is prior to the de-ethylation process. Anyway, the de-ethylation process can happen prior to the decolorization when the concentration of oxidative species at low level. The degradation process of methyl orange (MO) is similar with that of RhB. Firstly, the staining group of -N=N- destroyed by oxidative species. Then the intermediate products of phenol and aldehyde are further mineralized into carbon dioxide and water. Both of RhB and MO can absorb visible light, resulting in photosensitized oxidation by photocatalyst. The degradation of 2, 4-dichlorophenol by TiO_2 with different dye under visible light was studied by Li et al. [80]. The results indicate the dye sensitized TiO_2 pocesses excellent activity under visible light irradiation. After all, photocatalysts with wide band gap are able to be

activated by visible light to operate oxidation process when sensitized by dyes. The oxidation efficiency is significantly depended on the crystallinity and property of photocatalyst and the nature of dyes.

Although photo-reactors based TiO_2 have been applied in wastewater treatment, the reactors can not work without artificial light source which consumes large numbers of electrical power. Thus, novel photocatalyst with visible light responding and which can be easily separated from the reactor and recovered is needed.

2.4.2 Self-cleaning

Commonly, conventional building materials are sustained to outdoor environment and exposed to different weather. As a result, their appearances and properties may change as time goes. To avoid color changes of building materials, protection measures including paintings, chemical cleaners and sealers are widely used in buildings and constructions [82]. Nevertheless, these efforts have not completely solved the problem due to complexities and variability of external factors. Hence it is an urgent to develop an effective and sustained method to protect building constructions from inaesthetic caused by color change. By applying titanium dioxide photocatalyst into construction materials enable the degradation of a large numbers of organic compounds like VOCs (volatile organic compounds) and some inorganic

compounds like NO_x and SO_2. In early 1990s, the first application of self-cleaning concrete blocks made of white cement and TiO_2 occurred at the church "Dives in Misericordia" in Rome [83]. The report in 1996 [84] indicated that there is no obvious difference on the exterior and interior wall during the six years, demonstrating

Fig 2.3 Dives in Misericordia, Rome [81]

photocatalyst with the excellent property of self-cleaning.

In 1995, TiO_2 films containing SiO_2 were demonstrated have a hydrophilic behavior when they were exposed to UV light [85]. The contact angle between catalyst surface and water droplets would be reduced by photocatalysis, which causing super-hydrophobic or super-hydrophilic surfaces of TiO_2. Hydrophobic surface is like the leaves of lotus plant which allow the water droplet moving on the surface. Owing to the specific surface structure of lotus leaves, the bonding between

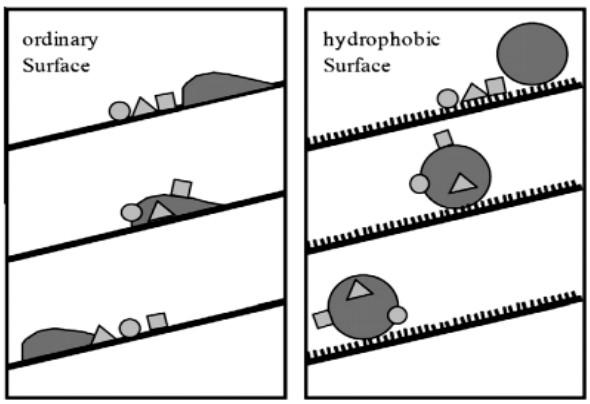

Fig 2.4 Water droplet on ordinary and hydrophobic surfaces [82]

water molecules is maximized as well as the contact angle between water and leave surface. Thus the droplet can maintain spheric shape and roll freely on the surface of lotus leaves. By this way, the dust could be washed away easily by the spheric droplets which have high mobility.

The self-cleaning effect of TiO_2-based materials not only gives expression to the construction materials, but also the exterior building materials such as tiles and glass. These products are mainly for walls and home environment. Through a heat treatment of 600-800℃, TiO_2 powders can be strongly attached to the tile surface to form a thick layer [86]. The self-cleaning effect of the products was evaluated by exposure in outdoor environment for 6 months [87]. The result confirmed that TiO_2-based tiles have an ability to maintain the luster of the surface in long time.

In conclusion, photocatalyst-based building materials exhibit excellent performance for self-cleaning, which attribute to the properties of air pollutants decomposition and hydrophobic surface caused by photocatalysis. These advantages provide the photocatalytic materials good prospects in the near future.

2.4.3 Anti-bacterial

The strong oxidizing power of photocatalyst not only contributes to organic contaminants degradation, but also the self-disinfecting application. So far, TiO_2-based materials have been widely used in indoor furniture and food containers. By contacting the surface of TiO_2-contained product, a number of normal bacteria such as fungi and acarid can be effectively killed under UV irradiation due to the

surface photocatalysis [88, 89]. However, anti-bacterial function of TiO_2 involves complicated process of chemical and biologic reaction. It's still a debatable issue in the previous researches. Some researchers attribute the death of bacterials to the attack of chemical species, while others suggest that biological structure destruction account for the inactivation of microorganism. Also, some scientists found that photocatalytic reaction could cause a significant disorder in cell permeability, which induce a loss of the cell's integrity. Because when microorganisms undergo TiO_2 photocatalytic reaction, the cell wall will be damaged, leading to a direct attack to the nucleus. By this way, some essential functions such as respiratory activity are lost, immediately causing the death of microorganisms.

Saito et al [90] put the TiO_2 powder with an average size 21 nm (30% rutile and 70% anatase) into a bacterial colony. The results show that 60–120 minutes were sufficient to destroy all the bacteria. And it has been demonstrated that using TiO_2 particles with bigger size will reduce the bactericidal capacity. According to the author, the travel distance of photo-induced electron-hole pair of large size semiconductor is longer than that of the one with small size. The longer the travel distance, the harder the carriers migrate to the semiconductor surface, leading to easier recombination of electron-hole pair. Furthermore, Huang et al [91] have confirmed that when the destruction takes place, turning off the UV light doesn't reduce the bactericidal effect. A comparison between TiO_2 containing paint and traditional paint has been carried out. The result in **Fig 2.5** showed photocatalyst paint had maintained initial color for 12 years, while usual antialge paint was polluted after only 3 years. Experts state

hydroxyl radicals generated during the photo reaction possess a destruction capacity of Escherichia Coli bacteria which is 1000-10000 times more effective than traditional chemical disinfection products.

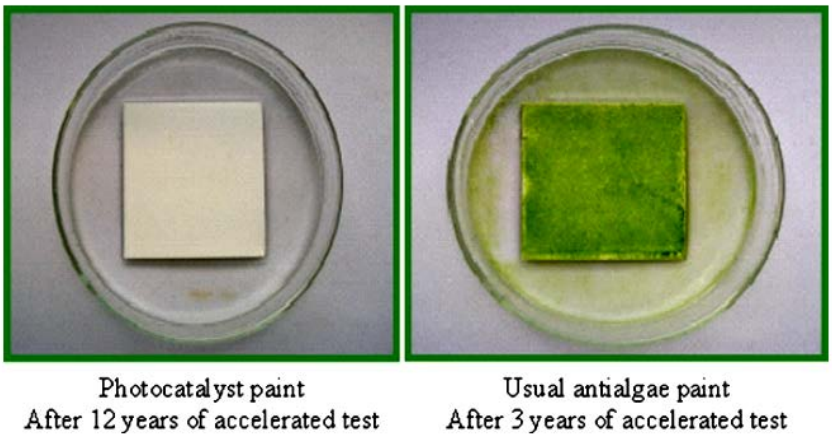

Fig 2.5 Comparison in antialage of photocatalyst properties [84]

To ensure human health and environmental health, measures of disinfection have become more and more necessary. The anti-bacterial function of TiO_2 is exactly useful especially in some microbiologically sensitive fields, e.g. pharmacy and food products. Recent years, the disinfecting effect of TiO_2 has been reported much better than the use of disinfectants in the long run [92]. Moreover, it is reported adding noble metal (such as Pt and Ir) into TiO_2 paint can realize more than 90% reduction in the growth of algae [90].

2.5 Summary of Chapter 2

The concept of semiconductor photocatalysts has been established by introducing the historical background and the two main principles of reaction mechanism. Three of the mostly used synthesis methods of photocatalyst preparation are stated, respectively. Moreover, working mechanisms of the functions of water purification, self-cleaning and anti-bacterial are explained and the existing applications of photocatalysts are introduced.

Chapter 3 Silver phosphate photocatalysts

These years, great efforts have been made by researchers to explore novel semiconductor materials with high photocatalytic activity for pollutants degradations under visible light irradiation. Ag salts-based semiconductors have received considerable attention due to their high activity, suitable band gap energy and intrinsic electronic structure. Among these materials, silver phosphate (Ag_3PO_4) has been an effective visible light responsive photocatalyst. It has significantly high efficiency for organics degradations under light irradiation below 520 nm, as well as for O_2 evolution from water splitting. However, previous works by other researchers reveal that an uncontrolled photocorrosion occurs on Ag_3PO_4 when exposure under irradiation for long time. The serious photocorrosion of Ag_3PO_4 hinders its practical applications and further development. In this chapter, the structure, properties and research status of Ag_3PO_4 have been established. The main strategies to improve the performance and overcome the photocorrosion of Ag_3PO_4 are illustrated by some typical instances.

3.1 Structure and properties of silver phosphate

As a photocatalyst with super-high activity for pollutants degradation, silver phosphate was firstly reported in 2010 [9]. Then this silver salt-based semiconductor attracted much attention by researchers due to its excellent optical and physicochemical properties, such as visible light response, high quantum yield and high energy crystal facets for organic dye degradation. **Fig 3.1** shows the XRD pattern (JCPDS no. 06-0505) and crystal structure of Ag_3PO_4. The structure of Ag_3PO_4 unit cell is a cubic composed of PO_4 tetrahedron and Ag atoms. In the cubic lattice, each Ag atom surrounded by 4 O atoms, P atom surrounded by 4 O atoms and O atom surrounded by 3 Ag atoms and 1 P atom, as shown in **Fig 3.1** Inset. The length of each unit cell is known to be 6.004 Å [4].

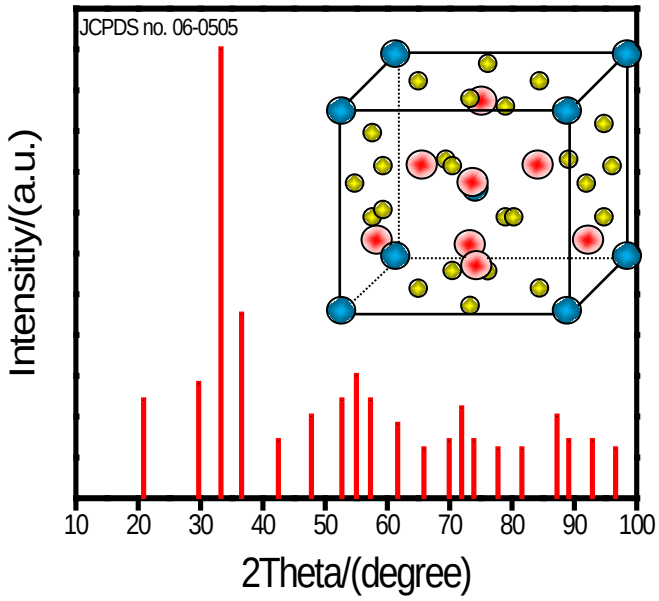

Fig 3.1 XRD patterns for standard Ag_3PO_4. Inset: simulated unit cell of Ag_3PO_4 (blue for P, yellow for Ag, red for O).

Generally, a photocatalytic process includes three stages: in stage 1,

electron-hole pair generates by irradiation, then the excited electrons transfer from the valence band to the conduction band, leading to the separation of the electron-hole pair; in stage 2, the excited holes and electrons transfer to the surface of the semiconductor; in stage 3, the holes and electrons react with water or organics. The first stage is affected by the band structure of the semiconductor. The second stage is relevant to the electric property of the material. And the last stage is dominated by external conditions. MA et al [93] employed the DFT method with the LDA+U formalism to find a large dispersion of the conduction band of Ag_3PO_4. The results indicate the conduction band of Ag_3PO_4 favors for the separation of charge carriers (electron-hole pair), which significantly influences the photocatalytic efficiency of catalyst. The effective separation of electron-hole pair can be understood by two ways. Firstly, the photo-generated electrons have higher mobility than holes due to the antibonding states in the conduction band of Ag_3PO_4. Secondly, a large number of Ag vacancies were revealed in the Ag_3PO_4 lattice. The existing of Ag vacancies can be the capture trap for photo-generated holes. The fast transfer rate of electrons and the capture of holes can significantly reduce the recombination raito of electron-hole pair, leading to the superior quantum yields of Ag_3PO_4. The band gap energy of Ag_3PO_4 can be calculated by Tauc method via absorption spectrum. It has been demonstrated that the indirect bandgap and the direct bandgap of Ag_3PO_4 are 2.36 eV and 2.43 eV, respectively [9]. It means that Ag_3PO_4 photocatalyst can be activated by light with a wavelength below 530 nm, namely, UV light and visible light shorter than 530 nm. Moreover, the valence band of Ag_3PO_4 is located at +2.9 V, indicating the strong

oxidizing power of the photon-induced hole generated from the valence band of Ag_3PO_4. As it is known, in typical photocatalytic process, hydroxyl radical play an important role in oxidation reactions. The oxidizing potential of hydroxyl radical is known to be +2.8 V. It indicates the hole in the valence band of Ag_3PO_4 has stronger oxidizing power than hydroxyl radical. In another word, the hole generated by Ag_3PO_4 can oxidize organic compounds directly, instead of oxidizing water into hydroxyl radical then degrading organics by the hydroxyl radical. Therefore, the strong oxidizing power of the holes under irradiation endows Ag_3PO_4 with excellent performance in water photooxidation reactions (e.g. O_2 evolution and pollutant degradation).

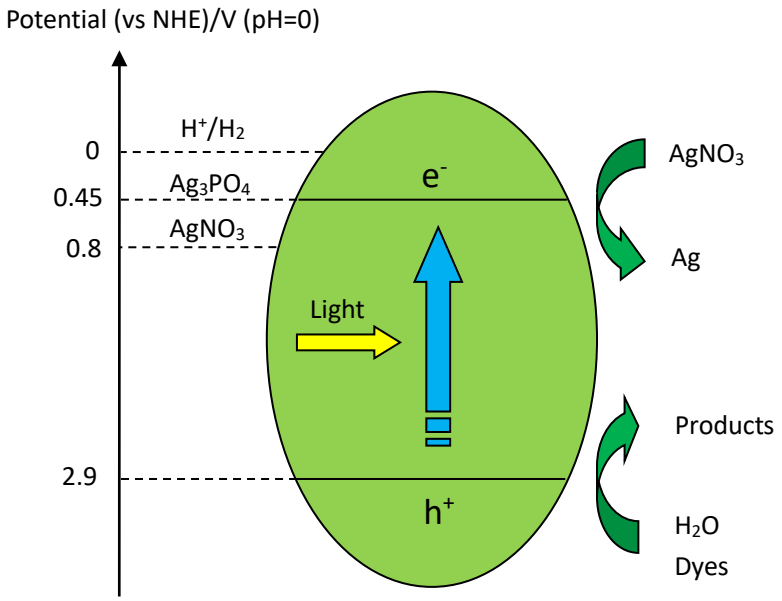

Fig 3.2 Band structure and work mechanism of Ag_3PO_4.

It has been demonstrated by Yi et al [9] that the quantum yields of Ag_3PO_4 can approach as high as 90% at 420 nm irradiation with the present of $AgNO_3$ solution. As shown in **Fig 3.2**, the active Ag^+ in $AgNO_3$ solution can combine with the photon-induced electrons on Ag_3PO_4 surface, thereby decreasing the recombination ratio of electron-hole pairs. Martin et al. [94] also confirm that the quantum yields of Ag_3PO_4 photocatalyst can reach over 90% if charge scavenger or electric bias is used to retard the recombination of electron-hole pairs. In summary, Ag_3PO_4 is an efficient visible light responding photocatalyst for water photooxidation.

However, the stability of Ag_3PO_4 is a concern attributing to that the Ag ions relatively unstable under irradiation, namely, photo-corrosion. The activity of Ag_3PO_4 could be decreased during photocatalytic reaction due to generation of Ag and loss of Ag_3PO_4 substance. Moreover, Ag_3PO_4 is slightly soluble in aqueous solution, the free Ag (I) can be easily reduced into Ag by the photon generated electron [95]. And the main ingredient of silver is a noble metal, implying high cost in the applications. From practical application viewpoint, it is necessary to improve its stability and service life. Although several methods including semiconductor complex [96, 97], morphology control [98] and carbon-based composite [99] have been proposed by researchers to strengthen the stability of Ag_3PO_4, the problem has not been solved yet. Furthermore, the conduction band of Ag_3PO_4 is +0.45 eV, indicating it has no reduction power. Hence it can not be utilized to produce hydrogen by water splitting. It is an urgent to find a suitable application method of Ag_3PO_4 photocatalyst.

3.2 Facet control of silver phosphate

It is acknowledged that the reactivity of a photocatalyst is significantly influenced by its surface properties such as crystal facets, morphologies and nature of electric charge. A catalyst with higher surface energy has higher activity for redox reactions. Because the surface energy is in direct relevant to the adsorption of molecules and the number of reactive sites. Normally, facets with high energy will reduce or disappear during the crystal growth process, while stable low reactive facets maintain at the surface. The reduction of active facets will lead to low surface energy and low activity of catalyst. For example, theoretical studies show that the {001} facets have the highest surface energy for water photooxidation among all the facets of anatase TiO_2. The average surface energy of {001} facets is calculated to be 0.90 J m^{-2}. Anyway, anatase TiO_2 is usually exposured with the stable {101} facets, which is with a surface energy of 0.44 J m^{-2}, which is only a half of that of {001} facets. To maintain the high energy {001} facets of TiO_2, Yang et al. [100] used density functional theory (DFT) calculation to find that the use of fluorine ions can maintain the {001} facets of TiO_2. Then a anatase TiO_2 consists of entire {001} facets had been synthesized, which agrees well with the theoretical studies. And they further confirmed that the sample with {001} facets show much higher photocatalytic activity for pollutants degradation than the sample with {101} facets. After that, this method had been widely used for facet controlling to increase the surface energy of photocatalysts. Commonly, organic surfactants (e.g. SDS) and anions (e.g. F^-) are used to realize high exposure ratio of active crystal facets [101- 104].

There are a number of works on Ag_3PO_4 facet controlling have been done in the past several years. Martin et al. [94] revealed that the {110} facets have the highest surface energy for oxidation among all the facets of Ag_3PO_4 by employing DFT method. This result is according to the standard formula:

$$\gamma = (E_{slab} - NE_{bulk})/2A \qquad (24)$$

Where E is the total energy per unit, N is the number of units, A is the surface area. The surface energies of the {100}, {110} and {111} facets of Ag_3PO_4 are calculated to be 0.67 J m^{-2}, 0.78 J m^{-2} and 1.65 J m^{-2}, respectively. The dangling P-O bonds are responsible for the {111} high energy facets. The redundant P-O bonds need to be sliced to maintain the {111} plane. Hence there will be a short distance between each layer in the [111] direction. This endow the {111} plane with high surface energy. The authors have tested photocatalytic activities of Ag_3PO_4 cubes, dodecahedrons and tetrahedrons, which composed of {100}, {110} and {111} facets, respectively. The results of water oxidation in **Fig 3.3** indicate that the oxygen generation rate of the tetrahedrons is approximately 13 times that of the cubes and dodecahedrons, which mainly ascribes to the difference of crystal facets. This result agrees well with the theoretical calculation of the facet surface energy, in which the {111} facets have much higher surface energy than the {100} and {110} facets. Otherwise, the photo-induced holes in Ag_3PO_4 play a vital role in water oxidation process. The anisotropic mass of holes determine that the smaller of mass, the faster of transfer rate. According to the authors, the anisotropic mass of holes in Ag_3PO_4 reaches the highest in the [110] direction and the lowest in the [111] direction. It means the holes have the

highest mobility in the [111] direction. The fast transfer rate of holes will benefit the efficient charge separation and the migrate process to the catalyst surface. That would be the reason that the activity of dodecahedrons is lower than that of tetrahedrons and cubes in water oxidation. Furthermore, quantum yields of the Ag_3PO_4 tetrahedron approach 98% at 400 nm, due to the high surface energy of the {111} plane and the fast transfer rate of holes along the [111] direction.

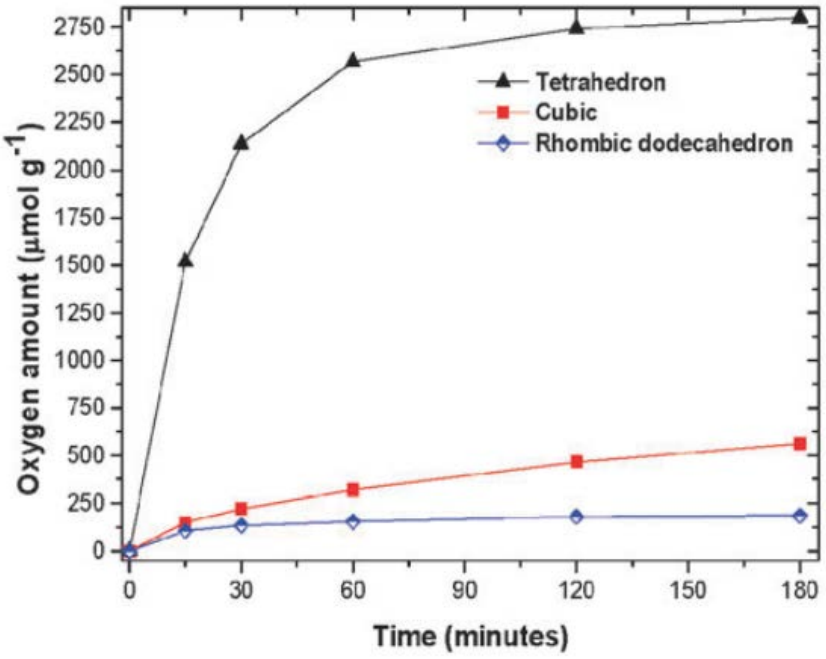

Fig 3.3 Oxygen generation of water by Ag_3PO_4 tetrahedrons, cubes and dodecahedrons under 300W Xe lamp with the electron scavenger of $AgNO_3$ [94].

It is acknowledged that crystals with high index facets have much higher photocatalytic activity than that with low index facets, attributing to high density of atomic steps, danling bonds and kinks [105]. Nevertheless, the growth rate toward the high index facets direction is much slower than that of the vertical directions of these

facts. Hence the high index facets rapidly disappear during the growth process. It is a challenge to maintain high index facets on crystal surfaces. Jiao et al. [106] reported the trisoctahedral Ag_3PO_4 with {221} and {332} facets synthesized via heteroepitaxial growth process starting with Au@Ag nanorods. The exposed {221} and {332} facets of Ag_3PO_4 significantly improved the photocatalytic activity for RhB degradation compared with the low index facets of Ag_3PO_4. However, the preparations of crystals exposed with high index facets demand complicated structure design, precise controlling of crystal growth and high requirement for instruments. It is still a great challenge to obtain crystals with high index facets via a facile method.

Except for the structure of regular polyhedrons, a semiconductor crystal commonly has more than one kind of crystal facets. The different facets have different atomic arrangement, resulting in different electronic structures. Due to the difference of the band energy between two different facets of a crystal, there will be a selective carriers transfer between the two facets. It is reported by Yu and Jaroniec [107] that an electron cascade occurs between the {001} and {101} facets in TiO_2, namely, the "surface heterojunction". The TiO_2 sample has the highest photocatalytic activity when the ratio of the {001} and {101} facets amounts to 55: 45. The results illustrate that the facets exposure ratio of a crystal significantly influences its catalytic activity. It is believed that the "surface heterojunction" can also happen in the different facets of Ag_3PO_4. Up to now, study in relevance has not been reported yet. It is in need to investigate the relationship between the exposure ratio of crystal facets and the photocatalytic performance of Ag_3PO_4.

3.3 Size and morphology

The surface properties (exposed facets, surface area and size) of a semiconductor significantly influence the photocatalytic performance attributing to that the photocatalytic reactions occur at the surface. Compared with the same semiconductor with irregular morphology, the sample with the larger surface area normally exhibits higher efficiency for photocatalytic reaction. This is because large surface area can provide more reactive sites for photocatalytic reactions, leading to high reaction efficiency. It is acknowledged that reduction of particle size can effectively increase the surface area of semiconductors. As the particle size reduced, the specific surface area will greatly increase, as well as the amount of reactive sites. Otherwise, the reduction of particle size will shorten the distance that charge carriers travel to the surface of semiconductor. As the travel distance decrease, the charge carriers can rapidly transfer to the surface of semiconductors and take part in redox reactions. The recombination ratio of electron-hole pairs can be reduced as well, leading to an increase of photocatalytic efficiency. However, Ye et al. [4] reported that the reduction of particle size may also cause some disadvantages on charge transport. According to their work, a strong quantum confinement effect can take place when the particle size equal to the electron mean free path, which is the average distance between two successive collisions of a electron. This effect can increase the recombination ratio of the electron-hole pair, leading to the reduction of photocatalytic efficiency. And the electron mean free path is influenced by the potential gradient and electron

concentration, which is in relevance with the morphology and structure of the semiconductor. Hence, it is in need to synthesize the photocatalyst with large surface area to optimize the photocatalytic efficiency of Ag_3PO_4.

Do et al. [108] reported the synthesis of Ag_3PO_4 nanocyrstals with size ranging from 8 – 16 nm with the assistant of oleylamine. The surface area of the nanocrystals is calculated to be 14.5 $m^2 g^{-1}$, which is much higher than that of the micron-sized Ag_3PO_4 crystals (less than 1 $m^2 g^{-1}$). The activity tests reveal that the photocatalytic activity of the Ag_3PO_4 nanocrystals is higher than that of the Ag_3PO_4 microcrystals due to the large surface-volume ratio of the nano-dimension Ag_3PO_4 crystals. However, the activity of the nanocrystals is only two times that of the microcrystals, considering the huge difference of surface area between the two Ag_3PO_4 crystals. The results indicate that though the reduction of crystal dimension can greatly increase the surface area of semiconductors, it is also accompanied with disadvantages.

The synthesis of specific structures such as plates, belts and rods is an effective way to increase the surface area of photocatalysts. It has also been demonstrated that these structures possess excellent adsorption, electronic and optical properties compared with their bulk materials. The studies of Dong et al. [109] developed a facile method to prepare Ag_3PO_4 semiconductors with different structures including rods, tetrapods, triangular prism and branches. All these structures can be obtained by adjusting the static and ultrasonic conditions. The activity tests reveal that all the samples with specific structures show higher photocatalytic activity than the bulk samples due to the large surface area, good adsorption for dye molecules and efficient

separation of charge carriers. They also indicates that the category of precursor, the growth speed of crystal seeds and the reaction medium can affect the growth habit of Ag_3PO_4 crystals, as well as the morphologies.

3.3.1 Effect of precipitants

Amornpitoksuk et al. [110] reported that the morphologies of Ag_3PO_4 are significantly influenced by the chosen of different precipitants.

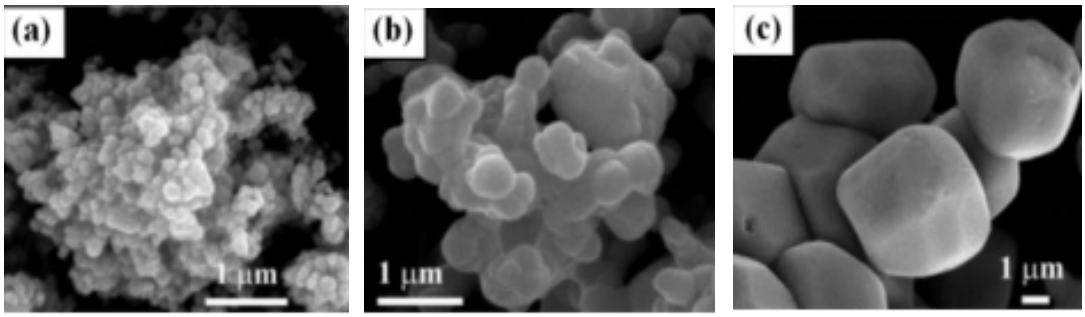

Fig 3.4 Ag_3PO_4 prepared by different precipitating agents: (a) Na_3PO_4, pH=12.10; (b) Na_2HPO_4, pH=9.50; (c) NaH_2PO_4, pH=4.94 [110]

As shown in **Fig 3.4**, Ag_3PO_4 with different morphologies are prepared by using Na_3PO_4, Na_2HPO_4 and NaH_2PO_4 as precipitating agents, respectively. It can be observed that the sizes of the samples are in order of Na_3PO_4＜Na_2HPO_4＜NaH_2PO_4. The results reveal that the concentration of hydrongen ion or the solution pH plays a vital role in the crystal growth of Ag_3PO_4. After that, the work by Dong et al. [111] reported the Ag_3PO_4 tetrahedrons with round corners by using 0.3 M KH_2PO_4 as phosphate source. And two-fold of KH_2PO_4 led to four short branches appear at the four corners of the tetrahedrons. As the amount of KH_2PO_4 increased to three times, Ag_3PO_4 tetrapods with four long branches on the {110} direction are obtained. Their

studies indicate that the morphology of Ag_3PO_4 can be controlled by adjusting the concentration level of precipitating agents. Obviously, the crystal growth rate and final size are affected by the category and concentration level of precipitating agents.

3.3.2 Effect of additives

Organic additives are widely used in the preparation of semiconductors for the complexation with metal ions to form stable precursors. The formation process of Ag_3PO_4 by using organic additives can be sorted by three steps: the formation of silver ion complex, the nucleation and crystal growth and the self-assembly procedure. The utilizations of different additives can form different complexes. The chemical properties, the growth habits and the self-assembly process of these complexes are in great difference, resulting in different morphologies of Ag_3PO_4. The typical morphologies of Ag_3PO_4 crystals obtained by using different organic additives are shown in **Fig 3.5**. The reaction agents are listed in **Table 3.1**.

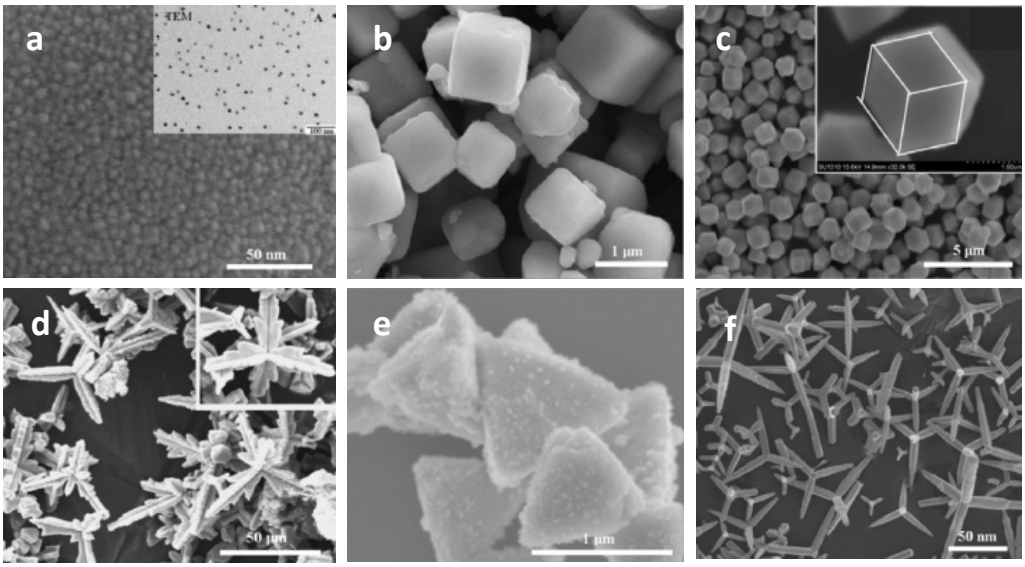

Fig 3.5 SEM images of Ag_3PO_4 morphologies: (a) particles [112]; (b) cubes [113]; (c) dodecahedrons [114]; (d) branches [111]; (e) tetrahedrals [109]; (f) tetrapods [115]

Table 3.1 Raw materials (additives) and sizes of Ag_3PO_4 crystals with different morphologies.

Morphology	**Raw materials**	**Size**
Particle	$AgNO_3$, H_3PO_4, oleylamine [112]	8-16 nm
Cube	$AgNO_3$, NaH_2PO_4, ammonia [113]	1000 nm
Dendrite	$AgNO_3$, H_3PO_4, hexamethylenetetramine [117]	Arm length 20 μm
Tetrapod	$AgNO_3$, H_3PO_4, urea [115]	Arm length 40 μm
Branch	$AgNO_3$, KH_2PO_4, glacial acetic acid [111]	Branch length 40μm
Tetrahedron	$AgNO_3$, H_3PO_4, oleic acid, N,N-dimethylformamide [109]	1000 nm
Dodecahedron	$AgNO_3$, NaH_2PO_4, hexamethyleneteramine [114] $AgNO_3$, Na_2HPO_4▪$12H_2O$, triethanolamine [116]	1000 ~2000 nm

3.3.3 Templates

Bi et al. reported the synthesis of dendritic Ag_3PO_4 crystals by using Ag nanowires as either the Ag source or the templates. Vinyl pyrrolidone (PVP) and H_2O_2 are used in the preparation process as the additive and oxidant, respectively. The PVP is selectively adsorbed on the Ag nanowires surface, while the H_2O_2 oxidize the nanowires to form Ag-O coordination. According to the author, the crystal growth rate could be changed by the adsorbed PVP on the silver surface. The growth speed of the planes covered with PVP is much slower than that without PVP, resulting in a 2-D dendritic structure. However, this 2-D structure will finally disappeared due to the reduction of PVP concentration, which is ascribed to the symmetrical growth rate of Ag_3PO_4 crystal in all facets [118]. Besides, Li et al. [119] prepared the Ag_3PO_4

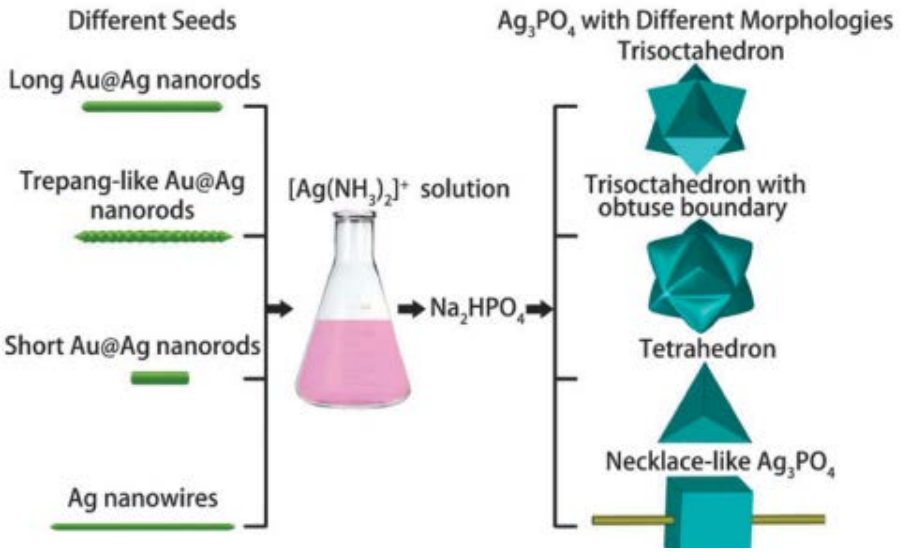

Fig. 3.6 Schematic illustration of the preparations of Ag_3PO_4 polyhedrons using different seeds [106].

nanorods by using polycarbonate as template via a chemical deposition process. The diameters of the obtained nanorods are 2 μm, 275 nm and 85 nm, respectively. The nanorods with the diameter of 275 nm show the highest photocatalytic activity for the degradation of Rhodamine B under visible light, which is mainly due to the proper aspect ratio. Pang et al. [120] reported the preparation of Ag_3PO_4 with the morphologies of particle, trisoctahedron, tetrahedron and tetrapod by adjusting the pH level of the reaction solution. The controllable synthesis method can be ascribed to the one-step synergetic reaction of the raw materials (Ag nanowires, H_3PO_4, H_2O_2). Jiao et al. [106] reported the preparation of a series of Ag_3PO_4 polyhedrons via seed-mediated method by using different seeds. The Ag_3PO_4 trisoctahedron, trisoctahedron with obtuse boundary and tetrahedron are prepared by using the Au@Ag nanorods with different shapes and sizes. An interesting necklace-like Ag_3PO_4 has been synthesized when the template was changed to pure Ag nanowires. The schematic illustration of the preparation process is shown in **Fig 3.6**. The results

indicate that the morphology and structure of Ag_3PO_4 can be tailored by regulating the composition of metal start materials. For example, the reaction of $[Ag(NH_3)_2]^+$ complex and Na_2HPO_4 in the presence of long Au@Ag nanorods results in a Ag_3PO_4 trisoctahedron with sharp corners and edges. When the metal start materials changes into the trepang-like Au@Ag nanorods, a Ag_3PO_4 trisoctahedron with round corners and edges. Notably, Ag_3PO_4 with the high index facets of {221} and {332} are obtained. The {221} and {332} facets of Ag_3PO_4 show superior photocatalytic activity for the degradation of RhB dye under visible light irradiation.

3.3.4 Effect of other factors

Except for the precipitants, additives and templates, there are many other factors can influence the morphologies of Ag_3PO_4 crystals, such as the solvent, pH value and external conditions (e.g. temperature, ultrasonic). Yang et al. [121] reported the flower-like Ag_3PO_4 fabricated by using polyethylene glycol (PEG) as reaction medium. The polyethylene glycol can provide nucleation sites for the flower-like sheets attributing to the interaction between Ag^+ and PEG molecule. Moreover, Indra et al. [122] had used oleic acid and water-in-oil emulsion to fabricate the irregular-faceted Ag_3PO_4 crystals, which exhibits excellent photocatalytic performce for oxygen evolution. Wu et al. [123] also reported the synthesis of Ag_3PO_4 with the medium solvents of dimethyl sulfoxide and ethylene glycol, revealing that the medium solvents play an important role in the growth process of Ag_3PO_4. Dong et al. [124] reported the synthesis of Ag_3PO_4 crystals with different morphologies by N,

N-dimethylformamide (DMF) and water via adjusting the external conditions. Under the static conditions, Ag_3PO_4 branches and tetrapods with smooth edges can be obtained by adjusting the reaction time. In the case of the ultrasonic conditions, the nuclei diffusion is much more intensively than that under normal condition, resulting in the formation of Ag_3PO_4 nanorods and triangular prisms. Lou et al [125] had successfully prepared the concave Ag_3PO_4 crystals via an electrochemical method. The electrochemical oxidation of Ag can release Ag^+ and react with Na_3PO_4 and Na_2SO_4 solution to form Ag_3PO_4 crystals. The releasing rate of Ag^+ can be easily controlled by adjusting the voltage. Overall, the morphologies of Ag_3PO_4 can be influenced by the factors of raw material, precipitant, additive, template, pH value, temperature, reaction time, medium solvent and external experimental condition.

3.4 Modifications of silver phosphate

The recombination of photo-induced carriers has been a problem that significantly influences the photocatalytic efficiencies of semiconductors. The recombination of photo-induced carriers is influenced by the travel distance of carriers, the mobility of carriers, the property of the semiconductor itself and the external environment [126-129]. It has been demonstrated that modification methods can effectively enhance the light absorption, surface catalysis, energy band structure and stability of a semiconductor. To improve the separation and transport of the photo-induced carriers of Ag_3PO_4, some modification methods including metal deposition [130], ion doping [131], composite [132] and carbon-based materials

supporting [133, 134] have been done by researches. In this part, the recent progresses on Ag_3PO_4-based composites are reviewed. The methods of band structure engineering and effective separation of charge carriers with assistant of other materials are mainly introduced.

3.4.1 Metal deposition

It is acknowledged that noble metals such as Au, Ag, Pt and Pd can effectively enhance the light absorption of a semiconductor and the mobility of photo-induced electrons. Since Ag_3PO_4 can easily capture electrons to form Ag, Ag/Ag_3PO_4 composite photocatalysts have been intensively studied in recent years. Bi et al. [135] reported a facile method to obtain the Ag/Ag_3PO_4 composites with controllable ratio of Ag particles by slowly reducing the Ag_3PO_4 in ammonia solution. Glucose is used to react with Ag_3PO_4 as reduction agent. As shown in **Fig. 3.7** the Ag particles emerge on the edges, planes and entire of the Ag_3PO_4 microcubes, respectively. The Ag particles generated on the entire facets of the Ag_3PO_4 microcubes when the concentration of ammonia is 0.1 M. When the concentration of ammonia reduced to 0.05 M, the small particles are mainly formed on the edges of the cubes, only a few particles generated on the surface of the {100} facets. And the Ag particles only appear on the edges of the cubes without adding ammonia. All the Ag/Ag_3PO_4 composites exhibit higher photocatalytic activity than the pure Ag or the Ag_3PO_4 microcubes for the degradation of RhB.

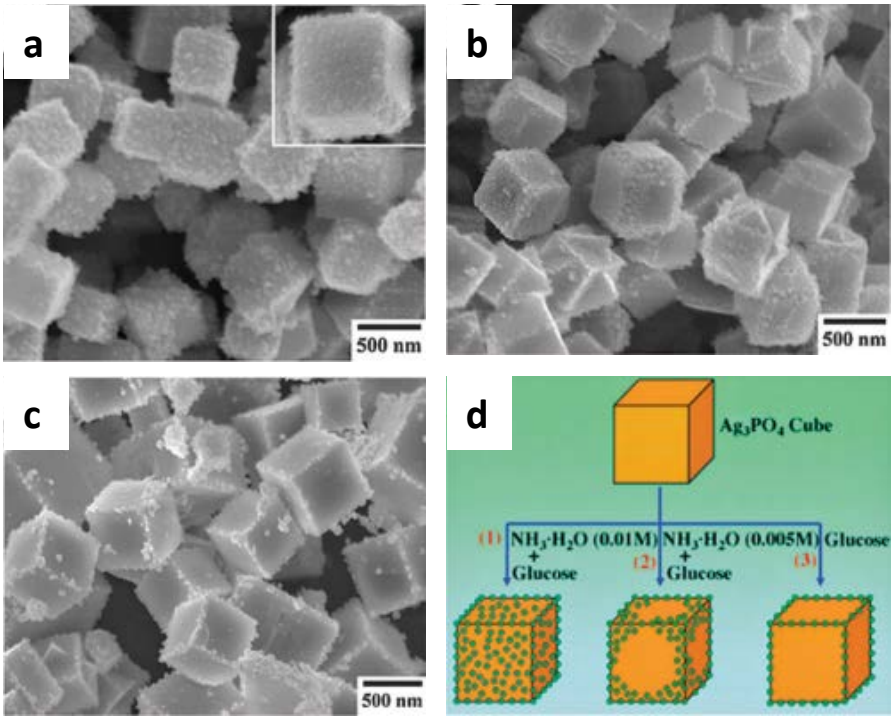

Fig 3.7 SEM images of Ag/Ag_3PO_4 composites prepared with different amounts of ammonia: (a) 0.01 M, (b) 0.005 M, (c) none. (d) Schematic illustration of the preparations of Ag/Ag_3PO_4 with different morphologies. [135]

This is due to the fast separation and high mobility of the photo-generated electrons and holes. Because the good electronic conductivity enables the Ag particles acting as electron captors and transport path. The capture of electrons by Ag can reduce the recombination ratio of electron-hole pair. Meanwhile, the electrons have higher transfer speed on Ag compared with that on Ag_3PO_4 or other medium. These factors result in the good photocatalytic performance of the Ag/Ag_3PO_4. Liu et al. [] prepared the Ag/Ag_3PO_4 composite photocatalytst via a facile hydrothermal method with the assistant of pyridine. The composite shows high stability and photocatalytic activity due to the localized surface plasmon resonance (LSPR). As metallic nanoparticles excited by light, a collective electron charge oscillation will occur when

the frequency of incident photons matches natural frequency of metal surface electrons. The energy of incident photons will be absorbed by the surface electrons of metallic nanoparticles due to the resonance, resulting in enhancement of light absorption. This resonance occurs on metallic nanoparticle surface is known as surface plasmon resonance (SPR). The localization means that the amplitude at the resonance wavelength has been enhanced in a near-field which is highly localized at the material. The LSPR is affected by the dimension of a nanoparticle. Besides, Liu and Wang [136] prepared the Ag/Ag_3PO_4 crystals by illuminating pure Ag_3PO_4 substance. The obtained composite photocatalysts also show higher photocatalytic activity than pure Ag or Ag_3PO_4. Yan et al. [137] successfully deposited Pt, Pd and Au on Ag_3PO_4 using $NaBH_4$ as the reduction agent. The composites exhibit improved light absorption due to the highly dispersed noble metal particles. Importantly, the transfer rate of electrons in the Ag_3PO_4 has been significantly increased due to the noble metal. The high mobility of photo-induced electrons endows the Ag_3PO_4 with high photocatalytic activity and good stability. Besides, Xie et al. [138] reported a precipitating method to deposite lanthanum on Ag_3PO_4 crystals by controlling the kinetic parameters. The results indicate that the deposition of lanthanum effectively enhances the photocatalytic activity of Ag_3PO_4 for O_2 evolution, due to the porous structure, surface defects and large surface area. Recently, Yu et al [139] reported the synthesis of simultaneously modified $Fe(III)/Ag\text{-}Ag_3PO_4$. The simultaneous loading of Fe(III) and metallic Ag have obviously enhanced the visible light absorption and the generation of charge carriers. According to the author, the Ag particles are

responsible for the improved light absorption, while the Fe (III) contributes to the effective separation of photo-induced electron-hole pairs. Because Fe (III) can reduce the oxygen into H_2O_2 and H_2O by capturing the photo-induced electrons, thus decreasing the recombination ratio of the electron-hole pair. Moreover, Fe (III) is inexpensive and rich in natural resource compared with noble metals. The studies of the Fe (III)/Ag-Ag_3PO_4 promote the application of metal-doped Ag_3PO_4 in practical utilization.

3.4.2 Ion doping

Ion doping is an effective method to change semiconductor band structure and properties by introducing atomic impurities. The introduction of a foregion element can significantly change the energy band positions and band gap of the original photocatalyst.

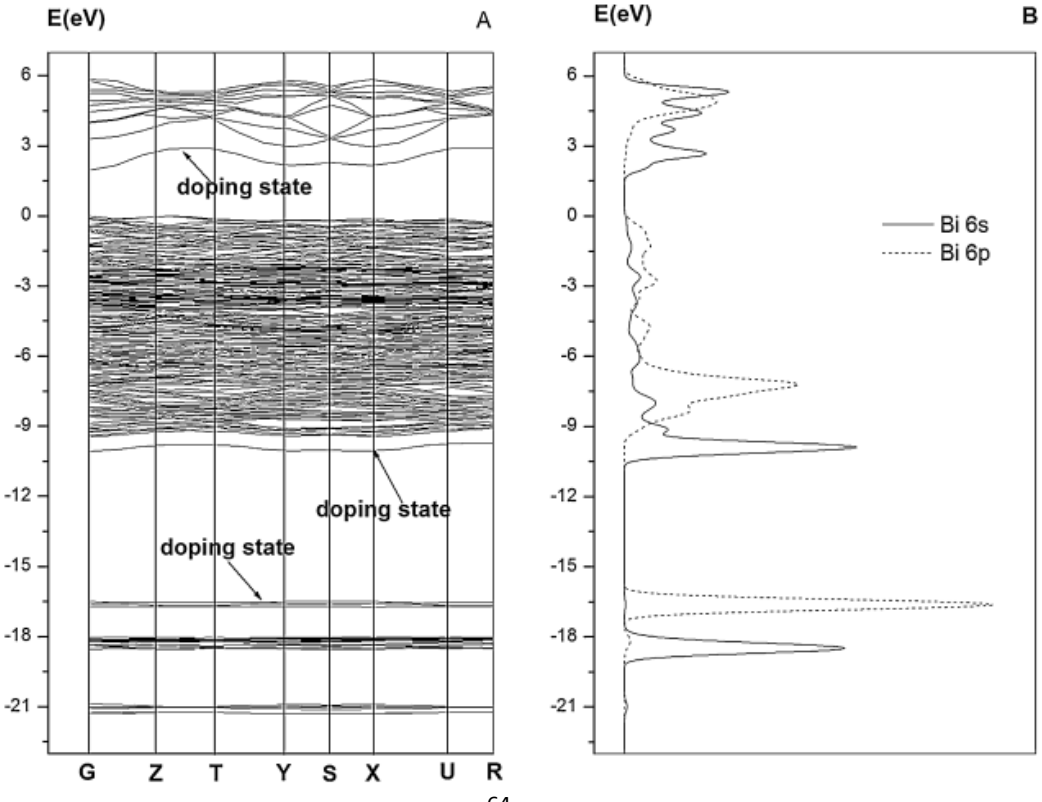

Fig 3.8 Band structure of Bi-Ag_3PO_4 (A) and density of states of Bi atom (B). [131]

Normally, the doping processes come with the formation of defects. Defect energy levels can cause the capture of the photo-induced electron thereby decreasing the recombination probability of electron-hole pairs. The efficient separation of carriers will greatly improve the photocatalytic activity of catalysts. However, the photocatalytic efficiency will be reduced when the concentration of defects is high. Because the abundant defects in the catalyst can be the recombination centers of photo-induced electron-hole pairs. Besides, ion doping can lead to an improved light absorption of a semiconductor due to the change of the band gap. The improved light absorption of semiconductor favors for the photocatalytic reactions. Zhang et al. [131] synthesized the Bi-doped Ag_3PO_4 by an ion exchange method. $Bi(NO_3)_3$ was added into $AgNO_3$ solution under stirring to obtain a precursor with highly dispersed Bi and Ag ions. $(NH_4)_3PO_4$ was used as the precipitating agent in the preparation process. The doped Bi^{3+} enters the unit cell of Ag_3PO_4 and takes place of the P^{5+}, resulting in the shift of the valence band of Ag_3PO_4 to more positive position. The broadening of the band gap has greatly improved the photocatalytic efficiency of the Bi doped Ag_3PO_4. The 2 wt% Bi-Ag_3PO_4 has the highest activity for the photodegradation of methyl orange solution, which is 7.3 times that of pure Ag_3PO_4. The excellent photocatalytic performance of the Bi-Ag_3PO_4 is attributed to both the reduction of OH defects and the change of the electronic structure of Ag_3PO_4. According to the author, ▪OH radicals play the vital role in the photodegradation of methyl orange by Ag_3PO_4. The doped Bi^{3+} effectively decreases the OH defects on the surface of Ag_3PO_4, leading to the fast degradation efficiency of methyl orange. Furthermore, the band

structure and density of states (DOSs) of Bi-Ag_3PO_4 were also investigated through DFT method by the author. As shown in **Fig 3.8**, three doping states derived from Bi 6s and 6p orbitals are observed. These doping states are ascribed to the interaction between O, Ag and doped Bi atoms. The effect of Bi dopants on the electronic structure may be another reason for the improvement of the photocatalytic performance of Bi-Ag_3PO_4. However, only slight difference can be observed from the comparison of band structure and density of states between pure Ag_3PO_4 and Bi-Ag_3PO_4. The influences of doped Bi atoms on Ag_3PO_4 are still not clear and require further studies.

3.4.3 Coupling materials

It has been demonstrated that it is an effective way to improve electron-hole pair separation by coupling two semiconductors with proper band structures. For Ag_3PO_4 semiconductor, the conduction band and valence band are more positive than most of other semiconductors. This means it is easy for Ag_3PO_4 conduction band to obtain electrons from another semiconductor, and holes maintain on Ag_3PO_4 valence band or transfer into the valence band of another semiconductor. The efficient separation of electron-hole pair will significantly improve the photocatalytic activity of Ag_3PO_4. Moreover, the poor stability of Ag_3PO_4 can be enhanced via semiconductors coupling. The formation of new band structure between Ag_3PO_4 and another semiconductor can improve the stability of Ag_3PO_4 through consuming abundant free radicals such as dissolved O_2 by reacting with photo-induced electrons and holes, thus reducing the

probability of the reduction of free Ag^+ by photo electrons. However, it is usually difficult to match two semiconductors with suitable band structure to construct efficient heterojunction systems. As for Ag_3PO_4, there is less choice compared with other semiconductors attributing to that its conduction band and valence band are with such positive potential. In recent years, great efforts have been done in coupling Ag_3PO_4 with other photocatalysts such as TiO_2, Ag salts, $In(OH)_3$ and WO_3.

As the most studied photocatalyst, TiO_2 has suitable band structure with Ag_3PO_4. The negative valence band of TiO_2 can allow injection of holes from Ag_3PO_4 valence band, leading to more efficient photocatalytic reactions on TiO_2 valence band. Yao et al. [97] firstly reported the synthesis of Ag_3PO_4/TiO_2 via a precipitation method. The sample with 47%wt showed the highest photocatalytic activity for the degradation of RhB. The degradation rate of the 47%wt Ag_3PO_4/TiO_2 is tow-fold that of bare Ag_3PO_4 due to the heterostructure between Ag_3PO_4 and TiO_2. As mentioned above, the holes in the Ag_3PO_4 valence band can rapidly transfer to the TiO_2 valence band ascribed to that the valence band of TiO_2 has negative potential than that of Ag_3PO_4. Meanwhile, the photo-induced electrons in TiO_2 migrate to the conduction band of Ag_3PO_4, leading to effective separation of photo-induced carriers. The heterostructure between Ag_3PO_4 and TiO_2 effectively reduce the recombination ratio of electrons and holes, greatly enhancing the photocatalytic activity of Ag_3PO_4/TiO_2. Cai et al. [140] prepared Ag_3PO_4/TiO_2 fibers with good photocatalytic activity and stability. Ag_3PO_4 nanoparticles were uniformly deposited on TiO_2 fiber surface. Hydroxyl radicals were revealed that responsible for the black liquor degradation. Bisides, Rawal et al. [141]

reported that Ag_3PO_4/TiO_2 has good performance in the photocatalytic degradation of gaseous 2-propanol. The degrading efficiency of 2-propanol was evaluated by measuring the amount of CO_2 evolution. The sample with weight ratio 3:97 of Ag_3PO_4/TiO_2 had the highest activity which is 11.67 and 2.93 times higher than that of Ag_3PO_4 and TiO_2, respectively. On the basis of Ag_3PO_4/TiO_2, Teng et al. [142] introduced Ag particles to further enhance the carriers separation, stability and light absorption of the composite. The obtained $Ag/Ag_3PO_4/TiO_2$ exhibited two-fold and 10 times degradation efficiency that of Ag_3PO_4/TiO_2 and TiO_2 for the degradation of 2-chlorophenol (2-CP), respectively. The efficient charge separation and good light absorption due to the LSPR effect was responsible for the excellent photocatalytic efficiency of $Ag/Ag_3PO_4/TiO_2$. Xu et al. [143] reported the synthesis of a multi-heterostructure composite by combining Fe_3O_4 with Ag_3PO_4/TiO_2. The composite showed high activity for acid orange 7 (AO7) under blue laser (50 mW, λ= 405 nm), which is 6 times that of pure Ag_3PO_4. Importantly, $Fe_3O_4/Ag_3PO_4/TiO_2$ can be completely recovered via magnetic separation due to the magnetic property of Fe_3O_4. This approach contributes to the recycling of nano-sized photocatalyst in practical applications on water purification.

The solubility and photocorrosion have been the most serious shortages impeding the practical applications of Ag_3PO_4 under light irradiation. For this reason, Bi et al. [144] prepared AgX /Ag_3PO_4 photocatalyst with core-shell heterostructure by growing silver halide on dodecahedral Ag_3PO_4. Among the AgX/Ag_3PO_4 photocatalysts, $AgBr/Ag_3PO_4$ exhibited the highest photocatalytic activity for MO

Table 3.2 Band structures of semiconductors coupled with Ag_3PO_4

Semiconductor	Conduction band (eV)	Valence band (eV)	Energy band (eV)
TiO_2 [92]	-0.50	2.70	3.20
AgCl [146]	0.22	3.47	3.25
AgBr [147]	0.08	2.54	2.46
AgI [10]	-0.38	2.34	2.72
$BiPO_4$ [63]	0.43	4.28	3.85
BiOCl [149]	-1.10	2.40	3.30
CeO_2 [150]	-0.53	2.67	3.20
ZnO [151]	-0.60	2.60	3.20
$In(OH)_3$ [152]	-0.93	4.24	5.17
$SrTiO_3$ [153]	-0.79	2.45	3.24
Ag_2O [154]	0.20	1.40	1.20
WO_3 [155]	0.64	3.34	2.70
CdS [156]	-0.45	1.80	2.25
Fe_2O_3 [157]	0.20	2.30	2.10
Bi_2MoO_6 [158]	-0.32	2.44	2.76
$BiVO_4$ [159]	0.31	2.78	2.47
Ag_2S [160]	-0.82	1.48	2.30

degradation, which is 14 times that of bare Ag_3PO_4.

The high photocatalytic activity can be attributed to the effective separation of photo-induced electron-hole pair due to the formation of heterostructure. Importantly,

the AgX nanoshell significantly inhibits the dissolution of Ag_3PO_4 in aqueous system, thereby slow down the releasing of Ag^+ by dissolved Ag_3PO_4. And the core-shell heterostructure leads to abandunt electrons at the interface between AgX and Ag_3PO_4, promoting the multiple-electron reduction of O_2. Thus, the photocorrosion of Ag_3PO_4 caused by photo-induced electron could be prevented to some extent. Chen et al. [10] investigated the influence of molar ratio of AgI on the photocatalytic performance of AgI/Ag_3PO_4. The degradation rate of methyl orange and phenol approach the highest when the AgI content reach 20 %. According to the author, tiny amounts of metallic Ag generated at the interface of AgI and Ag_3PO_4 due to the enrichment of electrons on Ag_3PO_4 surface. The transmission of charge carriers has been strengthened by the metallic Ag due to its good electronic properties. The fast transmission of photo-induced carriers favors for the separation of electron-hole pair, resulting in improved photocatalyic activity of AgI/Ag_3PO_4. Apart from AgX semiconductors, Ag_2O/Ag_3PO_4 was prepared via a facile method by Wang et al. []. The heterojunction between Ag_2O and Ag_3PO_4 endows the composite with much higher photocatalytic activity compared with bare Ag_2O and Ag_3PO_4. Tang et al. [161] reported the synthesis of Ag_2S/Ag_3PO_4 and Ag@(Ag_2S/Ag_3PO_4) by a facile anion exchange method. The obtained Ag_2S/Ag_3PO_4 photocatalyst also showed high photocatalytic activity compared with pure Ag_2S and Ag_3PO_4 due to the constructed heterojunction.

Bi-based materials have been widely studied as single or hybrid photocatalytsts attributing to its properties of good optical capacity, high stability and proper band structure for pollutants degradation. Li et al. [162] successfully deposited Ag_3PO_4

nanoparticles on the high energy {040} facet of a truncated bipyramid shape $BiVO_4$ crystal. The high optical capacity, exposed high energy facet and enhanced charge separation efficiency endow the $Ag_3PO_4/BiVO_4$ composite with excellent photocatalytic performance and stability. Xu et al. [163] reported the preparation of a flower-like Bi_2MoO_6 with Ag_3PO_4 nanoparticles deposited on it via a solvothermal method. The author mentioned the concept of the space charge region potential, which influences the recombination probability of electron-hole pair and light capacity. The separation efficiency of photo-induced carriers reaches the peak value when the space charge region equal to the light penetration depth [164, 165]. And the space charge region potential is greatly dependant on the weight ratio of Ag_3PO_4. When the weight ratio of Ag_3PO_4 exceeds optimal value, the charge density increases and the space charge region narrow down. This can lead to easier recombination of photo-generated carriers. On the contrary, when the weight ratio of Ag_3PO_4 below optimal value, the function of heterojunction between Ag_3PO_4 and Bi_2MoO_6 is weakened, leading to the reduction of photocatalytic activity. Wu et al [166] used $BiPO_4$ to couple with Ag_3PO_4 by a hydrothermal method. The composite (Bi:Ag= 4:3 molar ratio) showed highest photocatalytic activity for the degradation of methyl blue (MB) and methyl orange (MO) under visible light irradiation. Lin et al [167] also reported the preparation of $Ag_3PO_4/BiPO_4$ photocatalyst with heterostructure. The photocatalytic activity of $Ag_3PO_4/BiPO_4$ is much higher than that of bare Ag_3PO_4 and $BiPO_4$ under visible light, attributing to the formation of p-n junction and the good absorption of visible light due to the quantum dot sensitization of Ag_3PO_4. BiOCl is an efficient photocatalyst

with specific layered structure which favors for light absorption and separation of photo-induced electron-hole pair. Cao et al. [168] have investigated the influence of molar ratio on photocatalytic performance of BiOCl/Ag_3PO_4. The results indicate that the BiOCl/Ag_3PO_4 with molar ratio 2:1 show the highest photocatalytic activity under visible light, while the composite with molar ratio 10:1 has the highest activity under UV light.

Tungsten trioxide (WO_3) is a photocatalyst which can be activated under visible light. The valence band potential and conduction band potential of WO_3 is 3.34 eV and 0.64 eV, respectively. Zhang et al. [169] successfully synthesized a Ag_3PO_4/WO_3 photocatalyst with high photocatalytic activity for the degradation of RhB and MO. The formation of heterostructure in Ag_3PO_4/WO_3 improved the separation of electron-hole pair, resulting in excellent performance of the composite. Importantly, the conduction band of WO_3 is more positive than that of Ag_3PO_4. Thus photogenerated electron in the conduction band of Ag_3PO_4 can migrate into the conduction band of WO_3, impeding the reduction of Ag^+ by photo electron. Since the reduction of Ag_3PO_4 into metallic Ag is inhibited, the stability of Ag_3PO_4 is significantly improved.

Apart from enhancing the separation of photo-induced carriers, coupling can also modify the surface electronic properties of semiconductors. Guo et al. [152] used $In(OH)_3$ to couple with Ag_3PO_4 to obtain a composite with high negative surface charge. The zeta potential of Ag_3PO_4/$In(OH)_3$ (-60.20 mV) is much more negative than that of Ag_3PO_4 (-1.78 mV) and $In(OH)_3$ (+17.40 mV). The author attributed this

to the increased OH^- on the surface of photocatalyst due to the synergetic hydrolyzation of In^{3+} and PO_4^{3-}. The $Ag_3PO_4/In(OH)_3$ catalyst exhibited greatly high degradation efficiency for RhB due to the high negative charge surface and improved carrier separation. The band structures of semiconductors coupled with Ag_3PO_4 are listed in **Table 3.2**.

Other studies of Ag3PO4 coupling materials including Cr-$SrTiO_3$ [153], ZnO [11], CdS [170], CeO_2 [171], SnO_2 [172] and Fe_2O_3 [173] all prove that the photocatalytic activities of Ag_3PO_4 composites are higher than that of bare Ag_3PO_4 or the coupling materials. The improved photocatalytic performance of Ag_3PO_4 composites can be attributed to the efficient separation of photo-induced electron-hole pair, modification of surface property and change of electric structure. Besides, the photocorrosion of Ag_3PO_4 could be inhibited to some extent due to the construction of heterojunction. Because the band energy difference between Ag_3PO_4 and coupling materials leads to an electron enriching on Ag_3PO_4 [4]. The enrichment of electrons can promote the regeneration of Ag_3PO_4 by reacting with oxygen according to the reaction as follows:

$$O_2+2H+2e^- \rightarrow H_2O_2 \quad (25)$$

$$6Ag + 2PO_4^{3-}+3H_2O_2+6H^+ \rightarrow 2Ag_3PO_4+6H_2O \quad (26)$$

Therefore, coupling Ag_3PO_4 with suitable semiconductors not only enhance the photocatalytic activity but also increase the photo stability of Ag_3PO_4.

3.4.4 Carbon materials

Carbon materials have been widely used to enhance photocatalysts attributing to their properties of high surface area, good conductivity and high stability [174, 175]. For example, graphene is an ideal supporting material with two-dimensional structure. It has been demonstrated that the combination of graphene and semiconductors can improve the mobility of carriers and the separation of photo-induced electron-hole pair, resulting in good photocatalytic activity. Researchers have made great efforts to increase the photocatalytic activity and stability of Ag_3PO_4 by applying graphene. The graphene modified Ag_3PO_4 [176], TiO_2/Ag_3PO_4/graphene composite [177], Ag_3PO_4/Ag/AgBr [178] have been synthesized and they all display higher photocatalytic activity and stability than bare Ag_3PO_4 photocatalyst. Theoritecal studies by Xu et al. [179] indicate that there is a charge fluctuation at the interface of Ag_3PO_4 {100} surface and graphene, promoting the electron transfer from Ag_3PO_4 to graphene. By this interaction, the electrons in the conduction band of Ag_3PO_4 can be rapidly removed into graphene then further consumed by other entities, avoiding the reduction of Ag^+ by photo-induced electrons. Futhermore, graphene can be oxidized to obtain the graphene oxide (GO), which has massive hydroxyl and carbonyl. The hydroxyl and carbonyl endow the GO with good solubility thereby easy to be used in liquid synthesis process. Ag_3PO_4/GO composites have been prepared by different processes such as liquid-phase deposition [180], electrostatic interaction [98] and ion-exchange method [181]. All of the obtained composite photocatalysts exhibited advanced photocatalytic activity and stability for the degradation of organic

contaminants. This is ascribed to the effective trapping of photo-induced electrons by GO, which extends the separation process of electron-hole pair. However, the conductivity of GO is weaker than graphene due to the massive defects on GO surface. Hence, Chai et al. [182] reduced GO sheets via an in situ deposition method to fabricate the reduced graphene oxide (RGO). The RGO has the advantages of good solubility and conductivity, which is easy to combine with other materials and favors for the transfer of electrons. Furthermore, Xu et al. [183] combined Ag_3PO_4 with rolled up graphene sheets, namely, the carbon nanotubes (CNTs). The carbon nanotubes have a tubular structure and are with large surface area, good electrical property and chemical stability. The obtained CNTs/Ag_3PO_4 exhibited excellent photocatalytic activity for the degradation of RhB under visible light irradiation. The activity of the composite is greatly affected by the weight ratio of CNTs and Ag_3PO_4. Wang et al. [184] synthesized CNTs/Ag_3PO_4 with high activity for the degradation of methyl orange (MO). The activity of the composite is approximately 5 times higher than bare Ag_3PO_4. After that, Tian et al. [185] reported the preparation of the composite of Ag_3PO_4 and multi-walled carbon nanotubes (MWCNTs). The Ag_3PO_4/MWCNTs showed higher photocatalytic activity for pollutants degradation compared with the CNTs/Ag_3PO_4 due to larger surface area, higher adsorption capacity and better conductivity. Liu et al. [186] further synthesized Ag@Ag_3PO_4/MWCNTs composite with a triple heterostructure. The triple heterostructure endows the composite with excellent photocatalytic activity for pollutants degradation and superior high stability under visible light irradiation.

In recent years, graphitic carbon nitride (g-C_3N_4) has been intensively investigated as a novel photocatalyst for photocatalytic reactions especially hydrogen production. The band gap energy of g-C_3N_4 is 2.7 eV, indicating it can be activated by visible light irradiation. However, as report goes [187], the quantum efficiency of g-C_3N_4 is as low as approximately 1.5%, limiting its utilization as an independent photocatalyst. The low quantum efficiency is ascribed to the poor light absorption of g-C_3N_4. Silver and boron have been introduced to g-C_3N_4 to enhance the absorption of either dye molecules or visible light by changing the surface states. Anyway, the performance of g-C_3N_4 under visible light has not been improved as much as expected. Up to now, most investigations on g-C_3N_4 is about utilizing it as a co-catalyst or improving its photocatalytic activity via doping reactive metals. Kumar et al. [188] reported the preparation of g-C_3N_4/Ag_3PO_4 by an in situ precipitation method. The composite had the highest photocatalytic activity for the degradation of MO dye when the weight ratio of g-C_3N_4 and Ag_3PO_4 is 1:3. The high surface area, functional heterostructure and effective separation of charge carriers are responsible for the high activity of g-C_3N_4/Ag_3PO_4. Besides, the syntheses of g-C_3N_4/Ag_3PO_4 by ion-impregnating method [189], chemisorption method [190] and precipitation method [188] have been reported. Although the photocorrosion of Ag_3PO_4 has been reduced by combining with g-C_3N_4, there is little imporvement on the degradation efficiency toward pollutants under visible light.

3.5 Summary of Chapter 3

The crystal structure and properties of Ag_3PO_4 have been introduced for better understanding of this photocatalyst. The previous studies on crystal facets of Ag_3PO_4 are summarized with the examples of Ag_3PO_4 dodecahedrons ({110} facet), cubes ({100} facet) and tetrahedrons ({111} facet). The synthesis strategy of morphology control of Ag_3PO_4 photocatalyst is stated. The influences of different parameters on preparation process are discussed, including the effect of precipitants, additives, using templates and other factors. Finally, the previous works of modifications on Ag_3PO_4 (metal deposition, ion doping, coupling with other photocatalysts and combination with carbon materials) have been introduced in detail.

Chapter 4 Experimental techniques and analysis methodologies

The experimental techniques of photocatalysts synthesis and characterization techniques used for physical-chemical analysis of sample are illustrated in this chapter. The methods of data collection and processing are also explained. Moreover, original indoor weak light photocatalytic reaction used in our work is presented, and its work theory and principle are explained.

4.1 Precipitation method

Precipitation is a process obtaining solid compounds from a liquid system by adding reactive agents or changing parameters such as temperature or pH value of the solution. Normally, the solution containing a chemical substance is called a precursor, while the additive causing the formation of solid is called the precipitant and the formed solid named the precipitate. With the force of gravity, the precipitate will sink down to the bottom of solution, leading to a solid-liquid stratification. The liquid above the precipitate is known to be the supernate. Sometimes, the supernate can not be obtained attributing to that the solid suspends in the liquid system due to the low density of the solid. The insoluable precipitate can be easily collected by centrifugation, filtration or decanting.

Precipitation is in great relevance with the solubility of substance. When the concentration level of a substance exceeds its maximum solubility in the system,

precipitant will emerge. The solubility of a substance is affected by the temperature, pH value and component of liquid. For most substance, the solubility will increase with increasing temperature. Anyway, the solubility of NaCl is rarely affected by temperature, while the solubility of $Ca(OH)_2$ decrease with increasing temperature. Otherwise, chemical reaction can lead to the formation of precipitates. The reaction form can be the solid-liquid, liquid-liquid or gas-liquid. For example, CaO, Al_2S_3 and H_2O can react to generate gaseous H_2S and precipitate of $Al(OH)_3$. The addition of $Ca(OH)_2$ solution into Na_2CO_3 solution can obtain the white $CaCO_3$ precipitate. And $CaCO_3$ can also be obtained by importing CO_2 into $Ca(OH)_2$ solution. Importantly, precipitation by chemical reaction also follows the solubility equilibrium, which is a dynamic equilibrium between the solid and ionic states of a substance. Each substance has equilibrium constant at the dynamic equilibrium, which is known as thermodynamic equilibrium constant K= {A(aq)}{B(aq)}/{AB(s)}. The value of a pure solid AB(s) is equal to one. Hence the thermodynamic equilibrium constant K can be reduced into solubility product which is known as K_{sp}= [A(aq)][B(aq)]. [A(aq)] is an activity coefficient of A ions. The dissolving capacity of a compound is highly dependant on its solubility product. And the solubility product of a compound is a constant at certain temperature, which is not affected by the concentration. For the precipitate consists of same amount of ions, the solubility is weaker as the solubility product smaller. For example, AgCl is solid powder which is insoluable in water. Anyway, none substance is absolutely insoluable in theory. The water with AgCl suspension follows the dissolution formular: $AgCl(s) \leftrightharpoons Ag^+(aq) + Cl^-(aq)$. The

solubility product of AgCl equal to $[Ag^+(aq)][Cl^-(aq)]$. When NaCl or $AgNO_3$ are added into the AgCl saturated solution, the activity coefficient $[Ag^+(aq)]$ or $[Cl^-(aq)]$ will change. This will change the thermodynamic solubility equilibrium, resulting in the reduction of dissolving capacity of AgCl. Besides, sometimes precipitation can also occur in solid reaction due to ion implantation or quenching. Solid precipitation is widely used in the synthesis of nanoclusters.

In this work, except for that tetrapod-like Ag_3PO_4 was fabricated by hydrothermal method, all the Ag_3PO_4 samples were prepared by precipitation method at room temperature (25 ºC). The precipitated pH value of Ag_3PO_4 is ranged from 4.6-6.1. The solutions used were water, PEG 200 and tetrahydrofuran/water.

4.2 Characterization techniques of photocatalyst

This section states the physical characterization techniques used in this work for the characterizations of phase, morphology, surface property of samples. The fundamentals of X-ray Diffraction (XRD), Scanning Electron Microscope (SEM), Transmission Electron Microscope (TEM), UV-vis diffuse reflectance spectra (DRS), thermogravimetric analysis (TGA) and nitrogen adsorption-desorption are illustrated.

4.2.1 X-ray Diffraction

X-ray Diffraction (XRD) is an analytical technique used for phase identification of crystalline material. It can also be used to measure unit cell dimension and analyze surface properties of material. X-ray diffraction is based on constructive interference

of monochromatic X-rays and crystalline sample. Firstly, cathode ray tube generates X-rays and these X-rays produce monochromatic radiation after filter. The monochromatic radiation is concentrated and illuminate at the sample. Then the interaction of incident ray and sample produces diffracted rays which detected by receiver to process and count. When the diffracted rays satisfy Bragg's Law ($n\lambda=2d \sin\theta$), all diffraction directions of the lattice will be attained due to the orientation of the material itself. Every mineral has a set of unique d-spacings so that the sample could be identified to the conversion of the diffraction peaks to d-spacings. Thus, the kind of mineral can be determined by comparison of d-spacings with standard reference patterns.

X-ray diffraction instruments consist of three basic parts: X-ray tube, sample holder and X-ray detector. Electrons generated by heating a filament and accelerated toward a particular material by applying a voltage. When electrons have enough energy to dislodge inner shell electrons of the material, characteristic X-ray spectra is formed. The specific wavelength of X-ray depends on which the material is (Cu, Fe, Mo or Cr). Foils or crystal monochrometer is required to produce monochromatic X-ray. Then the monochromatic X-ray illuminates the sample on sample holder to produce diffraction rays. The diffraction rays detected by X-ray detector and processed, converting the signal to a count rate output to computer monitor. By rotating the sample holder and the X-ray detector, all possible peaks will present on computer monitor. According to the 2θ degree and intensity of peaks, the phase, purity and structure of materials can be identified. Moreover, XRD pattern is one of the

mostly used methods to confirm the ion doping of semiconductors. The ion doping involves introducing foreign atomic impurities into a semiconductor. The introduction of a foreign element will cause a size increase of the original unit cell, resulting in a shift of diffraction peak to the right of standard position. Hence the shift of diffraction angle is indirect evidence which can be used to demonstrate the occurrence of doping.

In this work, The X-ray diffraction spectra measurements were performed on an instrument using Cu Kα radiation (XRD-6100, Shimadzu). The XRD patterns were recorded from 10° to 80° with a scanning rate of 7 degree/min.

4.2.2 Scanning electron microscope

Scanning Electron microscope (SEM) is an equipment produce images of samples by scanning them with high-energy beam of electrons. The electrons interact with atoms in the sample and reflecting signals contain information of topography and position of samples. Secondary electron imaging is the mostly used detection mode. In this mode, there are two electron beams emitted toward the sample, namely, a primary electron beam with high energy and a secondary electron beam with lower energy. The primary beam interacts with the sample and reflects signal, while the secondary beam emitted from a close position to the sample resulting in reflection too. The reflection signals then detected by detectors and produce image on computer monitor. SEM can produce very high-resolution images less than 1 nm in size of a sample. By rotating specimen plate, images of sample in different directions can be observed. Before imaging in the SEM, all the samples must be electrically conductive

to prevent the accumulation of electrostatic charge at the surface. Normally, the specimens are coated with ultrathin coating of electrically conducting material such as gold by low vacuum sputter coating. Scanning electron microscope consists of an electron gun, an anode, a magnetic lens, a scanning coil, a backscattered electron detector and a secondary electron detector. Schematic illustration of SEM is shown in **Fig 4.1**.

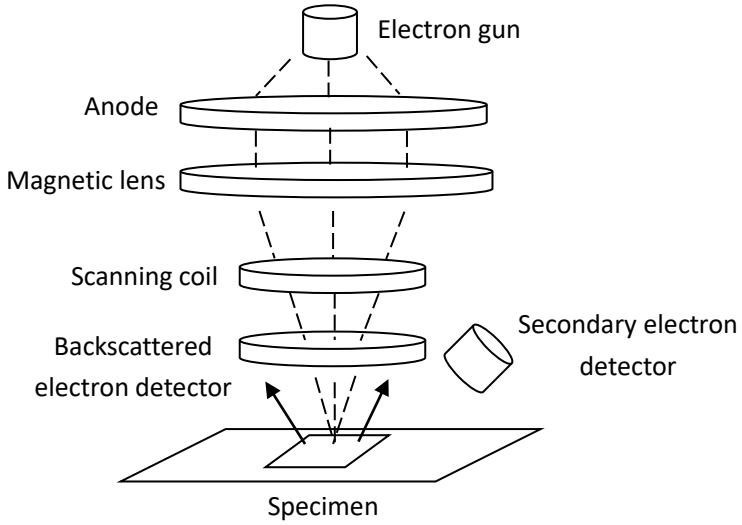

Fig 4.1 Schematic illustration of the SEM work mechanism.

The instruments also include a vacuum system which consists of a vacuum pump and a vacuum column. The vacuum pump is used to produce vacuum environment in the column during the test. There are two main reasons for the utilization of vacuum system: 1) the filament will be easily oxidized and invalidation in atmospheric environment. Hence it is necessary to fill the column with inert gas such as pure nitrogen to protect the filament. 2) The mean free path of electron is larger in vacuum environment compared with that in air, resulting in that more electrons can be used in

electronic imaging.

The morphology and size of the obtained samples in our work were characterized by a scanning electron microscope in type of Hitachi SU1510 with a working voltage of 15.0kV.

4.2.3 Transmission electron microscope

Transmission Electron Microscope (TEM) is a technique using high energy electron beam to transmit through a sample to obtain images. TEM is commonly used to obtain images at high resolution to analyze the crystal orientation, electronic structure and hollow structure of samples. Incident electron beam with higher than 100 k eV is usually used for imaging internal structure of sample. Thus images of sample at a significantly high resolution can be obtained. The TEM consists of an electron gun, a vacuum system, a specimen stage, several electron lenses and apertures. Electrons with high energy can be generated from the electron gun by applying high voltage. The vacuum area can increase the mean free path of the electron gas interaction. The electron lenses are designed to focus parallel rays at some constant focal length. Finally, Apertures can filter electrons which are further than a fixed distance from the optic axis. Schematic illustration of the TEM is shown in **Fig 4.2**.

Although the electrons are with such high energy, it still requires the thickness of specimen to be extremely thin. The thickness of specimen above 500 nm would result

in failure to obtain images. For a specimen with thickness around 100 nanometers, Selective Area Electron Diffraction (SAED) and High-resolution Transmission Electron Microscope (HRTEM) will be available. For the SAED, the image on the TEM will be a series of spots. Each spot corresponding to a satisfied diffraction condition of the crystal structure of sample. It can present image areas of specimen that as small as several hundred nanometers. The SAED enables researcher to identify crystal structures and crystal defects. Otherwise, the HRTEM is an imaging mode that for direct imaging atomic structure of specimen. By measuring the lattice spacings in HRTEM image, the exposed crystal facets and plane can be obtained. And the crystal facets and plane are important factors which affecting the activity of catalysts.

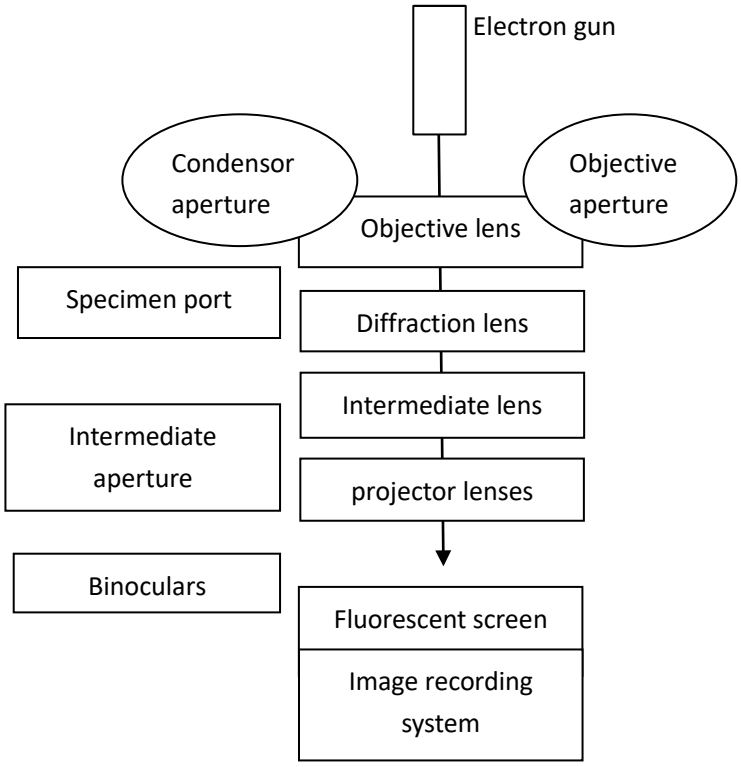

Fig 4.2 Schematic illustration of the TEM work mechanism.

To state, in this work, the TEM images are obtained by type JEOL JEM-2100F,

with the assistance of Wuhan University of Technology, China.

4.2.4 UV-vis spectrum

In analytical chemistry, UV-vis spectrum or UV-vis Diffuse Reflectance Spectra (DRS) is a common technique to determine the category and concentration level of molecules in solution. Substance molecules can absorb light energy in ultraviolet or visible region and every molecule has a unique maximum absorption wavelength in UV-vis spectra due to its molecule structure. When light with wavelength from high to low go through the sample solution, absorption curve can be obtained. And the position of maximum absorption wavelength (peak) can reflect the kind of the molecule in the sample solution, thus determining the category of substance. When testing the concentration level of a solution, a corresponding blank sample is usually used to be compared with the target solution. A calibration curve can be obtained by testing the blank sample. Based on the calibration curve, the intensity of absorption curve could reflect the concentration level of the corresponding molecule in the solution. Moreover, for the test of known substance, the absorbance intensity can be obtained by illuminating the substance with the light wavelength equal to maximum absorption wavelength of the substance. For example, the maximum absorption wavelength of RhB is 554 nm. The intensity basis which equal to zero can be obtained by testing a blank sample (normally pure water) at 554 nm. Then the absorption intensity of RhB solution can be measured directly. The quantitative way to determine concentrations of absorbing species in solution satisfies with the Beer-Lambert Law,

which is:

$$\mathbf{A = \log_{10} (I_0/I) = \varepsilon cL} \quad (27)$$

where A is the measured absorbance, I_0 is the intensity of the incident light at a given wavelength, I is the transmitted intensity, L the path length through the sample, and c the concentration of the absorbing species. For each species and wavelength, ε is a constant known as the molar absorptivity or extinction coefficient.

In this work, UV-vis DRS results of the samples were obtained using a UV-vis spectrophotometer in type UV-2550, Shimadzu.

4.2.5 Nitrogen adsorption-desorption

Nitrogen adsorption-desorption is a physical technique to study the surface properties of solid material. This technique is commonly used to measure specific surface area and pore size, pore volume and pore distribution of porous material. Porous materials can be devided into microporous, mesoporous and macroporous due to the pore sizes. The pore sizes of microporous, mesoporous and macroporous are <2 nm, 2-50 nm and >50 nm, respectively. Before the ad-desorption process, it is necessary to remove the remaining liquid in the sample by heating to ensure the sample is entirely solid. The sample is then put into an elongated quartz tube and vacuumized. Nitrogen is the mostly used gas adsorbate for characterization of the

solid surface. The gaseous nitrogen is provided by heating liquid nitrogen to 77 K (boiling temperature of N_2). It is acknowledged that the gas adsorption capacity of a specific solid is constant at certain pressure. By changing the pressure, an adsorption isotherm can be obtained due to the different gas adsorption capacity of solid. By analyzing the adsorption isotherm the total surface area and specific surface area of solid can be calculated. It involves Brunauer-Emmett-Teller (BET) theory which used to measure specific surface area of materials by analyzing the physical adsorption of gas molecules on a solid surface. The specific surface area means the surface area of per unit of mass of a material. The BET theory agrees the equation as follows:

$$\frac{1}{v[(p_0 / p)-1]} = \frac{c-1}{v_m c}\left(\frac{p}{p_0}\right) + \frac{1}{v_m c} \qquad (28)$$

where p and p_0 are the equilibrium and the saturation pressure of adsorbates at the temperature of adsorption, v is the adsorbed gas quantity, and v_m is the monolayer adsorbed gas quantity, c is the BET constant.

The total surface area and specific surface area can be obtained as follows:

$$S_{total} = \frac{v_m N s}{V} \qquad (29)$$

where v_m is in units of volume which are also the units of the molar volume of

$$S_{BET} = \frac{S_{total}}{a} \tag{30}$$

the adsorbate gas, N is Avogadro's number, s is the adsorption cross section of the adsorbing species, V the molar volume of the adsorbate gas, and a the mass of the solid sample or adsorbent.

For the calculation of SPMs specific surface area by BET method, the correlation coefficient is 0.99064. The value of each data is as follows: p/p_0=0.3137, v=2.4029, c=22.107. v_m is calculated to be 1.8126. N= 6.022140857×10^{23}, V=22.40 L mol^{-1}, s=1.14×10^{-23}, the sample mass is 0.0772 g. The specific surface area of SPMs is calculated to be 7.1982 $m^2\ g^{-1}$. Besides, the specific surface area of solid Ag3PO4 by BET calculation is 1.5262 $m^2\ g^{-1}$, in which p/p_0=0.3146, c=37.236, v=0.5144.

The BET theory is established on the base of five assumptions: 1) only well-defined sites can occur adsorption; 2) a molecule can be an adsorption site for the molecule in its upper layer; 3) the surface is in equilibrium with gas phase; 4) the desorption is a homogeneous kinetically process; 5) every adsorption site is filled with gas at saturation pressure.

In characterizations of photocatalysts, surface area is a very important factor which may indicate the adsorption efficiency for organic molecules and further affects the photocatalytic activity of material. The texture properties of the samples were

measured by nitrogen sorption isotherms in this work. The data of surface area is processed by software of ASiQwinV200.

4.2.6 Thermogravimetric analysis

Thermal gravimetric analysis (TGA) is a process to analyze physical and chemical properties of material by increasing temperature with constant heating rate or changing time with constant temperature or mass loss. Information of physical process such as adsorption, desorption, sublimation and vaporization can be studied via TGA. And TGA can also provide information of some chemical properties by chemisorption, dehydration, decomposition and oxidation. Characterization of materials through decomposition analysis is an important application of TGA. By heating a material to the decomposition temperature, the components of the material can be determined. Moreover, organic and inorganic content in a material can be determined by TGA, which contributes to predicting material structures or quantitative analysis of each component. The TGA procedure requires a precision balance with a pan loaded with the sample and a programmable controlled furnace. The furnace can meet the requirement of constant heating rate and constant mass loss with time. Commonly, the precision balance weighs a sample online as it is heated to up of 2000 ºC. As the temperature increases, various components volatilize from the sample and the mass change can be measured. Moreover, the temperature of volatilization can tell the category of component by referring to material boiling point.

By combining the material boiling point and preparation method, the category of component can be predicted. Furthermore, the percent mass of an individual component in a known sample can be calculated by the stoichiometric ratio of ash content and starting weight. Because each component is liberated at different temperature. By counting the mass loss in every heating stage, the percent mass of the component can be measured precisely. The mass percent of end product in starting material is known as ceramic yield.

Thermal stability evaluation of materials is also an application of TGA. No observed mass change indicates the good thermal stability of the material. For some thermal stable polymers, the mass will not change even when the temperature exceeds their boiling points. Because there is a large temperature range from melting to decomposition of the polymer. As the weight of polymer changes, the decomposition of polymer starts. Otherwise, the oxidative mass loss is the most common weight loss in TGA. Most of organic compounds will be oxidated by oxygen at the temperature range from 200-300 ºC. Hence, starting from 100 to 300 ºC, moisture, organic compounds and some unstable solid will be liberated one after another, resulting in mass loss of the initial material. Moreover, TGA is a common method to evaluate oxidation resistance by heating materials under air condition. Some alloys such as aerospace materials need to be recovered for next use due to their high expense. The oxidation of alloys caused by fuel combustion make the alloys can not be reused. Therefore, the oxidation resistance is an important factor for the materials like alloy.

4.3 Photocatalysts used in this work

All chemicals used were analytic grade reagents without further purification; polyethylene glycol 200（PEG 200）, silver acetate, silver nitrate, 85% phosphoric acid, tetrahydrofuran (THF), urea, hexamethylenetetramine, tetramethylene oxide, sodium hydroxide, P25 powders were purchased from Shanghai Reagents Company (Shanghai, China). The preparation methods of Ag_3PO_4 photocatalysts used in this work are presented as follows.

Synthesis of solid silver phosphate. The irregular Ag_3PO_4 particles were synthesized as previously reported [115]. Typically, appropriate amounts of raw powders of Na_2HPO_4 and $AgNO_3$ were thoroughly ground until the initial white changed to yellow. The precipitation was collected and washed with deionized water for several times. Finally, the product was dried at 60 °C for 8 h.

Synthesis of silver phosphate porous microtubes. Typically, 2 mmol silver acetate was added into 40 mL poly ethylene glycol 200 (PEG 200) at room temperature. Under stirring, 40 μL phosphoric acid (85 wt.%) was then added into the solution above. After stirring for 15 min, the produced precipitate was washed by ethanol and distilled water for 3 times, respectively. Finally, the sample was dried at 60 °C for 4 h.

Synthesis of silver phosphate tetrapods. Typically [115], 3 mmol of 85% H_3PO_4 was dissolved in 80 mL of deionized water and 2.5 mmol of $AgNO_3$ was added under stirring. Then, 37.5 mmol of urea were put into above solution. The resulting precursor was transferred into a Teflon-lined stainless steel autoclave and maintained at 80 °C for 24 h. The yellow precipitation was collected and washed with deionized water several times, then dried overnight at 60 °C.

Synthesis of the Ag_3PO_4 dendrites. In a typical synthesis [117], 32 ml deionized water was placed in a breaker, and 8 ml tetrahydrofuran (THF) was then added. 0.318 g Ag_3NO_3 was added into the mixed solvent above under stirring. Then, 41 µl of 85 Wt.% H_3PO_4 was added drop wise to the solution above. Finally, 0.197g of hexamethylenetetramine (HMT) was introduced into the above solution. The whole process was carried out at room temperature under stirring. The color of the reaction mixture changed from silvery white to golden yellow after injection of the HMT. Then the yellow precipitation was collected, washed with deionized water for several times, and dried at room temperature.

Preparation of silver phosphate dodecahedron. In a typical synthesis [191], CH_3COOAg (0.2 g) was solved in aqueous solution. Na_2HPO_4 aqueous solution (0.15 M) was added with drop by drop to the above solution, and golden yellow precipitation would be formed. The obtained samples were washed with water and dried under atmosphere.

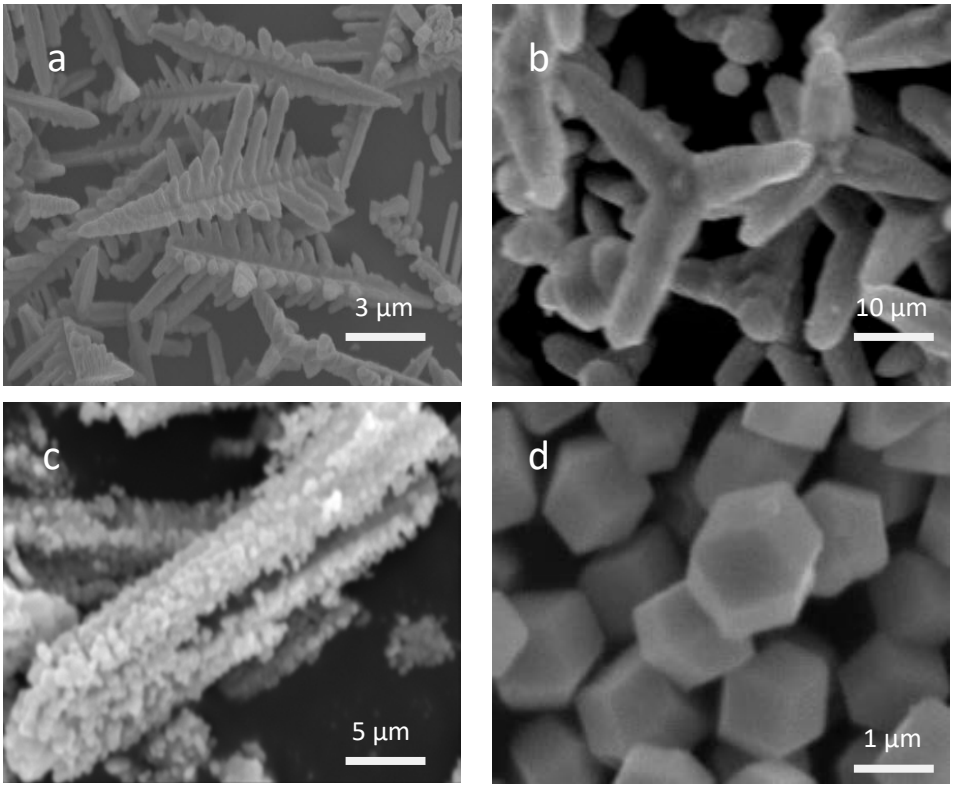

Fig. 4.3 SEM images of the as-prepared Ag_3PO_4 samples: (a) Dendrites; (b) Tetrapods; (c) Microtubes and (d) Dodecahedrons

4.4 Evaluation of photocatalytic activity

The photocatalytic activity of sample can reflect the decomposition efficiency of pollutants by photocatalyst. In this thesis, activities of the samples are tested by using Rhodamine B (RhB), methyl orange (MO) and the RhB-MO mixture dye as the

probing molecules. The parameters of the test and experimental conditions under visible light irradiation are introduced as well as under natural indoor weak light.

4.4.1 Evaluation under visible light

For the evaluation of photocatalytic activity of samples under visible light, a 400 mL column type beaker with a magnet in it was settle down on a magnetic stirring apparatus. A 300 W Xe lamp was placed right above the 400 mL beaker supplying visible light of wavelength above 420 nm by installing a glass filter in front of the light source.

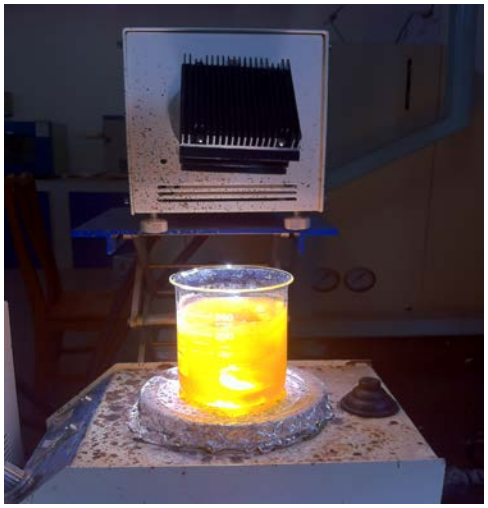

Fig 4.4 Degradation of MO over Ag_3PO_4 by visible light irradiation.

The illustration of reaction device is displayed in **Fig 4.5**. Typically, 0.1 g of photocatalyst was added into the dye solution (200 mL, 10 mg/L RhB or MO). The suspension was stirred for 30 min to reach an adsorption–desorption equilibrium of dye molecules on the surface of photocatalyst. Then the dye solution was irradiated by the Xe lamp from top of the beaker. The distance between the light source and liquid surface was settled to be 15 cm. And the light density at the liquid surface was measure to be 68.2×10^3 cd by an irradiatometer (FZ-A type, Handy, China). During

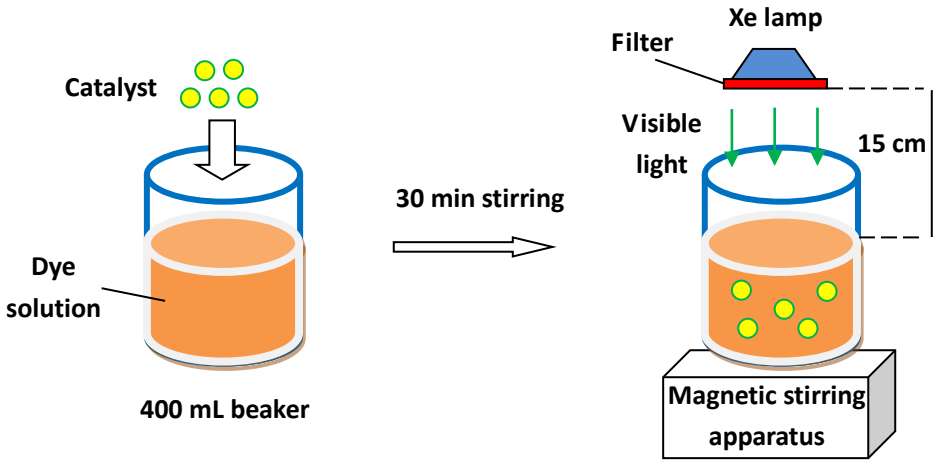

Fig 4.5 Schematic illustration of reaction device for evaluation of photocatalytic activity under visible light.

degradation, 4 mL of suspension was collected at a given interval time and centrifuged by a high speed centrifuge (CTK 80 type, Xiangyi, China) to remove the particles. The particles were put back into the beaker to maintain the initial quantity of photocatalyst. The concentration of dye remained in the solution was determined by using UV–Vis spectrophotometer. For RhB-MO mixture wastewater, 200 mL of 10 mg/L RhB and 10 mg/L MO are employed. The pH values of all the solutions are

tested to be approximately 6.

The degradation efficiency (η, %) is calculated by the formulae as follows.

$$\eta\ (\%) = (C_0\text{-}C)/C_0 \quad (31)$$

where η is the degradation efficiency; C_0 is the initial concentration of dye; and C is the remained concentrations of dye at different irradiation times. The apparent kinetics reaction rate can be calculated by:

$$\ln(C_0/C) = k_a \times t, \text{ or } C = C_0 \times \exp(-k_a \times t) \quad (32)$$

A plot of $\ln(C_0/C)$ versus time (t) represents a straight line, the slope of which upon linear regression equals the apparent first-order rate constant (k_a).

4.4.2 **Evaluation under natural indoor weak light**

The evaluation of photocatalytic activity of Ag_3PO_4 under natural indoor weak light aims to study the performance of Ag_3PO_4 in practical applications for pollutants degradation by entirely utilizing solar energy. The dye solution (200 mL, 10 mg/L RhB or MO) was poured into a volumn beaker placed on a magnetic stirring apparatus.

0.05 g of catalyst was added into the beaker under stirring to reach an adsorption–desorption equilibrium of dye molecules on the surface of photocatalyst. The dye solution containing photocatalyst was settled on a table (1.2 m height) in the center of the laboratory room (Nanjing, in China). The room is 16 square metres in

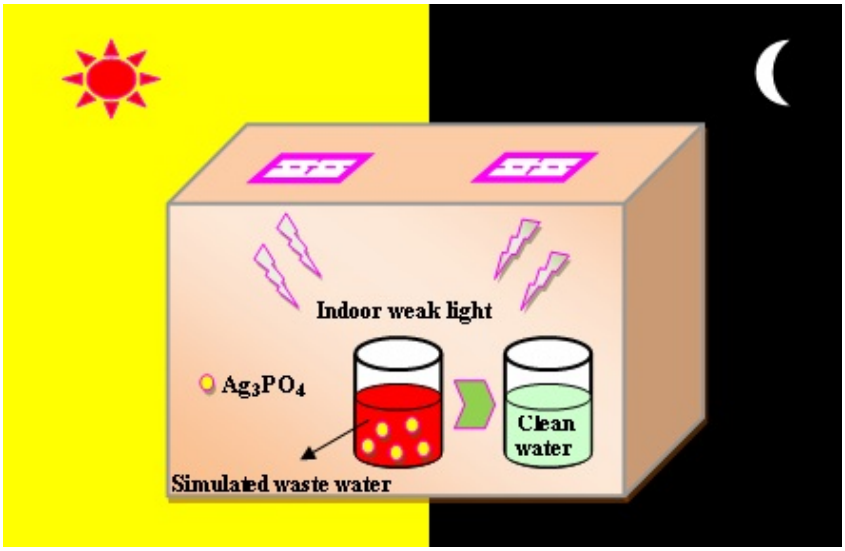

Fig 4.6 Diagrammatic sketch of natural indoor weak light degradation of simulated wastewater by Ag_3PO_4.

area and has two windows with the size of 120 *180 cm^2. The temperature of the room is measured to be 16 °C at daytime and 8 °C at night, respectively. The dye solution containing photocatalyst was kept stirring and degraded by the natural light through the windows over day and night, without any artificial light source. The light density at the liquid surface is measured by an irradiatometer (FZ-A type, Handy, China). The average light density during the daytime is 72 cd, while it is 28 cd at night. The determination of the liquid concentration is the same as that the evaluation under visible light. For RhB-MO mixture wastewater, 200 mL of 10 mg/L RhB and 10 mg/L MO are employed. The pH values of all the solutions are tested to be approximately 6.

4.5 Stability test

The stability of Ag_3PO_4 is investigated by circulation experiment in this thesis. Typically, 0.1 g Ag_3PO_4 sample is dissolved in 200 mL dye solution (10 mg/L RhB). The suspension was stirred for 30 min to reach an adsorption–desorption equilibrium of dye molecules on the surface of photocatalyst. The dye solution is degraded by Ag_3PO_4 sample to the completion of reaction (absorbance of solution no longer changes). The absorbance of solution is tested every 5 min by twice and the used liquid sample is poured back into the beaker. After the reaction, the used Ag_3PO_4 sample is collected by high speed centrifugation (10000 r min^{-1}). The sample is washed by deionized water and dried at 60 ºC. The dry powder is weighed by analytical balance to ensure that the weight has not changed. In this work, the weight loss of sample between each run is less than 0.005 g. Then the recovered sample is dropped into another 200 mL dye solution (10 mg/L RhB) for the second run. This process is repeated for 5 cycles and the ending absorbance of each cycle is recorded. The stability of the sample is evaluated by comparing the ending absorbance value of dye solution after each run. No obvious difference between the first run and the fifth run, indicating the stability of the sample is fine. This method can be used to study the activity of sample after repeated utilization, thereby reflecting the stability of the sample. Moreover, in chapter 7, the SEM image and XRD pattern of samples after

circulation experiment are displayed. The stability of Ag_3PO_4 is studied by different samples under visible light and natural light.

4.6 Summary of Chapter 4

The theories of data collection and analysis in this work are stated in this chapter. The synthesis technique and characterization methods used in this work are discussed in detail. The work mechanisms of equipments for characterization are also introduced in this chapter. Besides, the typical preparation methods of photocatalysts and evaluation method for photocatalytic activity of the catalysts are presented.

Chapter 5 Ag_3PO_4 microtubes with improved photocatalytic properties under visible light irradiation

Since structure and surface properties can significantly affect the activity of photocatalyst. It was reported that Ag_3PO_4 cubes [113], dodecahedrons [114] and tetrapods [115] have been synthesized. These Ag_3PO_4 photocatalysts with specific structures all show higher photocatalytic activity for dye degradation than bare Ag_3PO_4. In this chapter, the Ag_3PO_4 microtubes (SPMs) are introduced by a one-pot synthesis using polyethylene glycol 200 (PEG 200) as the reaction medium. The properties of the catalyst are investigated by scanning electron microscope (SEM), X-ray diffraction (XRD), transmission electron microscope (TEM) and N_2 adsorption-desorption. It is found that PEG 200 plays a vital role in the formation of the tube-like structure. The crystal growth and self-assembly process of SPMs are propsed. Under visible light irradiation (≥420 nm), the sample exhibits a greatly higher photocatalytic activity for the degradation of RhB than solid Ag_3PO_4 and Ag_3PO_4 tetrapods, which has been mainly ascribed to the hollow structure. Moreover, the influence of pH value on degradation efficiency by SPMs has been investigated. The pH values of organic dye solutions are adjusted to 1, 7 and 12 by HNO_3 and NaOH to study the photocatalytic performance of SPMs under acidic, neutral and alkaline conditions, respectively. As it is known, photo corrosion is a pervasive

problem which occurs on many silver salts. This is mainly attributed to the slightly solubility of silver salts in aqueous system, resulting in the reduction of released silver ions by photo-induced electrons. Therefore, the stabilities of SPMs under different pH values are studied by circulation experiment.

5.1 Morphology and properties of SPMs

The specific tube-like structure of SPMs is studied via the characterization results of X-ray diffraction (XRD), scanning electron microscopy (SEM), transmission electron microscope (TEM) and nitrogen ad-desorption. Moreover, a possible formation mechanism of the SPMs which involves the reaction medium of polyethylene glycol 200 (PEG 200) is presented.

5.1.1 Characterization of SPMs

Fig. 5.1 shows the X-ray diffraction (XRD) patterns and scanning electron microscopy (SEM) images of the silver phosphate microtubes (SPMs). It can be seen from **Fig 5.1a** that all the diffraction peaks of SPMs are in good correspondence with standard Ag_3PO_4 (JCPDS No. 06-0505), confirming the purity of SPMs. **Fig 5.1b, c and d** show the SEM images of SPMs at low and high magnifications, respectively. It can be observed that the sample consists of many hollow tubes with average length of 8 μm and diameter of 1.5 μm. Broken pieces of Ag_3PO_4 can be observed Form the

inset of **Fig 5.1 b** and the positions circled out with red in **Fig 5.1 d**, displaying the interior structure of the SPMs. The hollow structure of the SPMs can be confirmed by the internal void.

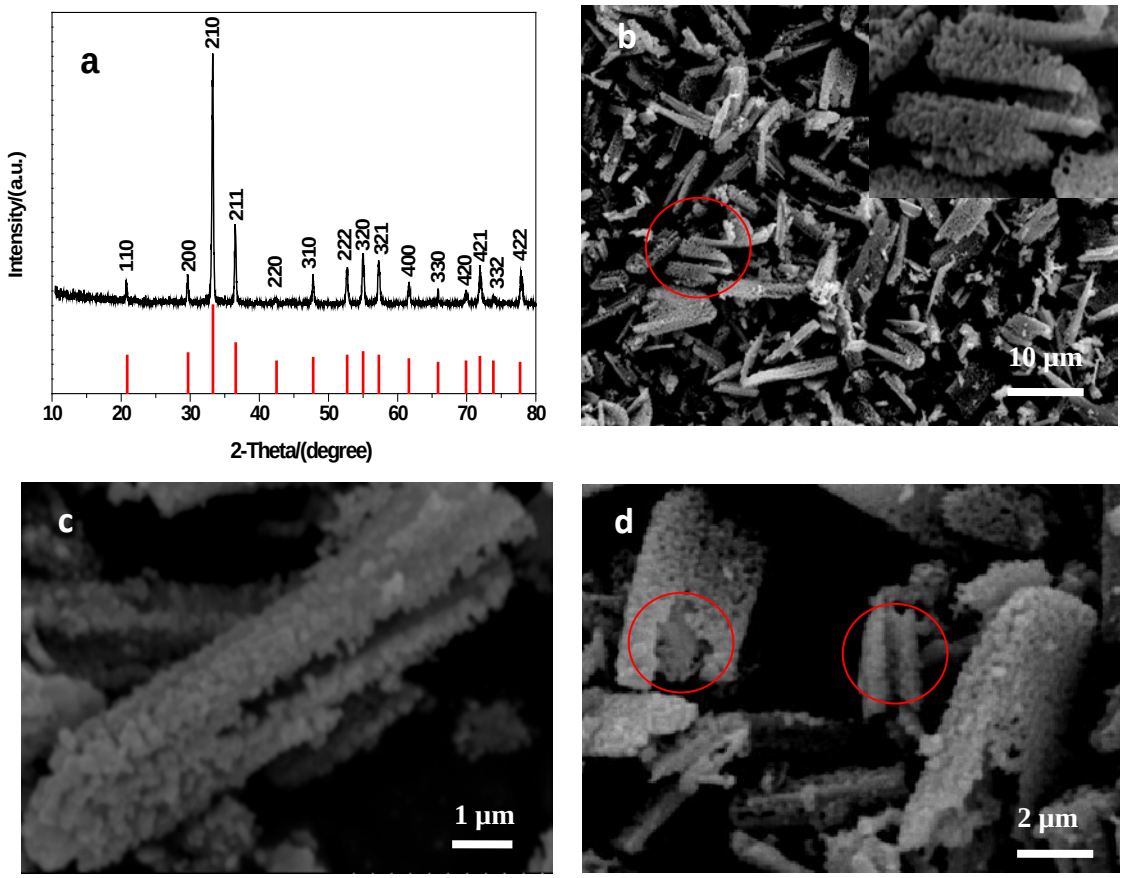

Fig 5.1 XRD patterns (a) and SEM images of the silver phosphate porous microtubes (SPMs) (b) low magnification with an inset; (c, d) high magnification.

Moreover, the sample has been calcined at 200 ºC for 2 h with protection of flowing gas of nitrogen. The purity of the nitrogen used is 99.99 %, and the flowing rate is controlled to be 100 mL min^{-1}. It can be seen from **Fig 5.2** that the surface of SPMs becomes smooth compared with that prior to calcination. This could be ascribed to the poor thermal stability of Ag_3PO_4. Notably, the structure of the most

SPMs has been maintained after heating, indicating the stable microstructure of the SPMs. From **Fig 5.2** inset, the hollow structure of the SPMs has been proved again. The SPMs are further made of large numbers of uniform nanoparticles with an average diameter of 100 nm, which is much smaller than the Ag_3PO_4 samples reported in the previous literatures (more than 1 μm). **Fig 5.3** shows the images of SPMs after ultrasonic treatment (frequency 20 kHz) in water by different times. After 5 h ultrasonic treatment, half of the SPMs has been shattered into pieces or large particles due to the ultrasonic treatment. Anyway, there are still a number of Ag_3PO_4 maintaining the tube-like structure after long duration ultrasonic treatment, confirming the structure of SPMs is not easily broken up. When the treatment duration increases to 10 h, the structure of most of the SPMs has been destroyed and only small pieces can be observed. Large amounts of nanoparticles can be seen at the surface of the SPMs pieces. As it is known, millions of cavitation bubble generate in water per second under ultrasonic condition, due to the vibration of liquid caused by ultrasonic transmission. The strong impact force caused by the violent blasting blast could broke up solid into the minimum unit. Therefore, the SPMs are constructed by these nanoparticles. The small dimension of photocatalyst might favors for the degradation reaction of pollutants due to the small dimension effect [192]. The specific tube-like structure and small particle size would endow SPMs with a large surface area, which favors for the pollutants adsorption.

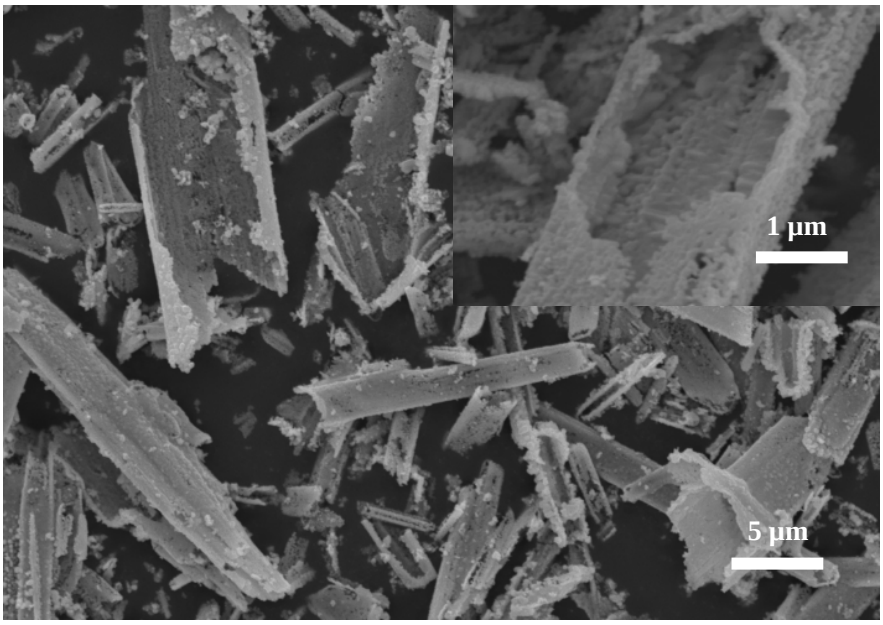

Fig 5.2 SPMs after calcination, Inset: image with high magnification.

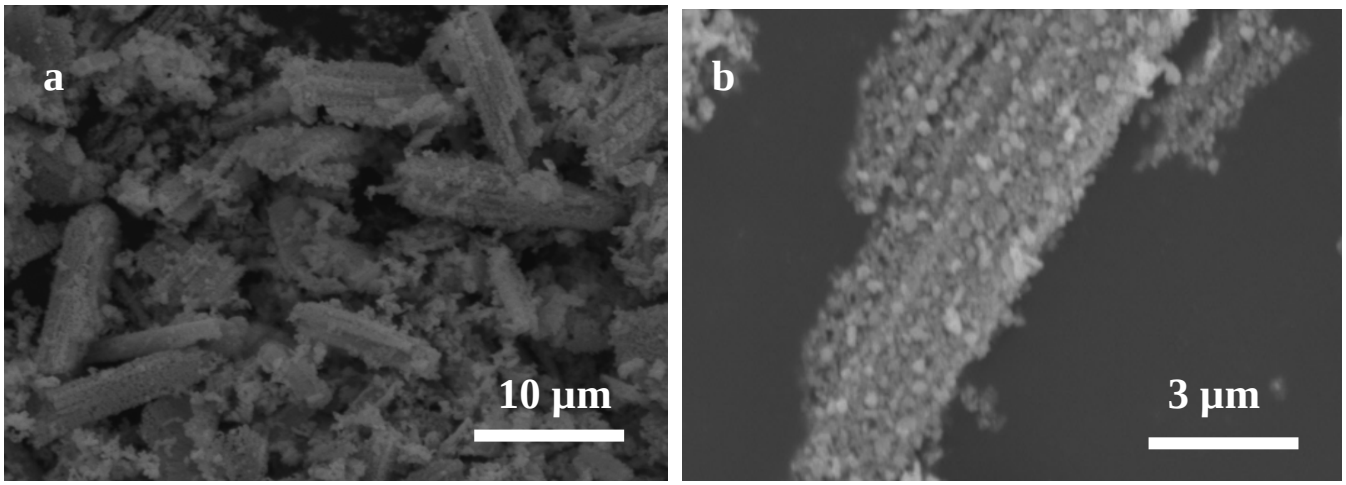

Fig 5.3 SPMs after ultrasonic treatment at different times: (a) 5 h, (b) 10 h.

Nitrogen adsorption is used to analyze the physical surface property of SPMs. The nitrogen adsorption-desorption curves of SPMs is shown in **Fig 5.4**. The curves range from 0-0.8 relative pressure are almost parallel to the x axis, indicating that the interaction force between gaseous nitrogen and SPMs is very weak. There is little gaseous nitrogen adsorbed by the material as the relative pressure increases, indicating that SPMs might be a non porous or macroporous material. The surface

area of SPMs is calculated to be 7.2 m^2 g^{-1} according to the nitrogen ad-desorption curves by the Brunauer-Emmett-Teller (BET) method. The calculation procedure refer to the BET equation introduced in experimental chapter. Although the specific surface area of SPMs is as low as 7.2 m^2 g^{-1}, it is still higher than that of solid Ag_3PO_4 microcrystals (1.5 m^2 g^{-1}) and of Ag_3PO_4 microcubes (5.6 m^2 g^{-1}) reported by Liang et al. [193]. This could be ascribed to the hollow structure and the small dimension of single component unit of SPMs.

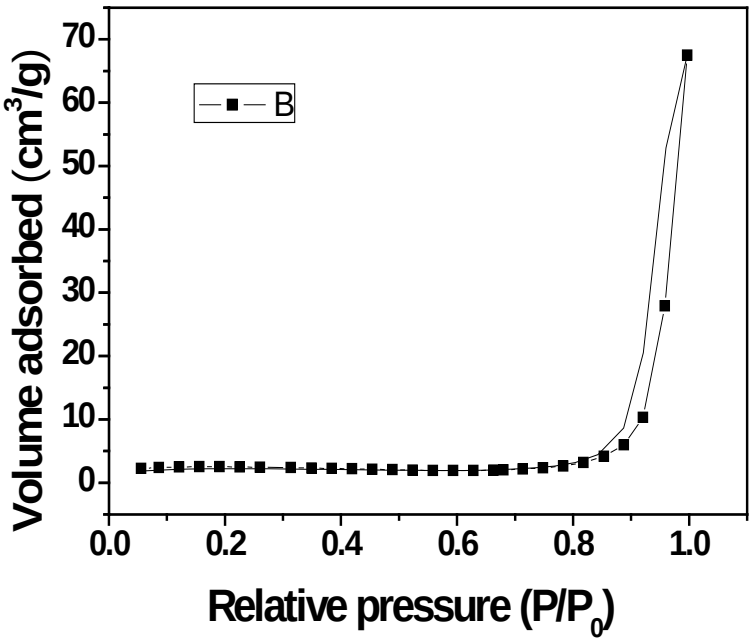

Fig 5.4 Nitrogen ad-desorption curves of SPMs.

Fig 5.5a displays the transmission electron micrographs (TEM) image of SPMs. It can be clearly observed that the SPMs consist of small nanoparticles due to the light

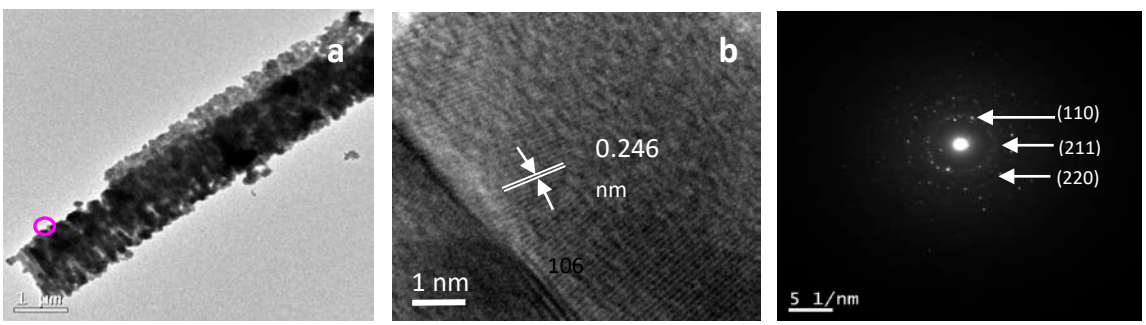

Fig 5.5 Structure and surface property of SPMs: (a) TEM image; (b) HRTEM image; (c) SAED image

and shade contrast of the spots. The tiny voids in the picture indicates that light can pierce through the SPMs, thus allowing light reflection inside the SPMs. The light reflection can cause the repeated light absorption by the SPMs, enhancing the utilization efficiency of light energy. Among the known studies of Ag3PO4, there is few reports on the lattice fringes in-situ analysis by the characterization of HRTEM and SAED. Because most of Ag_3PO_4 samples are thick and with large dimension. The electron beam can not penetrate the material, thus most of the studies on Ag_3PO_4 planes are based on computer calculation. The SPMs are with a length of 8 μm and a diameter of 1.5 μm. However, the single unit composed the SPMs is with a dimension of 100 nm, allowing the electron beam penetration for in-situ analysis. **Fig 5.5b, c** show the lattice fringe and selected area electron diffraction (SAED) of SPMs. The single lattice fringe spacing is determined to be 0.246 nm, corresponding to the (211) planes of silver phosphate (JCPDS No. 06-0505). Normally, SAED characterization of single crystal is displayed as square lattice, while that of polycrystalline is presented as diffraction rings. The clear diffraction rings in **Fig 5.5c** reveal its polycrystalline nature. By measuring the distance from the rings to the centre can obtain a value stands for a specific crystal plane. The value can be calculated by the equation: d = (1/L)/s, where L is the distance from the ring to the centre, s is the space scale. In the SAED of SPMs, (110) plane has also been discovered by calculating the value d. In previous studies of Ag_3PO_4 facets [191], it has been demonstrated that {110} facets of Ag_3PO_4 have the highest activity for the degradation of dyes when compared with other facets.

5.1.2 Formation mechanism of SPMs

It is found that the specific hollow structure of SPMs plays an important role in enhancing photocatalytic activity for dye solution degradations. The possible formation mechanism of SPMs is investigated here. The plausible formation process of SPMs is proposed and described in **Fig 5.6**. It has been reported [194] that the hydrophilic CH_2-CH_2-O in PEG 200 can easily form a chain-like structure. The Ag^+ could complex with CH_2-CH_2-O to form "Ag-PEG", by which the Ag^+ could be restricted in ordered sequence. It is assumed that those substances forming similar dominant intermolecular attraction can be dissolved by each other. Hence silver acetate is used in our work for the dissolution of Ag ions. When H_3PO_4 is added to the system, the Ag_3PO_4 nucleus would form in the initial position of the Ag ions and keep the chain structure. The Ag_3PO_4 nucleus then grow into particles and connect attributed to that lateral growth favors for the formation of ordered structure due to the surface tension of crystal particles [195, 196]. In the growth process of SPMs, Ag_3PO_4 particles in linear finally grow into Ag_3PO_4 chains. The structure is similar with the necklace-like Ag/Ag_3PO_4 reported by Bi et al [197]. The difference is that they use Ag wire as a string, anyway, the PEG will be removed after the formation of "chains". The "chains" in the same direction aggregate or self-assemble to form a tube structure so as to reduce the surface energy [198].

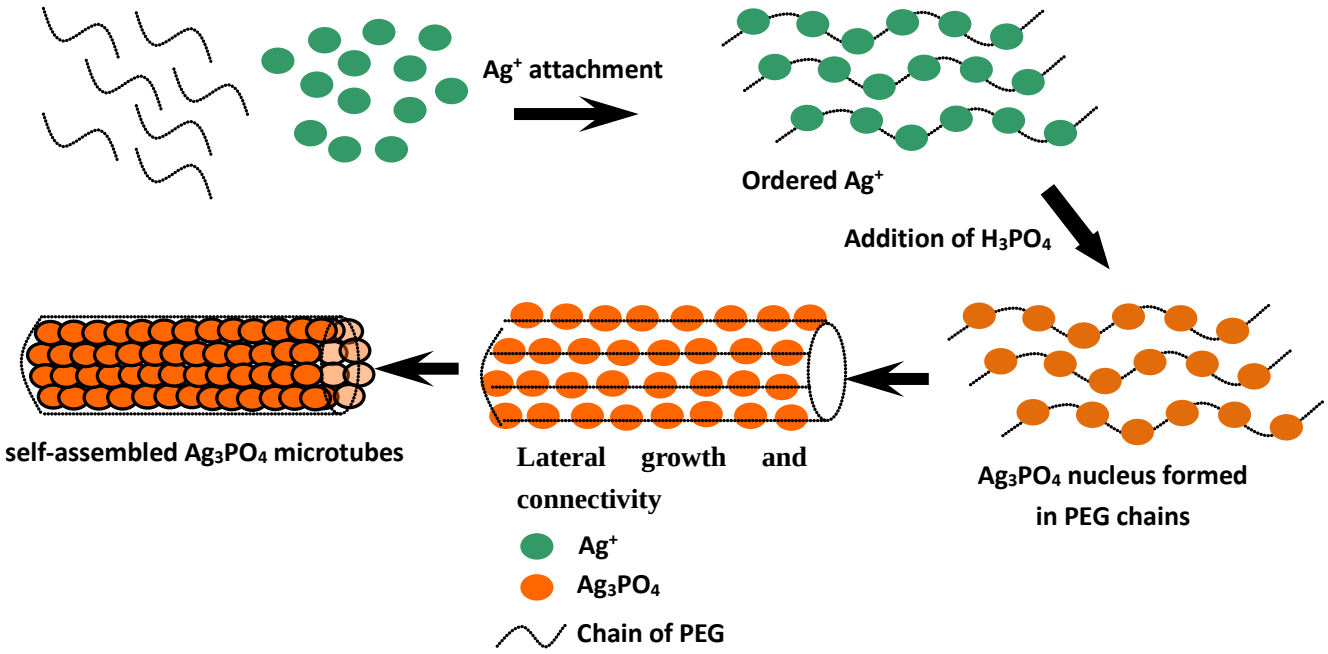

Fig. 5.6 Schematic formation diagram of SPMs

We have tried to investigate the influence of PEG concentration in the system by adjusting the ratio of PEG and water. However, only irregular particles were obtained when water was used in the system. We suspect that when water is used, the CH_2-CH_2-O chain can easily react with water to form the stable CH_2-CH_2-OH, which is a hydrate, thus refraining the formation of the "Ag-PEG" complexes. Otherwise, the viscosity of solution is an important factor in the growth process of crystal. Solution with high viscosity will slow down the growth of nucleus in the system. In pure PEG system, the growth rate of Ag_3PO_4 particles is very slow due to the high viscosity of PEG 200. The addition of water would decrease the concentration of PEG, resulting in increasing growth rate of Ag_3PO_4 nucleus. The Ag_3PO_4 nucleus rapidly grows into large size particle without bonding with CH_2-CH_2-O molecule chain, leading to the irregular solids of Ag_3PO_4. This could be

reason that the SPMs can not be prepared in PEG/water system. Consequently, PEG plays a vital role in the formation of SPMs and it could be used as a soft template reagent in the preparation of other semiconductors.

5.2 Photocatalytic activity of SPMs

The photocatalytic activities of SPMs are tested by degrading individual dyes and mixed dyes under visible light irradiation, respectively. The difference of photocatalytic activity of the SPMs for different dye degradation is studied. For comparison, the photocatalytic activities of Ag_3PO_4 tetrapods, solid Ag_3PO_4 crystal and P25 TiO_2 are also tested under same conditions.

5.2.1 Individual dye degradation by SPMs

The photocatalytic activities of the samples are evaluated by the degradation of rhodamine B (RhB) and methyl orange (MO). Except for SPMs, tetrapod-like Ag_3PO_4, solid Ag_3PO_4 and P25 powder are also used in the degradation to compare their activity. The absorbance of dye solution (C) is tested every three minutes by a spectrophotometer. The initial absorbance of dye solution is set as C_0. The concentration of organic dye is presented as. The x axis and y axis of the degradation curves are time (min) and C/C_0, respectively. **Fig 5.7a, b** show the degradation and kinetic curves of RhB over the samples under visible light irradiation (≥420 nm) at room temperature. It can be clearly observed from **Fig 5.7a** that RhB dye can be completely decolorized by SPMs within 10 minutes. 20 minutes and more than 35 minutes are needed for the complete degradation of RhB by the tetrapod-like and solid Ag_3PO_4, respectively. For the P25 powder, approximately 29 percent of RhB is

removed in 45 min. The removal of RhB by P25 powder under visible light could be mostly due to the dye sensitization of P25 by RhB dye [199]. By changing the y axis of the degradation curve to ln (C_0/C), the slope k (apparent degradation rate constant) of the new curve can be obtained by first order reaction equation Y= k*A+B. The apparent degradation rate constants of the sample are calculated to be k_{SPMs}=0.33051 min^{-1}, k_{Tet}=0.14167 min^{-1}, k_{solid}=0.08237 min^{-1}, k_{p25}= 0.00737 min^{-1}, which are ascribed to **Fig 5.7b**. The results indicate the degradation rate of RhB over SPMs is 2.5, 4 and 45 times that of the tetrapods, solid Ag_3PO_4 and P25 powder, respectively. We believe that the specific hollow structure play a very important role in the excellent photocatalytic performance of SPMs. As shown in **Fig 5.8a**, it is acknowledged that when light reaches semiconductor surface, some of the light energy would be absorbed by semiconductor to generate photo carriers, while the other energy would be reflected and waste. Nevertheless, the hollow structure of SPMs enables multiple scattering of light, leading to multiple absorption of light energy. The multiple absorption of energy can effectively increase the utilization efficiency of visible light by SPMs, thus enhancing the photocatalytic performance.

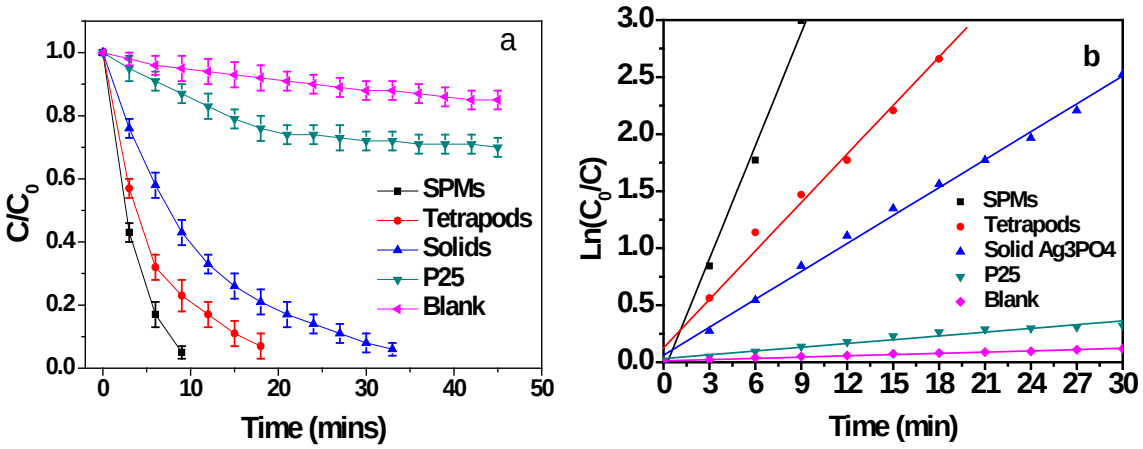

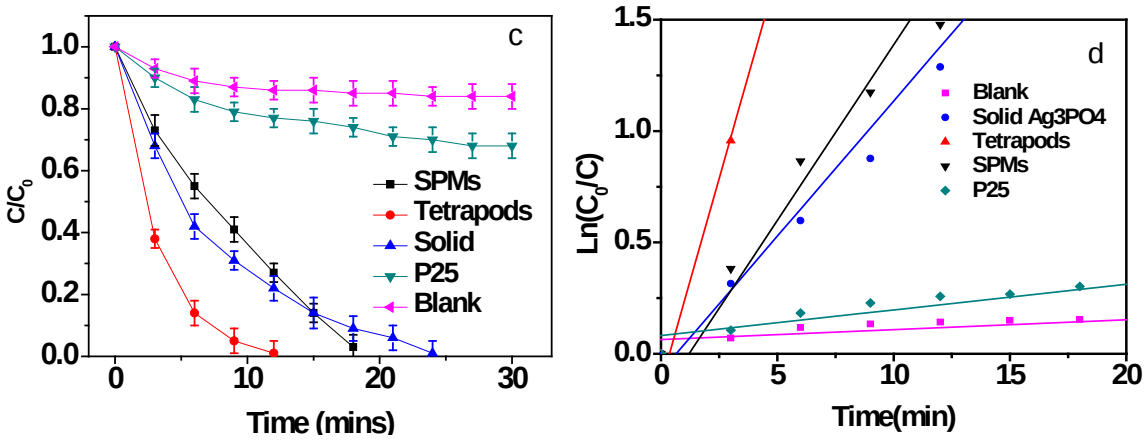

Fig 5.7 Degradation and kinetic curves of organic dyes by SPMs, tetrapods, solid Ag_3PO_4 and P25 powder under visible light irradiation (≥420 nm): RhB (a, b); MO (c, d)

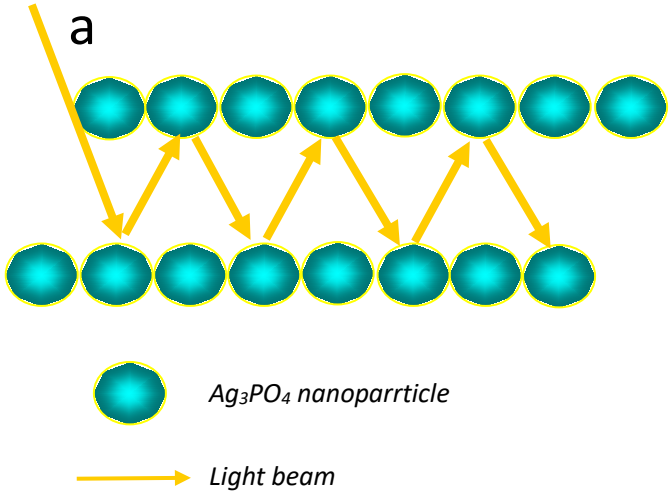

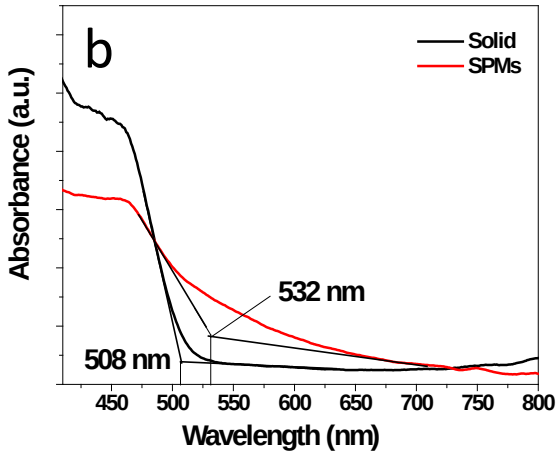

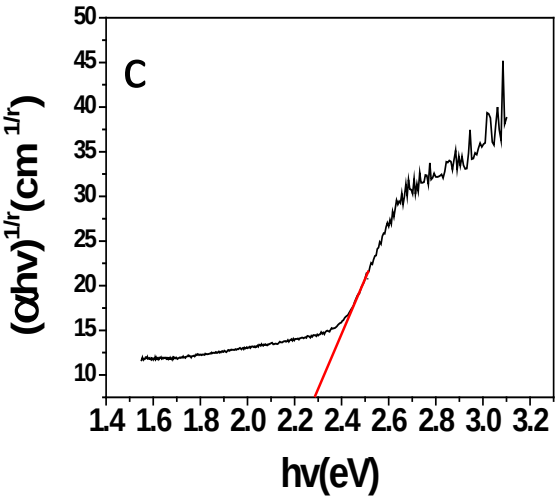

Fig 5.8 Schematic diagram of light scattering of the SPMs (a), UV-vis diffuse reflectance spectra (UV-DRS) of the SPMs and solid Ag_3PO_4 (b) and Tauc plot curve of the SPMs (c)

Normally, the reduction of particle size would increase the band gap of semiconductor and cause a blue shift of reflectance spectra. However, a red shift of UV-vis diffuse reflectance spectra is observed for SPMs, as shown in **Fig 5.8b**. This may be because that the smaller blue shift caused by the reduction of particle size counteracted by the larger red shift due to the formation of surface status [200]. The red shift endows SPMs with a higher absorption efficiency of visible light, which favors for better photocatalytic reactions. Furthermore, the absorption spectra of the SPMs are shown in **Fig 5.8c.** The direct and indirect allowed transitions of the SPMs can be determined by Tauc plot curve, in which quantity hv (the energy of light) on the x axis and quantity $(\alpha hv)^{1/r}$ on the y axis. Light energy hv can be calculated by $hv= 1240/\lambda$, where λ is the wavelength of absorption edge. α is the absorption coefficient of the material. The absorption coefficient α can be obtained as follows:

$$\alpha= A/bc \qquad (33)$$

Where A is the absorbance of solution. b is the absorption path of solution. c is the

concentration of solution. The absorption path of solution b is measured to be 1 cm. The concentration level c is 20 mg L^{-1}. r equal to 1/2 or 2 for direct or indirect (band gap energy commonly) allowed transition, respectively. The Tauc plot curve is displayed in **Fig 5.8c**. The tangent line (red) of the fitting curve indicates the band gap energy of SPMs is approximately 2.28 eV, confirming the activity under irradiation in visible light region. In conclusion, SPMs have the highest activity for the degradation of RhB under visible light compared with the other samples. The greatly high activity of SPMs could be attributed to the specific structure, small particle size and large surface area. **Fig 5.7c, d** present the degradation and kinetic curves of MO by the samples under visible light at room temperature. Interestingly, the results are in big difference with that of RhB degradation. For the degradation of MO, the tetrapod-like Ag_3PO_4 shows the highest activity among all the samples, follows by SPMs, solid Ag_3PO_4 and P25 powder. It can be seen from **Fig 5.7c** that 12 min, 18 min and 24 min are necessary for the tetrapods, SPMs and solid Ag_3PO_4 to completely degrade the MO solution. 32 percent of MO is removed by P25 in 30 min due to the dye sensitization process. The apparent degradation rate constants of the samples are as follows: k_{SPMs}= 0.16913 min^{-1}, k_{Tet}= 0.36861 min^{-1}, k_{solid}= 0.15773 min^{-1}, k_{p25}=0.08237 min^{-1}. Compared with the degradation of RhB, the degradation rates of MO over the tetrapods, solid Ag_3PO_4 and P25 powder are increased by 1.6, 0.9 and 10 times, respectively. On the contrary, the degradation rate of MO by SPMs significantly reduced (49% reduction of reaction rate) comparing with that of RhB. The difference of reaction rate between RhB and MO degradations could be explained by the different dye molecule structure and selective adsorption of the two dyes.

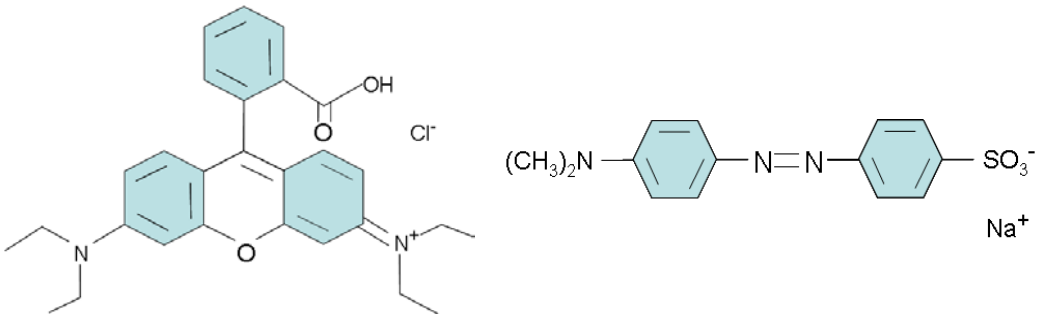

Fig 5.9 Molecular structures of RhB (left) and MO (right)

Fig 5.9 displays the molecule structures of RhB and MO dyes. It can be observed that the molecule structure of RhB is more complicated than that of MO, not only due to more benzene ring but also more kinds of chemical bonds. The main chromogenic group of MO is –N=N–, while that of RhB is the conjugated xanthene ring [201]. The bond energy of conjugated xanthene ring (882kJ/mol) is greatly higher than that (418 kJ/mol) of –N=N–. Hence it requires more energy to degrade RhB molecule compared with MO. Moreover, the degradation of RhB may generate intermediate products such as benzyl acid and alizaric acid [79], which hinders the further degradation of RhB. Hence the RhB dye is more difficult to be degraded than the MO dye. Therefore, except for SPMs, the degradation rates of MO by the samples are faster than that of RhB. However, for SPMs, the degradation rate of RhB is faster than that of MO. This is because the adsorption of RhB by SPMs is better than that of MO. As it is known, RhB is considered to be a cationic dye while MO is an anionic dye. Cationic molecules are easy to be captured by semiconductor with negatively charged surface due to the strong attractive power between opposite electrification. The surface of SPMs might be with negative charge attributes to the ether bond of the residual PEG molecules on SPMs surface. Because the PEG molecules are difficult to be absolutely removed by washing with water and ethanol.

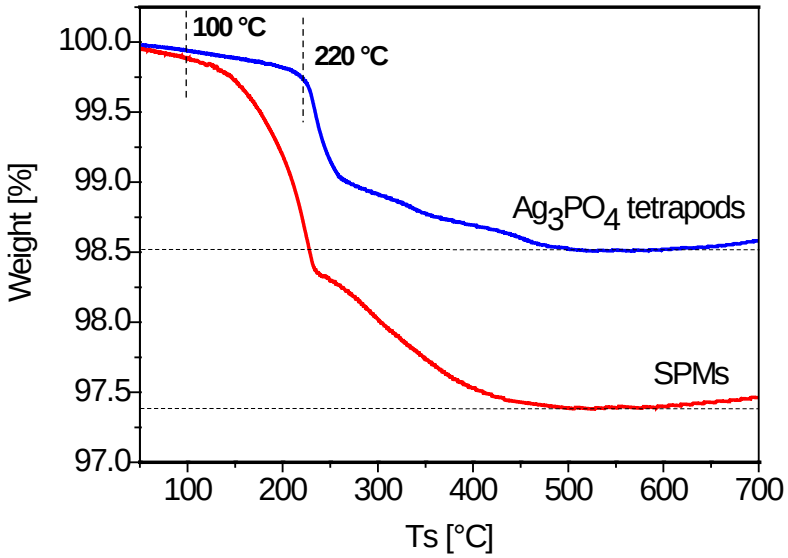

Fig 5.10 Thermogravimetric curves of Ag_3PO_4 tetrapods and SPMs range from 50 to 700 ºC.

Fig 5.10 presents the thermogravimetric curves of Ag_3PO_4 tetrapods and SPMs range from 50 to 700 ºC under flowing air condition. It can be observed that only a slight weight loss (0.06% and 0.13% of Ag_3PO_4 tetrapods and SPMs, respectively) from 50 to 100 ºC, indicating both of the samples are dry and with little moisture. There has been little report on Ag_3PO_4 via thermogravimetric analysis (TGA). Although the melting point of Ag_3PO_4 is known as high as 849 ºC, Ag or Ag_2O would easily form by heating or exposure to light [95]. The blue curve of Ag_3PO_4 tetrapods in **Fig 5.10** starts to fall sharply at 220 ºC and the sample loss 0.98% of weight at 260 ºC. After that, the weight of Ag_3PO_4 tetrapods continueously reduces to the end of heating, which is reflected by a smooth decline curve. The total weight loss ratio of Ag_3PO_4 tetrapods is measured to be 1.49%. However, the obvious weight loss of SPMs occurs at much lower temperature. The weight ratio of SPMs decreases as high

as 1.31% prior to 220 ºC, and continueously decrease after 220 ºC till the end of heating. The total weight loss ratio of SPMs is measured to be 2.62%. Interstingly, the weight loss ratio of SPMs is 1.28% from 100-220 ºC, which is approximately 6 times that of the tetrapods (0.20%). The rapid weight loss of SPMs from 100~220 ºC can be attributed to the libration of the residual PEG molecules on SPMs surface. Because starting from 100 to 300 ºC, moisture, organic compounds and some unstable solid will be oxidized by oxygen one after another, resulting in mass loss of the initial material. Compared with the slight weight loss of the tetrapods, the rapid weight loss of SPMs prior to 220 ºC is most likely caused by the removing of the residual PEG molecules on catalyst surface. The exsiting of the PEG molecules leads to the negatively charged surface of SPMs. The strong attractive power between cationic RhB molecules and negatively charged surface endows SPMs with good adsorption of RhB and led to the fast degradation rate. Consequently, the SPMs exhibit a good photocatalytic activity for RhB due to not only its small particle size, large surface area and hollow structure, but also the selective adsorption of pollutants.

5.2.2 Mixture dye degradation by SPMs

As it is known, actual industrial wastewater generally contains more than one kind of pollutants. Therefore, it is an urgent need to find an effective way to deal with complicated multi-pollutants wastes. In our studies, photocatalytic degradations of RhB/MO mixture dyes over Ag_3PO_4 are investigated. **Fig 5.11** shows the degradation curves of RhB/MO mixture dye solution by SPMs, tetrapods and solid Ag_3PO_4 under

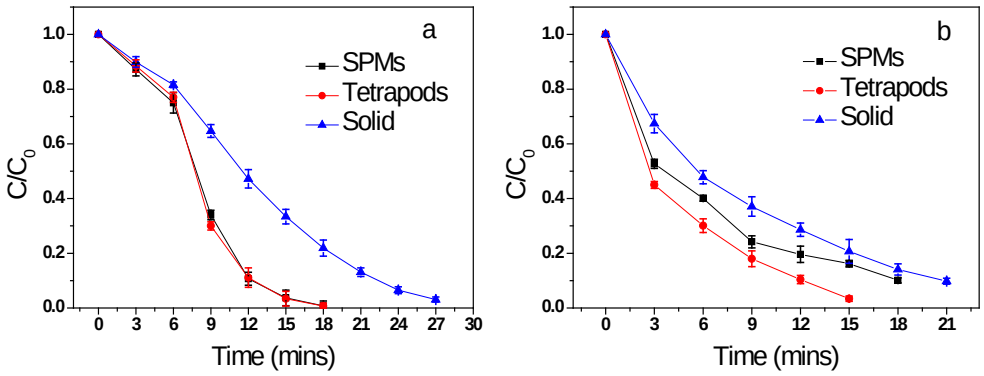

Fig 5.11 Mixed dye degradation by SPMs under visible light irradiation (>420 nm): (a) RhB; (b) MO

visible light. The results indicate RhB/MO mixed aqueous solution can be mostly degraded by SPMs and Ag_3PO_4 tetrapods within 20 minutes, while 1 hour is needed for TiO_2 reported in previous literature [202]. The degradation rate of MO was very fast at the beginning and slowed down over time. On the contrary, the degrading rate of RhB was slow at initial stage, then it has a rapid increase as the reaction carried on. According to the study of individual pollutants, the changes of degradation rates of RhB and MO can be explained by the competitive adsorption [203] and the changes of concentration. As it is known, MO is considered to be an anionic dye while RhB is a cationic dye. The molecules of MO adsorbed on the surfaces of tetrapods and solid Ag_3PO_4 (which are positively charged) prior to RhB, resulting in faster degradation of MO. As the concentration of MO decreases, RhB molecules begin to occupy a dominant adsorption on the catalyst surface due to its high concentration in the system. In a word, SPMs and tetrapod-like Ag_3PO_4 can effectively degrade the RhB/MO mixture dye solution under visible light. The results illustrate that it could be a promising method to deal with industrial wastewater by Ag_3PO_4 photocatalyst under

visible light.

5.3 Influences of dosage and pH value

Apart from catalyst itself, reaction conditions also significantly affect the degradation rate of wastewater. Ideal reaction conditions can maximize the capacity of catalyst and favor for efficient degradation of pollutants [25]. The dosage of used catalyst is an important factor in practical wastewater treatment process. The dosage below the optimal value will lead to low working efficiency of catalyst. On the contrast the dosage exceeds the optimal value will cause the waste of catalyst. Hence, it is necessary to find the most suitable dosage to realize the maximum utilization efficiency of catalyst. Bisides, there is no doubt that pH value is a very important factor in aqueous reaction system, as well as in wastewater treatment. Herein, rhodamine B (RhB) and methyl orange (MO) are degraded by the SPMs under acidic, neutral and alkaline conditions, respectively. The solutions with different conditions of acidic, neutral and alkaline are prepared by adding proper amount of NaOH or HNO_3 solution. RhB, MO and their mixed dyes were degraded by SPMs at different pH values under visible light irradiation (>420 nm), respectively.

5.3.1 Effect of dosage

Suitable catalyst dosage will also affect the degradation rate of the dye solution. Under same reaction condition, too much catalyst would cause agglomeration which decreases the degradation rate. On the contrary, too little catalyst dosage would also

lead to low degradation efficiency.

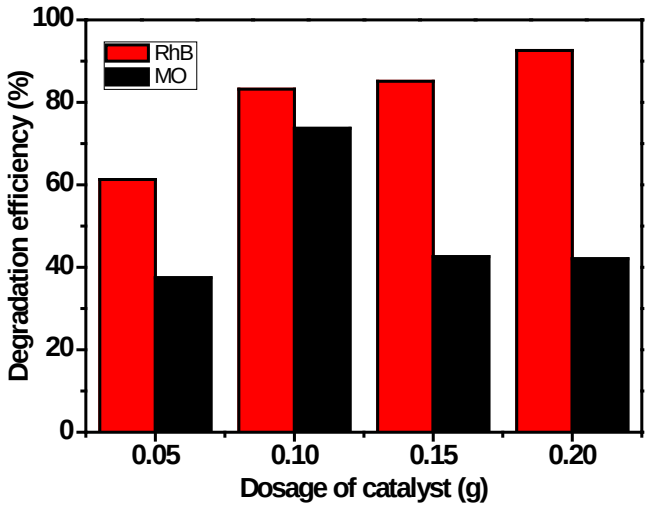

Fig 5.12 Degradation efficiency of RhB and MO with different catalyst dosages in 10 min.

Therefore, we have investigated the effect of the catalyst dosage on the photocatalytic degradation by control the mass range from 0.05 g to 0.2 g in 200 mL RhB and MO (10 mg/L), respectively. The reaction duration of both RhB and MO is controlled to be 10 min. The results in **Fig 5.12** shows 0.1 g catalyst has the fastest degradation rate for MO solution; while the most suitable dosage for the degradation of RhB is 0.2 g. It has been reported that increasing of catalyst dosage could provide more ·OH free radicals due to the increase of the generated carriers [204]. However, too much amount of catalyst would cause aggregation effect, leading to the reduction of irradiation efficiency, further reducing the photocatalytic activity [205-208]. In summary, 0.1 g SPMs could be the most reasonable dosage for the degradation of RhB and MO under same condition.

5.3.2 Effect of pH on the degradation of individual dyes

In our experiment, RhB dye is degraded by SPMs at acidic, neutral and alkaline conditions, respectively. **Table 5.1** shows the amounts of NaOH and HNO_3 which are used to adjust pH value of solutions**. Fig 5.13a** shows the degradation curves of RhB at pH 1, 7 and 12. It can be observed that under acidic condition (pH=1), the SPMs have the highest degrading rate for RhB degradation. 89.7% of RhB has been degraded within 15 minutes at pH=1, while 59.7 and 35.6 percet of RhB are removed under pH=7 and 12 in the same duration, respectively. **Fig 5.13b** presents the apparent reaction rate of RhB degradation at pH 1, 7 and 12, respectively. By changing the y axis of the degradation curve to ln (C_0/C), the slope k (apparent degradation rate constant) of the new curve can be obtained by first order reaction equation $Y=k*A+B$. The apparent reaction rate constants of RhB are determined to be 0.14104, 0.05556, and 0.02932 min^{-1} when pH value is 1, 7 and 12, respectively. The degradation rate of RhB by SPMs at pH=1 is 2.53 and 4.8 times that of at pH= 7 and 12, respectively. The results indicate the photocatalytic activity of SPMs under acidic conditon is higher than that under neutral and alkaline conditions. **Fig 5.13c, d** show the degradation and reaction kinetic curves of MO under pH 1, 7 and 12, respectively. The reaction kinetic constants of MO are 0.0994, 0.02779, 0.01503 min^{-1} at pH 1, 7 , 12, respectively. The degradation rate of MO by SPMs at pH=1 is 3.57 and 6.63 times that of at pH= 7 and 12, respectively. It is found that within 15 minutes, SPMs degrade about 76.6% of RhB at pH=1 condition, which is much higher than that at pH 7(33.7 % removed) and 12 (20.5 % removed). To conclude, the acidic condition favors for the degradation of RhB and MO dyes by SPMs under visible light irradiation.

Table 5.1 Degradation efficiency of RhB and MO by SPMs at pH values of 1, 7 and 12

pH value (RhB solution)	$(1-C/C_0)\times100\%$ RhB	pH value (MO solution)	$(1-C/C_0)\times100\%$ MO
1	89.7%	1	76.6%
7	59.7%	7	33.7%
12	35.6%	12	20.5%

Irradiation time: 15 min; weight of Ag_3PO_4: 0.1 g

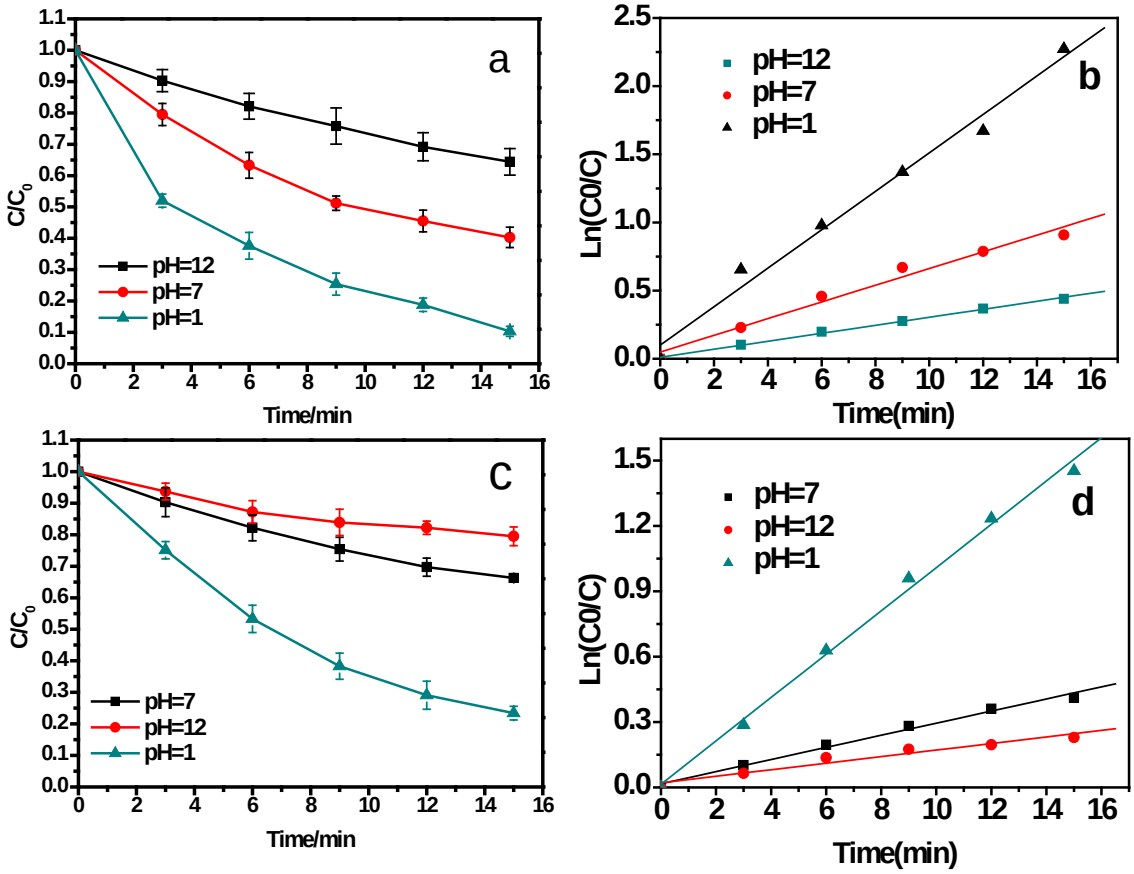

Fig 5.13 Degradation and apparent kinetic curves of RhB and MO by the SPMs: (a, b) RhB; (c, d)MO

Furthermore, **Fig 5.14** shows the optical absorption of RhB and MO under pH 1, 7 and 12. **Fig 5.14a** presents optical absorption of RhB at different pH values,

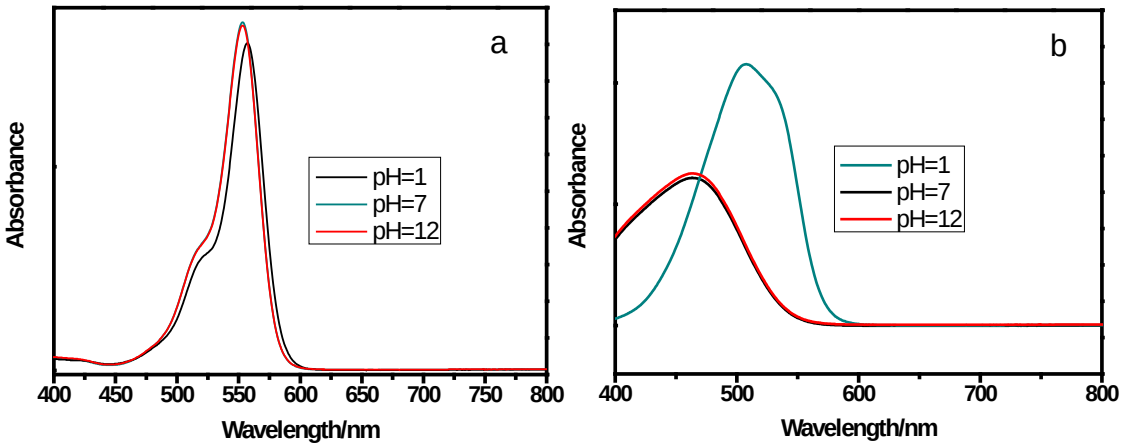

Fig 5.14 UV-vis absorption spectra of RhB (a) and MO (b) at different pH values: 1, 7 and 12

indicating that the change of pH will not destroy the conjugated structure of RhB. However, the degradation efficiency of RhB under acidic condition is much higher than that of under neutral and alkaline conditions. This is ascribed to that the concentration level of H^+ is different under different pH values, significantly affecting the generation amounts of reactive species (HO_2,$^{\cdot}O_2^{-\cdot}$, h^+ and ·OH) [208, 209]. Due to the conduction band position of +0.45 eV, $O_2^{-\cdot}$ and $HO_2^{\cdot}$ will not generate during the photocatalytic process. Because the reduction potential of O_2^- and HO_2· are higher than that of Ag_3PO_4 conduction band. Otherwise, the valence band potential of Ag_3PO_4 is about +2.9 eV, which is powerful enough to oxidize H_2O forming ·OH (+2.68 eV) [210]. Moreover, the released electrons can be adsorbed by dissolved O_2 to form H_2O_2. The H_2O_2 can further get electron from the conduction band of Ag3PO4 to generate ·OH [210,211]. Therefore, ·OH could be the most important active specie which responsible for the fast degradation of RhB dye. The generation process of ·OH can be explained by the equation as follows:

$$O_2 + 2H^+ + 2e^- \rightarrow H_2O_2 \quad (34)$$

$$H_2O_2 + e^- \rightarrow \cdot OH + OH^- \quad (35)$$

According to Eq.s 34 and 35, the addition of HNO_3 will increase the amount of ·OH, which favors for degradation rate of RhB. This could be the main reason that Ag_3PO_4 has faster degradation rate of RhB under acidic condition compared with that under neutral and alkaline conditions.

Otherwise, as shown in **Fig 5.14b**, the absorption spectra of MO is the same at pH value of 7 and 12, of which the peak of the spectral curve is at 464 nm. Interestingly, as the pH value adjust to 1, the peak of the spectral curve of MO shifts to 510 nm. The shift of the peak position indicates that the chemical structure of MO has changed with the addition of acid. It was reported [212] that under acidic condition, the N=N of MO will change into N–N and the benzene ring will also transform into chinone. The N–N is less stable than N=N while the structure of chinone is less stable than that of benzene ring. Hence MO molecule is less stable so that easy to with decomposition under acidic condition than neutral and alkaline conditions. Moreover, acidic condition favors for the generation of ·OH by Ag_3PO_4, which has strong oxidative power. Thus, acidic condition favors for the degradation of MO by Ag_3PO_4, whether from the viewpoint of the catalyst or the dye itself.

To further confirm that acidic condition favors for the generation of ·OH, dimethyl sulfoxide (DMSO) was added into the degradation process as ·OH scavenger. It can be observed in **Fig 5.15a** that 60 percent of RhB has been removed by Ag_3PO_4 in 15 min under neutral condition without adding DMSO. By adding 5 mL DMSO, only 45 percent of RhB is removed in the same duration, indicating the degradation efficiency of RhB is reduced due to the decrease of ·OH. When the amount of DMSO

increased to 10 mL, the degradation curve of RhB is almost the same as that of 5 mL. This result indicates that 5 mL DMSO is an excessive amount for the capture of the ·OH generated during the reaction. Under acidic condition (**Fig 5.15b**), 67 percent of RhB is degraded in 15 min without the addition of DMSO. 50 percent of RhB is removed by Ag_3PO_4 with the addition of 5 mL DMSO. The decreasing of RhB concentration also reveals the reduction of ·OH amount, which is captured by DMSO. However, the concentration of RhB continues to decrease with the addition of another 5 mL DMSO. This could be explained by that the first 5 mL DMSO can not capture the entire ·OH existing in the system under acidic condition. Hence, more DMSO is necessary for the capture of resident ·OH to avoid the oxidation caused by ·OH. This result confirms that the amount of ·OH generated under acidic condition is larger than that under neutral condition. It also agrees with the assumption of that increasing of H^+ promotes the generation of ·OH in the system (Eq.s 34 and 35). The results confirm that acidic condition favors for the generation of ·OH, as well as the degradation of RhB. In summary, the high degradation efficiency of RhB and MO by Ag_3PO_4 under acidic condition is attributed to the large amounts of ·OH.

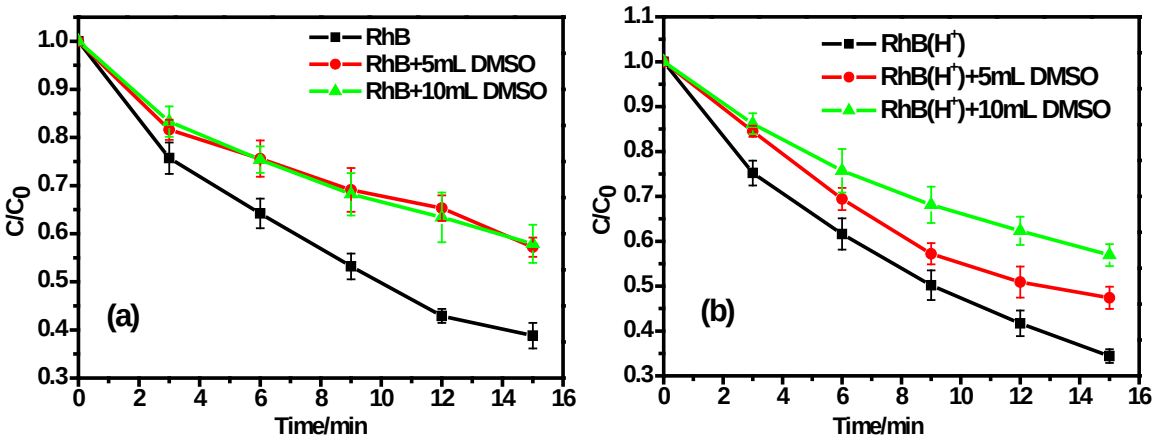

Fig 5.15 Degradation curves of RhB with different amounts of DMSO: (a) pH=7; (b) pH=1

5.3.3 Effect of pH values on mixture dye degradation

In the previous study, we have demonstrated that selective adsorption occurs when degrading more than one kind of organic dye. To study the effect of pH values on mixture dye degradation, RhB-MO mixture solution was degraded by the SPMs at different pH values. **Fig 5.16a, b** show the degradation and reaction kinetic curves of the mixture dye by the SPMs under acidic condition (pH=1). The results indicate the degradation rate of RhB is faster than that of MO under acidic condition. The apparent reaction rate constants of RhB and MO are 0.16327 and 0.06828 min^{-1}, respectively.

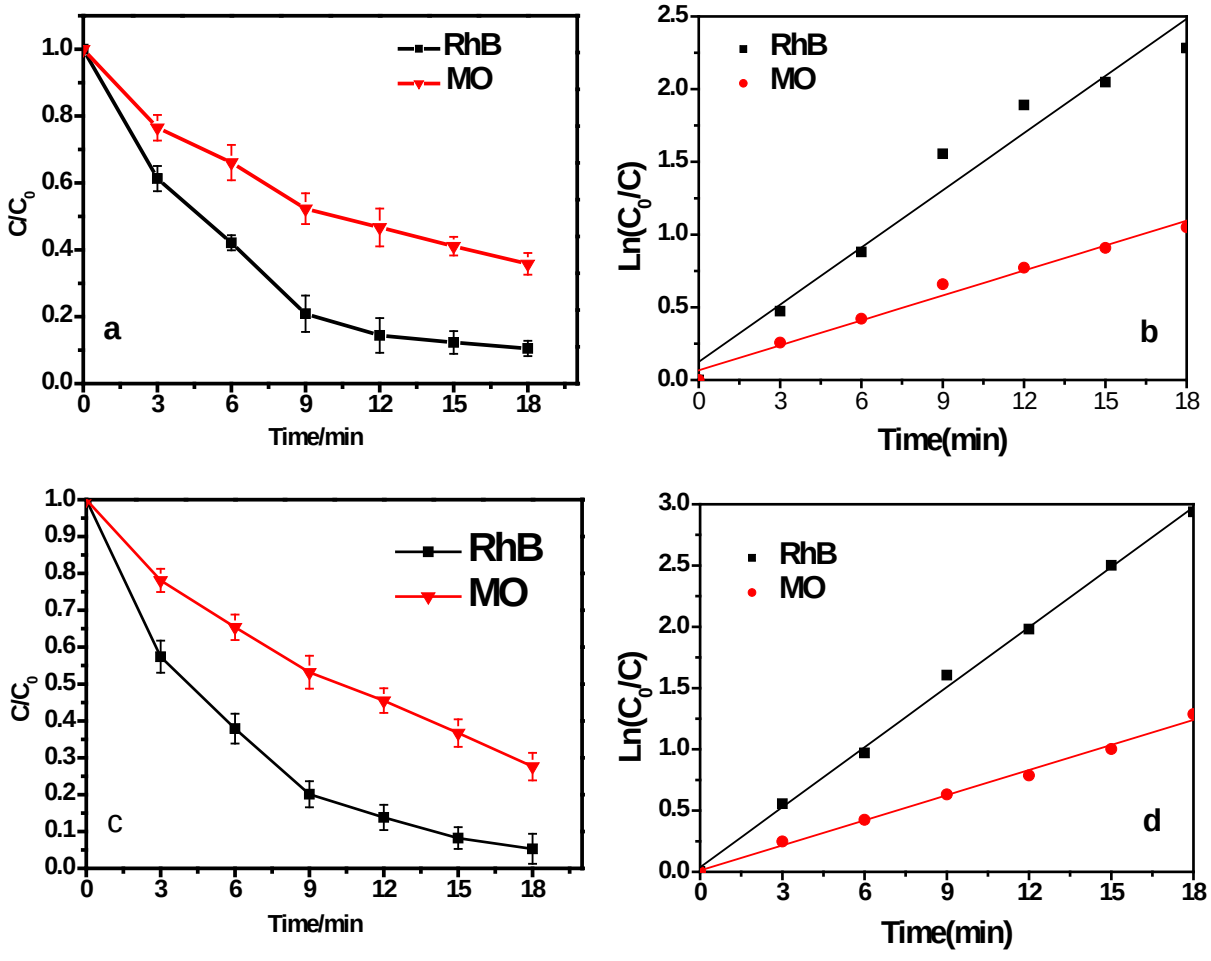

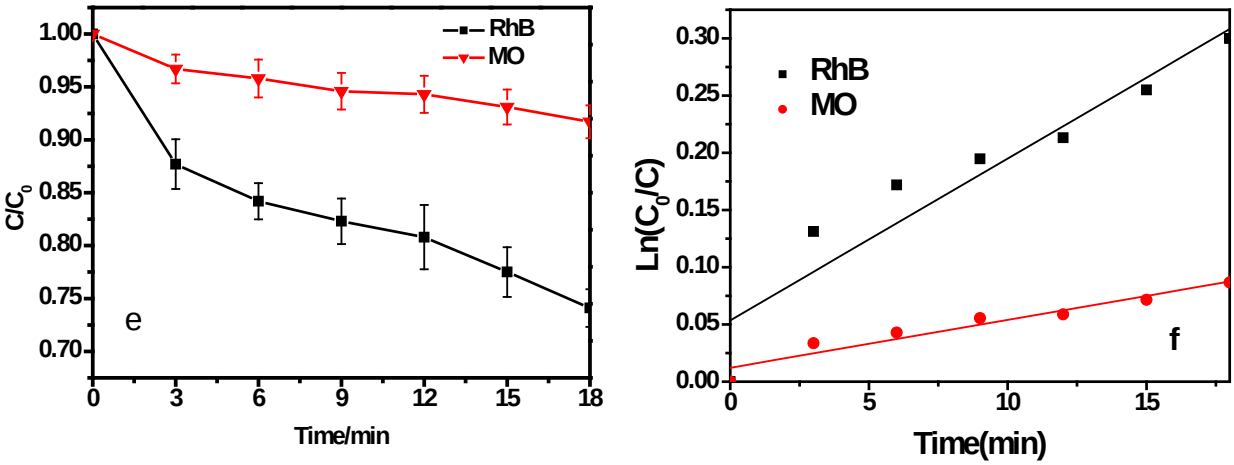

Fig 5.16 Degradation and apparent kinetic curves of RhB-MO mixture solution over Ag_3PO_4: (a, b) pH= 1, (c,d) pH=7, (e, f) pH= 12.

The degradation rate of RhB is calculated to be 2.39 times that of MO at pH 1. For the degradation of RhB-MO mixture at pH 7 and 12, RhB degradations are also faster than that of MO. The apparent reaction rate constants RhB and MO are 0.13151 and 0.05561 min^{-1} under neutral condition (pH=7); 0.03383 and 0.00419 min^{-1} under alkaline condition, respectively. The degradation rate of RhB is calculated to be 2.36 times that of MO under neutral condition, while the degradation rate of RhB is calculated to be 8 times that of MO. Moreover, the degradation rate of RhB at pH 1 is 1.24 and 4.82 times of that at pH 7 and 12, respectively. And the degradation rate of MO at pH 1 is 1.22 and 16.29 times of that at pH 7 and 12, respectively. The results are in agreement with the degradation of individual dyes by SPMs, in which SPMs have higher photocatalytic activity than MO under whether under acidic, neutral or alkaline conditions. And acidic condition favors for the high efficient degradation of organic dyes by the SPMs.

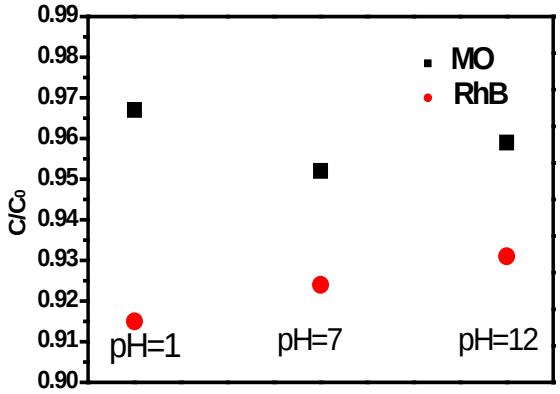

Fig 5.17 Adsorption of RhB-MO mixture solution by SPMs in 30 min.

Furthermore, the RhB-MO mixture solution was kept stirring for 30 minutes without light irradiation to investigate the adsorption abilities of RhB and MO by the SPMs. It can be observed from **Fig 5.17** that after 30 min stirring in dark, 8.5, 7.6, 6.9 percent of RhB molecules and 3.3, 4.8, 4.1 percent of MO molecules are removed from the solution by physical adsorption of the SPMs. The results indicate the adsorption of RhB by the SPMs is better than that of MO, whether under acidic, neutral or alkaline condition. Thus, the degradation of RhB is faster that of MO by the SPMs due to the better adsorption of RhB during the reaction. The results confirm that the selective adsorption plays an important role in the photocatalytic activity of the SPMs for the degradation of mixture dye.

5.3.4 Stabilities under different pH

As it is known, the stability of a catalyst is in great relevence with the reaction conditions. Hence, the staibility of the SPMs has been studied by degrading RhB dye solution under acidic, neutral and alkaline conditions, respectively. **Fig 5. 18a** shows the cycle experiment of RhB degradation by SPMs at pH=1. An obvious activity reduction of SPMs has been observed after 5 cycles under acidic condition (pH=1). The concentration of RhB has decreased by 82.2% after 10 min in the degradation of

first run. And the degradation efficiencies of RhB by SPMs after 10 min in the rest cycles are 78.7, 77.5, 74.3 and 67.6 percent, respectively. The degradation efficiency of RhB by SPMs has decreased 14.6% between the first run and the last run, indicating the activity of SPMs has been reduced after multiple degradation of RhB. Otherwise, the degradation efficiencies of RhB under neutral condition (pH=7) in the same time are 67.5, 66.4, 64.3, 63.2 and 60.9 percent, respectively. The reduction of RhB degradation efficiency by SPMs is only 6.6% between the first and last run. The results indicate that the reduction of activity under neutral condition is slower than that under acidic condition, namely, the stability of SPMs is better under neutral aqueous system. This is mainly ascribed to that Ag_3PO_4 is slightly soluble in aqueous system and the dissolved Ag ion can be reduced into metallic Ag by the photo-induced electron in the conduction band. The reaction formular is as follows:

$$Ag_3PO_4 \rightarrow 3Ag+ + PO_4^{3-} \quad (36)$$

$$Ag+ + e^- \rightarrow Ag \quad (37)$$

Under acidic condition, the reduction of Ag ion is faster than that under neutral condition. Because the high concentration of H^+ under acidic condition can rapidly combine with the dissolved PO_4^{3-} to form H_3PO_4. The existing of H_3PO_4 increases the solubility of Ag_3PO_4, thus promoting the dissolution process of Ag_3PO_4 as well as the releasing of Ag ion. Since the amount of free Ag ions increased, the generation of metallic Ag will be quick as well. The metallic Ag does not have photocatalytic itself. Hence the reduction of Ag ion into metallic Ag will lead to the weight loss of Ag_3PO_4 catalyst, thereby reducing the degradation efficiency of RhB solution. **Fig 5.18c** shows the circulation degradation under alkaline condition. The degradation efficiencies of RhB in 10 min by SPMs are 38.6, 36.9, 33, 31.8 and 27.9 percent, respectively. The degradation efficiency of RhB has reduced 10.7% between the first

and last test. The activity reduction of SPMs can also be attributed to the reaction between the dissolved Ag+ and OH-. The reaction formular is shown as follows:

$$2Ag+ + 2OH^- \rightarrow Ag_2O + H_2O \quad (38)$$

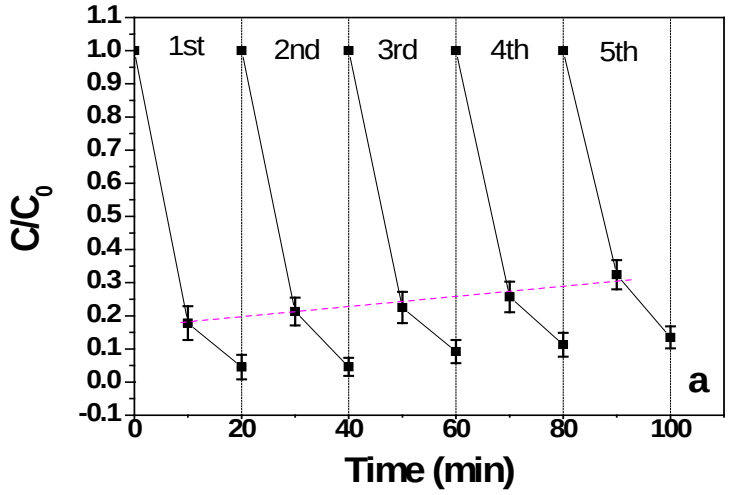

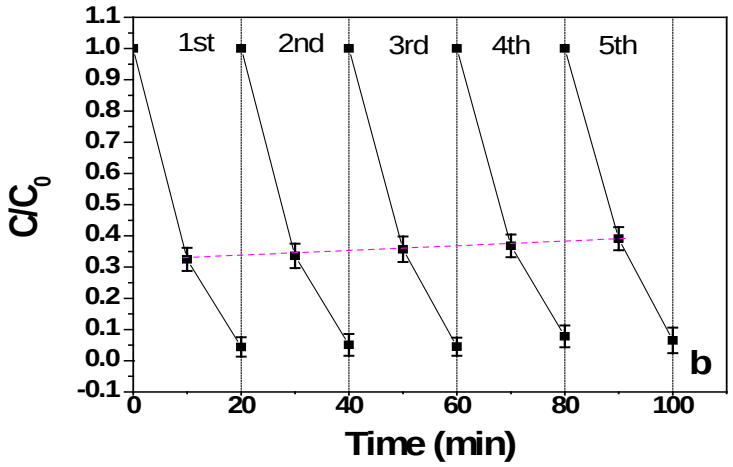

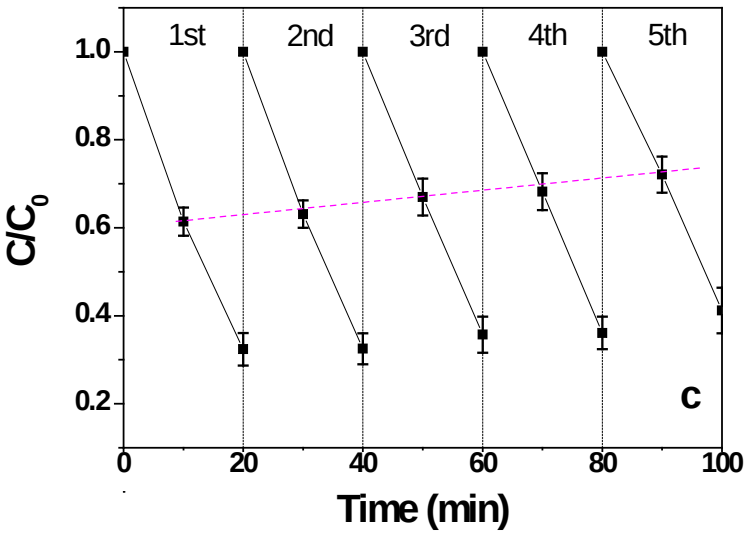

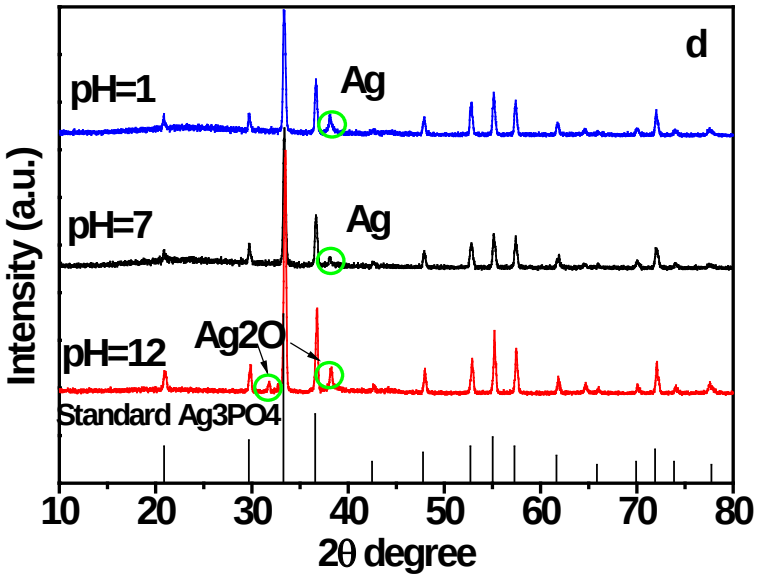

Fig 5.18 Degradation curves of RhB by the SPMs for 5 cycles under different pH values (a) pH=1, (b) pH=7, (c) pH=12 and XRD patterns of the recovered SPMs (d).

The generation of Ag_2O also decreases the substance weight of Ag_3PO_4, leading to a reduction of degradation efficiency. Anyway, Ag_2O is also a visible light responding photocatalyst (band gap 1.46 eV). The reduction of activity caused by the weight loss of Ag_3PO_4 could be made up by the generation of Ag_2O on Ag_3PO_4 surface. Therefore, the degradation efficiency reduction of RhB under alkaline condition (10.7%) is not that much as under acidic condition (14.6). To comfirm the generation of metallic Ag and Ag_2O, XRD patterns are performed under acidic, neutral and alkaline conditions in **Fig 5.18d**. It is obviously that impurity peaks other than Ag_3PO_4 have formed after the cycle experiments. The highest impurity peak emerges at approximately 38.1 º 2θ degree, which is near both the {111} facet of metallic Ag (JCPDS no 04-0783) and the {111} facet of Ag_2O (JCPDS no 65-3289). Importantly, in the XRD pattern of SPMs recovered from alkaline condition (pH=12,

in red) an impurity peak emergies at approximately 32.0 º 2θ degree, which is rightly in accordance with the {200} facet of Ag_2O. Anyway, this peak does not emergy under either acidic or neutral condition. This result indicates that the existing of Ag_2O in the SPMs recovered from the alkaline solution, confirming the assumption of the generation of Ag_2O under alkaline condition.

To conclude, the photocatalytic activity of SPMs is reduced under neutral condition ascribed to that the slightly dissolved Ag ions are reduced into metallic Ag by photo-induced electrons. The reduction of activity is even more serious under acidic condition due to the serious dissolution of Ag_3PO_4 by phosphoric acid. Otherwise, under alkaline condition, the generation of Ag_2O due to the reaction of Ag ion and hydroxyl also has a negative effect on the photocatalytic activity. To optimize the highest photocatalytic activity and stability, SPMs are most suitable to be applied under neutral condition.

5.4 Summary of Chapter 5

Silver phosphate photocatalyst with unique hollow structure has been synthesized via a simple chemical hydrothermal method. PEG 200 as the reaction medium plays a vital role in the formation of SPMs. SPMs exhibit excellent photocatalytic activity for the degradation of organic dyes under visible light irradiation due to the small dimension, large surface area and specific hollow structure. Under different pH values, RhB and MO organic dyes are degraded by the SPMs under visible light irradiation. The results indicate Ag_3PO_4 have the highest degradation efficiency of RhB and MO dyes under acidic condition when compared with that under neutral and alkaline conditions. This is attributed to that the acidic

condition favors for the generation of ·OH, which plays a vital role in the photocatalytic oxidation process. Moreover, the SPMs is found with good adsorption and degradation efficiency for RhB due to the selective adsorption of dyes, resulting in faster degradation of RhB than MO. The studies of stability under different pH value reveal that SPMs exhibit the optimal photocatalytic acitivity and stability under neutral reaction condition.

Chapter 6 Wastewater cleaning by silver phosphate under natural indoor weak light

As a high-quantum-efficiency photocatalyst, the serious photo-corrosion of silver phosphate (Ag_3PO_4), limits the practical applications in water purification and challenges us. Herein, Ag_3PO_4 is found to have a high stability under natural indoor weak light irradiation, suggesting that we can employ it by adopting a new application strategy. In our studies, rhodamine B (RhB, cationic dye), methyl orange (MO, anionic dye) and RhB-MO mixture aqueous solutions are used as the probing reaction for the degradation of organic wastewater. It is found that RhB, MO and RhB-MO can be completely degraded after 28 hours under natural indoor weak light irradiation, indicating that multi-component organic contaminants can be efficiently degraded by Ag_3PO_4 under natural indoor weak light irradiation. The density of natural indoor weak light is measured to be 72 cd, which is merely one-thousandth of 300 W xenon lamp (68.2×10^3 cd). Most importantly, Ag_3PO_4 shows a high stability under natural indoor weak light irradiation, demonstrated by the formation of fairly rare Ag. Furthermore, we also investigate the influence of inorganic ions on organic dyes degradation. It shows that the Cl^- and Cr^{6+} ions with high concentrations can significantly decreased the degradation rate of organic dyes.

6.1 Degradation of individual dye solution

The photocatalytic activities of silver phosphate are evaluated by degrading

organic dyes under visible light and natural indoor weak light, respectively. A 300W xenon lamp is used to provide visible light (above 420 nm). The individual dyes are further degraded by silver phosphate under indoor weak light to evaluate the photocatalytic performance of silver phosphate under natural solar energy irradiation. The test conditions are presented in the experimental section, Chapter 4.

6.1.1 Under artificial visible light irradiation

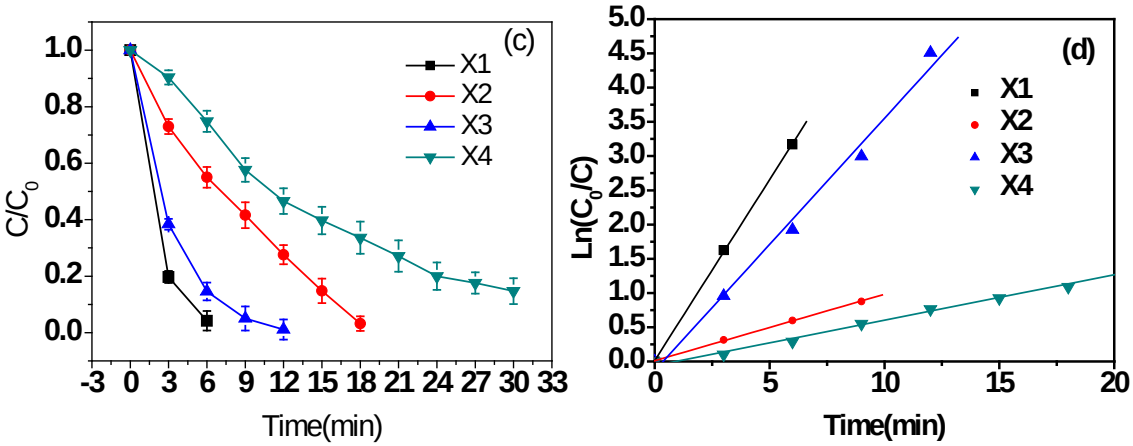

Fig 6.1 Degradation curves and reaction kinetic curves of individual dye over Ag_3PO_4 dendrites (X1), microtubes (X2), tetrapods (X3) and dodecahedrons (X4) under visible light irradiation (≧420 nm): (a,b) Rhodamine B (RhB); (c,d) Methyl orange (MO)

Fig 6.1a shows the degradation curves of individual cationic RhB over samples X1, X2, X3, X4 under visible light irradiation (≥420 nm). The results illustrate individual RhB aqueous solution can be degraded to a very low concentration level by X1, X2, X3 and X4 within 9, 9, 18 and 33 minutes, respectively. The X1 show the highest activity for the RhB degradation, followed by the X2, X3 and X4. The reaction kinetic curves for the samples are presented in **Fig 6.1b**. The apparent reaction kinetic constants are calculated to be as follows: k_1=0.46941, k_2=0.33051, k_3=0.14167, k_4=0.06801 (min^{-1}). The degradation rate by X1 is 1.42, 3.31 and 6.9 times that of X2, X3 and X4, respectively. This could be attributed to the highly

exposed active {110} facets (99%) of X1 [117]. It is reported [191] that the {110} facets (1.31 J m^{-2}) of Ag_3PO_4 have a higher photocatalytic activity than the {100}(1.12 J m^{-2}) and {111}(1.03 J m^{-2}) facets for dye degradation. Although X2 is with polycrystalline facets and lower exposure percentage of {110} facets than X1 (99%), its photocatalytic activity is as high as that of X1. This is ascribed to that X2 consists of numerous nanoparticles and has a surface area of 7.2 m^2 g^{-1}. The unique structure enables multiple scatterings and absorption of incident light, namely, the light energy could be absorbed time and again by X2. As a result, X2 have a high utilization efficiency of energy, leading to a high photocatalytic activity. To conclude, X1 and X2 have greatly high photocatalytic activities for the degradation of individual RhB solution.

Fig 6.1c shows the degradation curves of anionic MO by Ag_3PO_4 samples. The individual MO solution is completely degraded in 6, 18, 12 and 30 minutes by X1, X2, X3 and X4, respectively. The reaction kinetic curves are presented in **Fig 6.1d**. The apparent reaction kinetic constants of the samples are calculated to be: k_1=0.52835, k_2= 0.16913, k_3= 0.36861, k_4=0.06644 min^{-1}. The degrading rate of X1 is 1.43, 3.12 and 7.95 times as high as that of X3, X2 and X4. Except for X2, the degradation rates of MO over the other samples are faster than that of RhB. This could be explained by selective adsorption of RhB and MO. It is well known that MO is an anionic dye and RhB is a cationic dye [213]. The MO molecule is with negative charge in aqueous solution due to the dissolved Na^+, while RhB molecule is with positive charge due to the dissolved Cl^-. The anionic ions would be preferentially attracted by silver phosphate due to its positively charged surface [97]. The strong attraction between Ag_3PO_4 and the anionic molecules results in good adsorption of MO molecules, thus enhancing the degrading efficiency of MO. Therefore the degradation rates of MO by

X1, X3 and X4 are faster than that of RhB. Nevertheless, X2 were prepared using PEG200 as solvent, of which the ether bond (–O–) is generally with weak negative charge. The PEG200 molecules are difficult to be completely removed from the catalyst surface by washing. Hence X2 surface would be with negative charge due to the residual PEG200. The negatively charged surfaces of X2 have stronger attraction to RhB than MO molecules, leading to good adsorption and degradation of RhB. Zeta potential measurements [214] have been done to prove the surface charge of the samples, as shown in **Table 6.1**. The method for the measurement is briefly introduced here. Firstly, 0.1 mg Ag_3PO_4 was uniformly dispersed in 200 ml RhB/MO mixture solution (pH= 6) to obtain the sample solution. The samples were tested by Zetasizer (Nano ZS90). Every sample was tested for 3 cycles, every cycles for 50 runs to obtain the average Zeta potential. The results indicate the surfaces of X1 and X4 are with positive charge, which are in accordance with our assumption. However, the surface charge of X2 and X3 can not be ascertained clearly, because they have too large sizes (larger than 10 μm). The suitable particle sizes are smaller than 1 μm for the instrument. Therefore, it is difficult to confirm that the higher activity for the degradation of RhB than for MO over X2 is due to negative surface charge. Summarily, Ag_3PO_4 exhibit excellent degradation activities of individual organic dye (RhB, MO) under visible light irradiation. The degradation rates of RhB and MO are strongly dependent on the surface charge of the catalysts. Ag_3PO_4 with positively charged surface favors for the adsorption and degradation of MO, while Ag_3PO_4 with negatively charged surface favors for the adsorption and degradation of RhB.

Table 6.1 Zeta potential measurements of the samples at pH 6 (which is the pH value of solution used in degradation process)

Zeta Potential (mV)	Dendrites	Microtubes	Tetrapods	Dodecahedrons
Cycle1 (average)	+5.1	+0.4	+0.8	+2.8
Cycle2 (average)	+5.7	-2.8	-1.5	+7.3
Cycle3 (average)	+8.3	-0.7	-1.8	+3.1

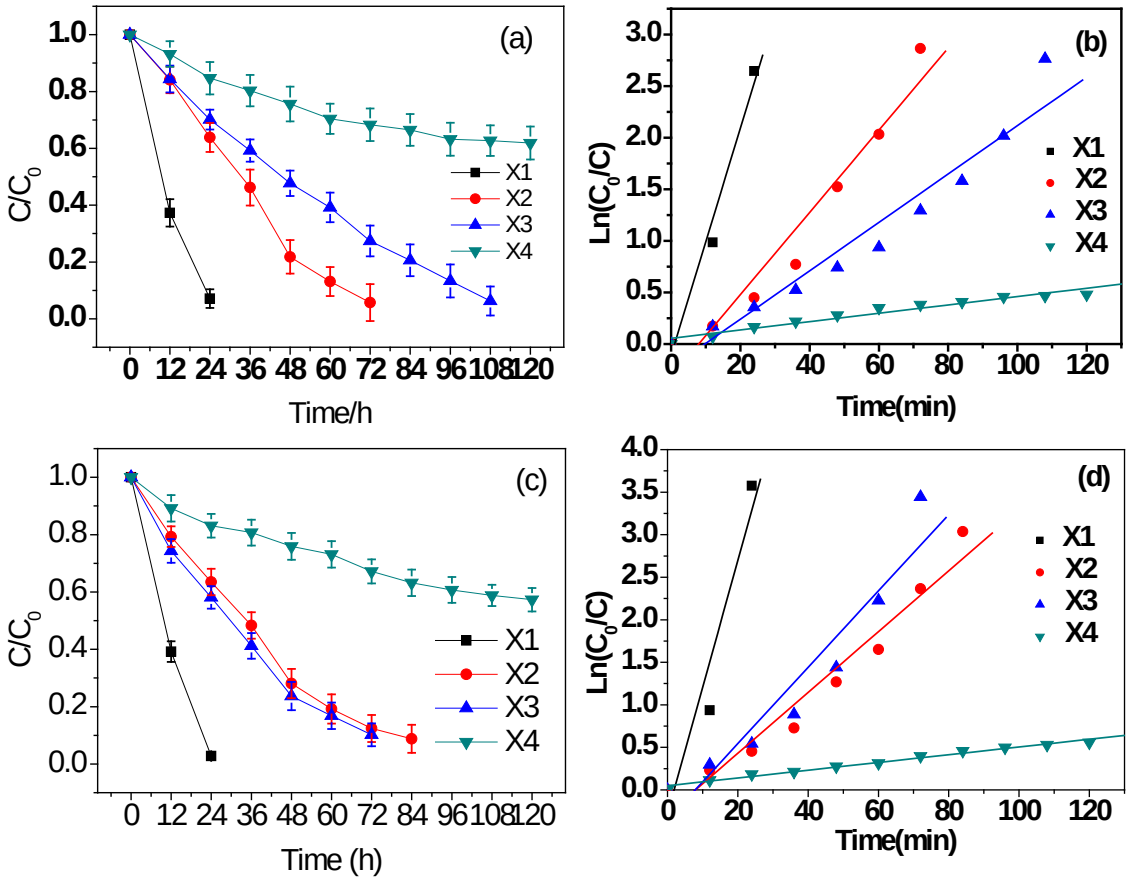

Fig 6.2 Degradation curves and reaction kinetic curves of individual dye over Ag_3PO_4 dendrites (X1), microtubes (X2), tetrapods (X3) and dodecahedrons (X4) under indoor weak daylight: (a,b) RhB; (c,d) MO

6.1.2 Under natural indoor weak light

We have further removed artificial light source to investigate the degradation performances of dye pollutants under natural indoor weak light. The results reveal that individual dye can also be decolorized by Ag_3PO_4 under natural indoor weak light, of which light density is fairly low (about 72 cd). It provides an extension application of solar energy driven photocatalysts for environmental remediation and energy conversion. In our experiments, individual RhB solution and individual MO solution were placed in a laboratory room (in Nanjing, in China) and kept stirring. By this way, the organic dyes were degraded by Ag_3PO_4 spontaneously under natural indoor weak light.

Fig 6.2 shows the degradation curves and reaction kinetic curves of individual RhB and MO solutions over Ag_3PO_4 samples under natural indoor weak light. It can be observed from **Fig 6.2a** that under natural indoor weak light, 24, 72 and 108 hours are needed for X1, X2 and X3 to completely degrade RhB dye, while 24, 72 and 84 hours are needed for MO degradation (**Fig 6.2c**), respectively. The degrading rates of the dyes by X4 are slow (38% RhB and 43% MO have been removed separately after 120 min), which can be mainly ascribed to its relatively low activity than the other samples. The reaction kinetic curves of RhB and MO by Ag_3PO_4 samples are shown in **Fig 6.2b, d**. The apparent kinetic constants for the degradation of RhB are as follows: k_1=0.08099, k_2=0.03984, k_3=0.02346, k_4=0.00405 (min^{-1}). The apparent kinetic constants for MO degradation are k_1=0.14898, k_2=0.03576, k_3=0.04488, k_4=0.00455 (min^{-1}). The degradation rate of RhB by X1 is 2, 3.5 and 20 times that of X2, X3 and X4; the degradation rate of MO by X1 is 3.3, 4 and 33 times that of X3, X2 and X4, respectively. Their activity order under natural indoor weak light is in

accord with that under simulated visible light irradiation.

To conclude, under 300W Xe lamp (light density 68.2×10^3cd), 6 and 9 minutes are needed for the completely degradation of individual MO and RhB dye over X1, respectively; 24 and 36 hours are needed under natural indoor weak light (light density 72 cd). The degradation time under natural indoor weak light is 240 times that of under Xe lamp degradation. It should be noticed that the light density of natural indoor weak light is approximately one-thousandth that of visible light generated by Xe lamp. From the viewpoint of energy conservation, the degradation of organic dye solution by weak light is more energy-efficient than by artificial light energy. Except for magnetic stirrer, no extra electrical energy is consumed for the natural indoor weak light-driven degradation by Ag_3PO_4, while 300W Xe lamp is supported by a 15 A current density. Thus large amounts of electrical power (mainly produced from fossil resources) could be saved and natural solar energy can be effectively utilized. From the viewpoint of environmental remediation, the organic dye degradation by silver phosphate under natural indoor weak light provides an efficient method for wastewater purification. This weak light-driven wastewater cleaning method is expected to be extended to the natural indoor air purification. For example, silver-based materials could be applied for air cleaning under dim light conditions, especially for car park, cellar, warehouse, spacecraft, armored car, and so on.

6.2 Degradation of mixed dye solution

The industrial wastewaters always contain multiple kinds of pollutants, which is dependent on the production process. These toxic compounds often interact with one another, making the treatments more complicate. As a result, it becomes difficult to decompose more than one kind of hazardous compound. It is a big challenge to

develop an effective way to deal with the actual wastewaters. To evaluate the degradation performance of Ag_3PO_4 photocatalyst for multi-component wastewater, the RhB-MO mixture solution is degraded by Ag_3PO_4 samples under both Xe lamp irradiation and natural indoor weak light irradiation.

6.2.1 Under visible light irradiation by an artificial Xe lamp

Fig 6.3 shows the UV-vis absorption spectra of RhB-MO mixture dye solution at different degradation times over Ag_3PO_4 samples under visible light (>420 nm, 68.2 $\times 10^3$cd, 300 W xexon lamp). The characteristic absorption peaks of RhB and MO are at 554 nm and 463 nm, respectively. It can be observed from **Fig 6.3a** that both peaks of RhB and MO are strong at the beginning of the reaction. As the reaction progresses, the typical peaks of RhB and MO decrease steadily. The RhB-MO mixture solution has been completely degraded by X1, X2, X3 and X4 in 15, 24, 24 and 45 minutes, respectively. Under visible light irradiation, X1 show the highest photocatalytic activity among all the samples, while the degradation efficiencies of X2 and X3 are almost the same (24 min). X4 show the lowest photocatalytic activity among all the samples (45 min). The results have demonstrated the Ag_3PO_4 samples have excellent activity for the degradation of multi-component organic dye solution due to its strong oxidizing power under visible light irradiation. As discussed above, the degradation rate of RhB and MO is different due to the different surface properties of the samples. The surfaces of X1, X2 and X4 are with positive charge, which favors for the adsorption of anionic dyes. It can be seen from **Fig 6.3a** that the absorbance intensity of MO at 463 nm has decreased to 5% in 9 min. However, the concentration level of RhB is approximately 23% at the same time. Same results are observed in the degradation of mixed dye by X2, X3 and X4. The concentration of MO degraded by

X2 is about 10% in 15 min, while that of RhB is as high as 42% at the same time. The results indicate that the adsorption of MO is prior to that of RhB due to the positive surface of Ag_3PO_4.

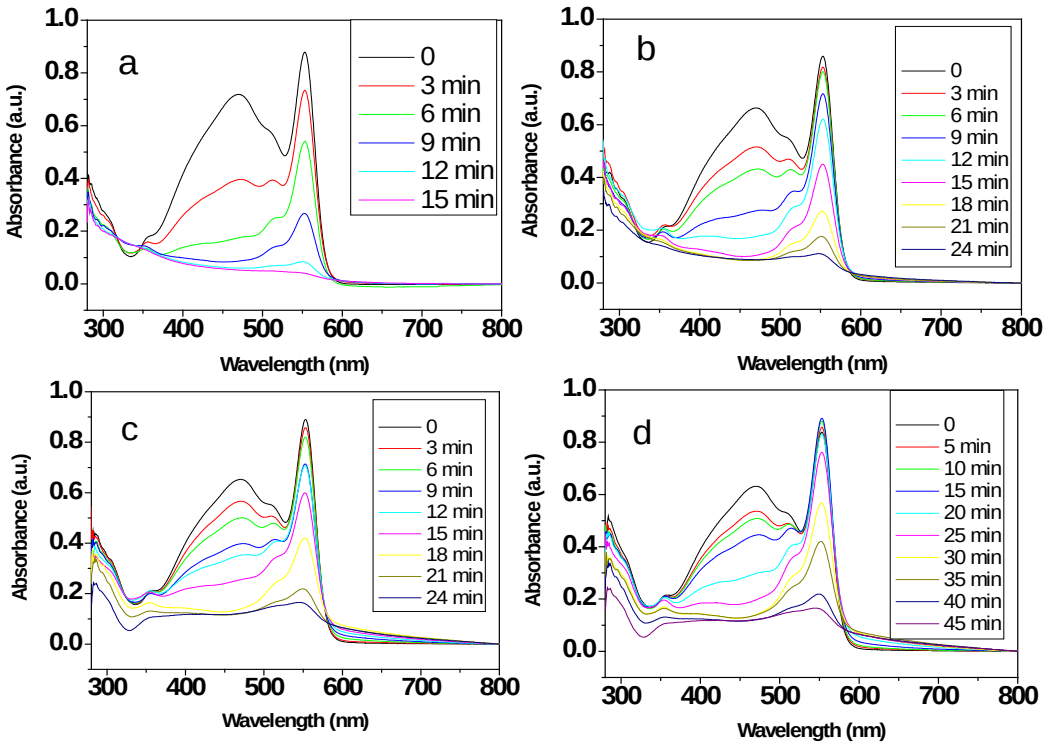

Fig 6.3 UV-vis absorption spectra of RhB/MO mixture dyes at different irradiation times over Ag_3PO_4 samples under visible light irradiation (≧420 nm): (a) Dendrites; (b) Tetrapods; (c) Microtubes; (d) Dodecahedrons

6.2.2 Under natural indoor weak light

Fig 6.4 shows the UV-Vis absorption spectra of RhB-MO mixture dye solution at different degradation times over Ag_3PO_4 samples under natural indoor weak light. From **Fig 6.4** we can find that the mixed dye solution has been degraded by X1, X2 and X3 within 28, 168 and 264 hours, respectively. The degradation process of the dye mixture by Ag_3PO_4 samples under weak light has been studied. In the case of X1, at the beginning of the reaction, both peaks of RhB and MO are strong. The absorbance intensity of MO significantly decreases in the first 4 hours and 94% of

MO has been removed at 12 h. In comparison, 46.5% of RhB has been merely removed at 12 h, then it takes another 16 h to finish the reaction (92.6% removed). It is obvious that the degradation rate of MO is faster than that of RhB in the mixture system. As it is known, the main chromogenic group of MO is –N=N–, while that of RhB is the conjugated xanthene ring [201]. The bond energy of conjugated xanthene ring (882kJ/mol) is greatly higher than that (418 kJ/mol) of –N=N–, thereby RhB is more difficult to be decolorized than MO. Moreover, the adsorption of MO on Ag_3PO_4 is better than that of RhB due to the selective adsorption caused by the opposite charges of MO and Ag_3PO_4 (see section 2.3.2.2). The preferential adsorption of MO, as the first prerequisite step, favors for the selective degradation of MO. As a result, the degradation rate of MO is faster than RhB.

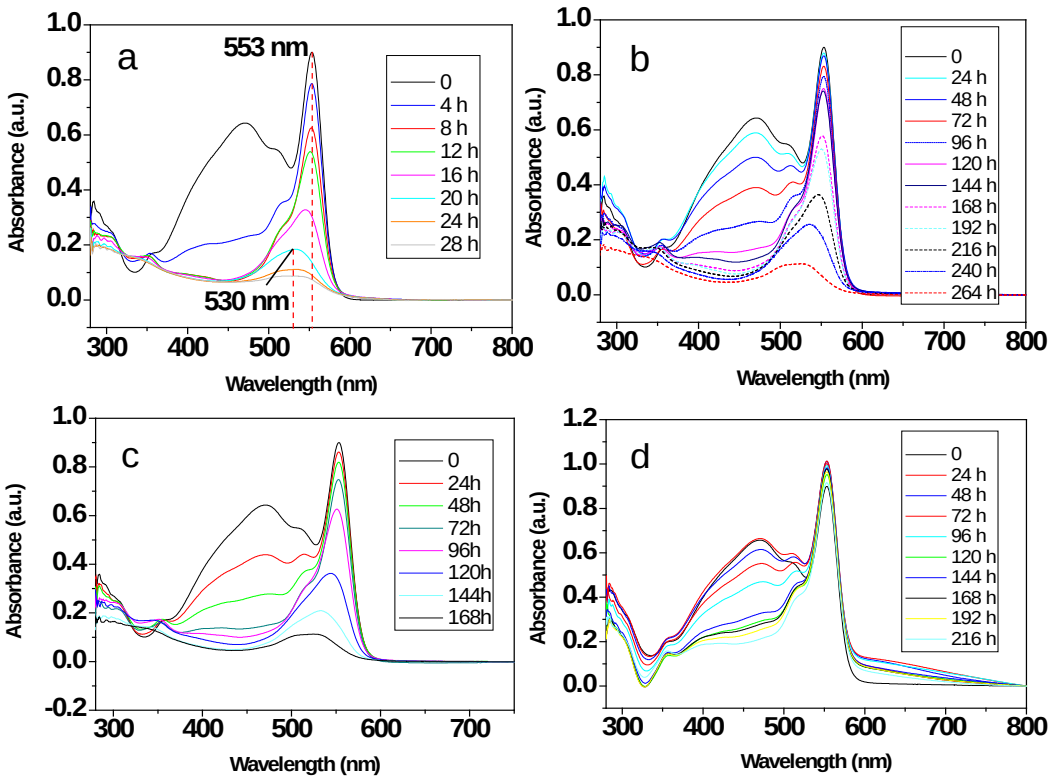

Fig 6.4 UV-vis absorption spectra of RhB/MO mixture dyes over Ag_3PO_4 samples under natural indoor weak daylight: (a) Dendrites; (b) Tetrapods; (c) Microtubes; (d) Dodecahedrons

Besides, an obvious hypsochromic shift (553 to 530 nm) of RhB peak can be observed from **Fig 6.4a**, which can be ascribed to the de-ethylation of RhB molecules [215]. However, no obvious peak shift of RhB can be observed in the visible light irradiation (Xe lamp). We assume that there could be two photochemical mechanisms, namely, a photocatalytic process and a photosensitized process. On one hand, under visible light irradiation, RhB could be degraded by the direct interaction with the strong oxidizing hole. In this case, deethylation intermediates would not emerged or be further degraded fleetly due to the powerful oxidizing function of hole. On the other hand, under natural indoor weak light, RhB dye could be excited by light of region above 420 nm, generating $O_2^{\bullet -}$ and $dye^{\bullet +}$ to mineralize RhB by a photosensitized process, namely, the self-degradation of RhB. To our knowledge, the photosensitized degradation of RhB is commonly via the deethylation process [216]. Consequently, both RhB and MO have been completely degraded by Ag_3PO_4 dendrites after 28 h. It is found that under natural indoor weak light irradiation, individual MO solution is easier to be degraded than individual RhB solution by X1. The same degradation characteristics can be observed for X2 and X3 (**Fig 6.4b, c**). It can be observed that RhB-MO mixture dyes are completely degraded after 168 and 264 h by X2 and X3, respectively. The activity of X2 is much higher than that of X3 under natural indoor weak light, which is attributed to its specific structure. As described in section 3.1, the light absorption ability of X2 can be strengthened by its hollow structure, thereby enhancing the degradation activity. **Fig 6.4d** shows the degradation curves of RhB-MO mixture dyes over X4. Under natural indoor weak light irradiation, 79.6% and 8.4% of MO and RhB are removed after 216 hours, respectively. The results indicate that under natural indoor weak light irradiation, the RhB is hardly degradable by X4, which is ascribed to the stable structure of RhB and

the relatively low activity of X4 compared with X1, X2 and X3. Overall, X1, X2 and X3 can effectively remove multi-component organic dyes in aqueous solution under natural indoor weak light irradiation; the selective adsorption of dye molecules significantly affects the degradation rates of different dyes; except for X2 with the negatively charged surface, the anionic dye is easier to be degraded by Ag_3PO_4 than cationic dye due to the selective adsorption of anionic molecules by positively charged surface of Ag_3PO_4. In summary, the organic dye mixture (RhB and MO) can be degraded by Ag_3PO_4 under both powerful visible light and natural indoor weak light. The light density of natural indoor weak light is only one-thousandth that of Xe lamp; nevertheless, the degradation time under natural indoor weak light is merely hundreds times of that under Xe lamp irradiation. Thus, it is an efficient, cost-saving method without using the expensive Xe lamp light source. Overall, the degradation by utilizing natural indoor weak light provides a new strategy for wastewater purification in the long term run. The strong oxidizing power of Ag_3PO_4 under weak light also implies its possible applications in other fields. For example, Ag_3PO_4 could be potentially applied in natural indoor air purifications to improve the natural indoor air quality. By utilizing Ag_3PO_4 based building materials, the hazardous volatile organic compounds (VOCs) such as formaldehyde could be effectively adsorbed and degraded under room light irradiation, thus reducing the healthy risks caused by harmful gases. Finally, the weak light driven degradation technology would be a suitable strategy to reduce the pressure of environmental protection and energy consumption.

6.3 Effects of inorganic salts

Generally, the real wastewater contains various inorganic salts. It has been demonstrated [217-220] that some of the inorganic salts will significantly affect the degrading performance of photocatalysts. To investigate the influences of inorganic

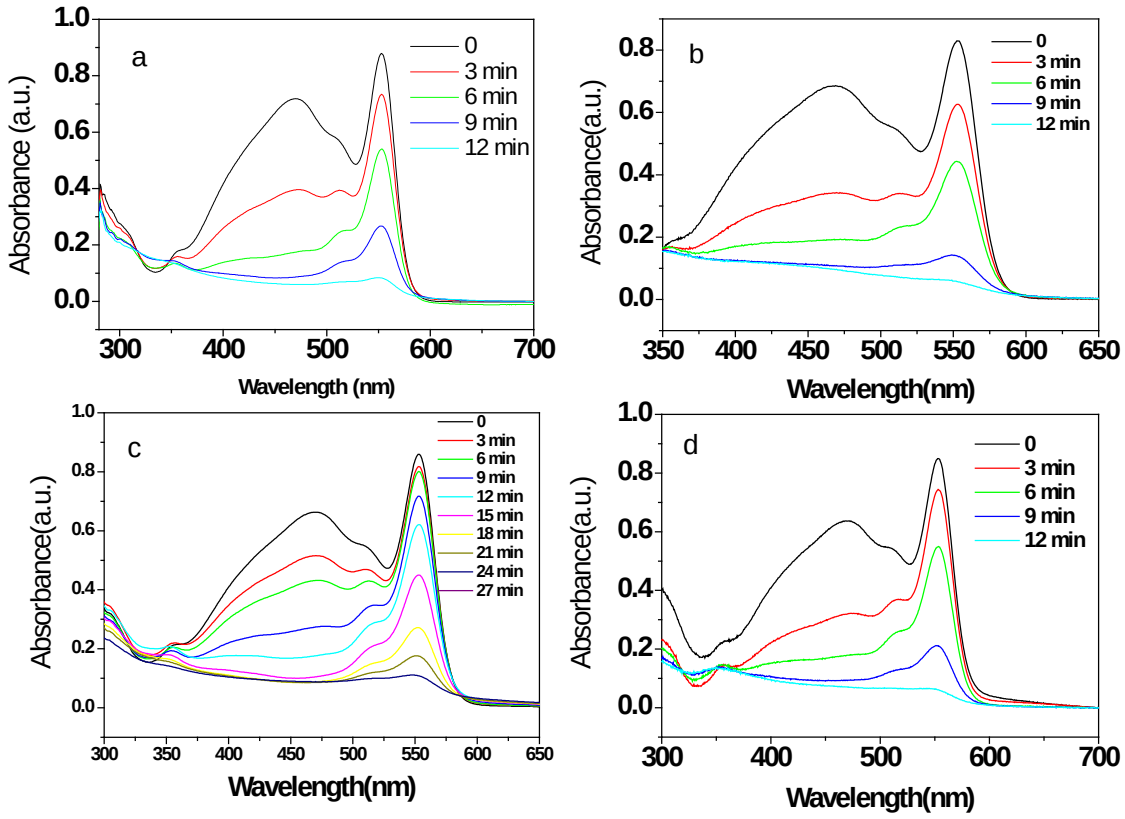

Fig 6.5 Absorption spectra of RhB/MO mixture dyes solutions containing different inorganic salts over Ag_3PO_4 dendrites under artificial visible light (Xe lamp) (≧420 nm): (a) KCl; (b) K_2SO_4; (c) $BaCl_2$; (d) $Ba(NO_3)_2$

Table 6.2 Inorganic ions concentrations in 200 mL RhB/MO mixture solutions containing KCl, K_2SO_4, NO_3^-, $BaCl_2$ and $K_2Cr_2O_7$

Chemicals	Doses (mmol)	K^+ (mmol/L)	Ba^{2+} (mmol/L)	Cl^- (mmol/L)	NO_3^- (mmol/L)	SO_4^{2-} (mmol/L)	Cr^{6+} (mmol/L)
KCl	1.3	6.5	/	6.5	/	/	/
K_2SO_4	1.3	13	/	/	/	6.5	/
$BaCl_2$	1.3	/	6.5	13	/	/	/
$Ba(NO_3)_2$	1.3	/	6.5	/	13	/	/
$K_2Cr_2O_7$	$6.8*10^{-3}$	/	/	/	/	/	$68*10^{-3}$

ions on the photocatalytic degradation of wastewater by Ag_3PO_4, the proper amounts of K^+, Ba^{2+}, Cl^-, SO_4^{2-}, NO_3^- and Cr^{6+} ions are added into RhB-MO mixture dye aqueous solution, respectively. The ion concentrations of K^+, Ba^{2+}, Cl^-, SO_4^{2-}, NO_3^- and Cr^{6+} can be found in **Table 6.2**. **Fig 6.5** shows absorption spectra of RhB-MO mixture dye solutions containing KCl, K_2SO_4, $BaCl_2$ and $Ba(NO_3)_2$ degraded by X1 under Xe lamp irradiation (≧420 nm). It is necessary to take about 12-15 min for X1 to degrade RhB-MO mixture solution without the addition of inorganic ions. From **Fig 6.5a and b** it can be seen that the mixed dyes are completely degraded by X1 in 12 min. No significant difference can be observed for the degradation curves of the solutions containing KCl and K_2SO_4, indicating that a proper amount of K^+, Cl^- and SO_4^{2-} do not affect the degradation of mixture dye. Nevertheless, the double reaction time is needed for the degradation of mixture dye solution with the addition of $BaCl_2$ (as shown in **Fig 6.5c**). The reduction of degradation rate could be ascribed to the existing of Ba^{2+}. Anyway, as shown in **Fig 6.5d**, the degradation of mixed dye solution containing $Ba(NO_3)_2$ only needs 12 min, indicating that the existing of Ba^{2+} does not affect the degradation rate of mixture dye. In Table 6.3, it can be found that

the concentration of Cl^- in $BaCl_2$ is two-fold that of KCl. Therefore, the reduction of degradation rate in Fig 6.7c can be attributed to the different concentration of Cl^-. The study by Wang et al. [220] indicated that the Cl^- ions can strongly adsorb on TiO_2 surface and reduce the photodegradation rate attributed to that the Cl^- ions compete with organic species for active sites and compete with oxygen for electron which reduces the formation of superoxide radicals. Similarly, in the degradation of mixture dye solution by Ag_3PO_4, high concentration of Cl^- ions are adsorbed on catalyst surface due to the positively charged Ag^+, thus competing with the dye molecules for active sites and reduce the photodegradation rate. It has been demonstrated by Piscopo [221] at low chloride concentrations (<0.02 M), the degradations of some organic compounds are strongly affected by the Cl^- concentration. Therefore, when the concentration of Cl^- is 6.5 mmol/L, Cl^- does not affect the degradation rate of the RhB-MO mixture. When the concentration of Cl^- increases to 13 mmol/L, the degradation rate slows down due to the adsorption of Cl^- on catalyst surface. Nevertheless, in the real water, the concentration of chloride can merely reach as high as 0.8 mol/L. Therefore, the high concentration of chloride in aqueous system would seriously decrease the degradation rate of wastewater.

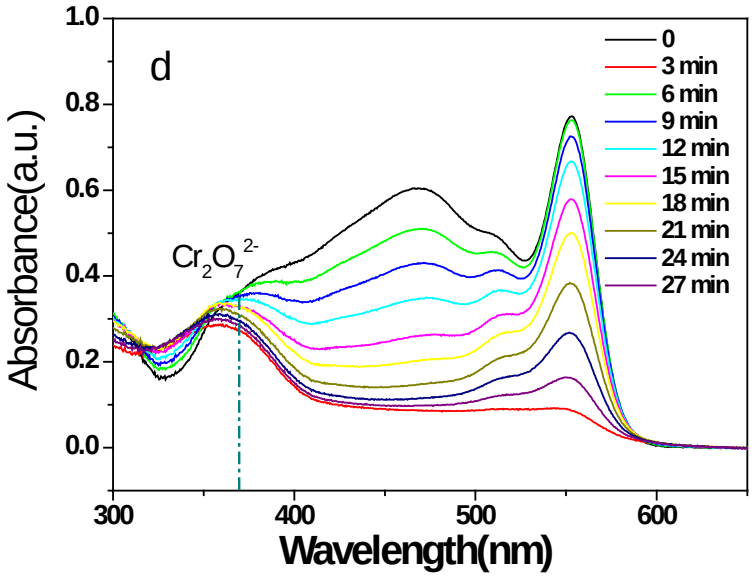

Fig 6.6 Degradation of mixture dye solution with the addition of $K_2Cr_2O_7$ by X1 under Xe lamp irradiation (≧420 nm)

Fig 6.6 presents the degradation of mixture dye solution with the addition of $K_2Cr_2O_7$ by X1 under Xe lamp irradiation (≧420 nm). The concentration of $Cr_2O_7^{2-}$ is 68×10^{-3} mmol/L, which is 3 times that of the permitted discharge standard in wastewater in China [222]. The result indicates that the addition of $Cr_2O_7^{2-}$ also caused a photocatalytic reduction for the degradation rate. This could be explained by the adsorption of negative charged $Cr_2O_7^{2-}$ on Ag_3PO_4 surface. Because X1 surface is with positive charge, which has a strong attractive force to anion species. Antonopoulou et al. [223] have reported the photocatalytic reduction of Cr (VI) by N-F-codoped TiO_2 suspension. The reduction of Cr (VI) into Cr (III) is attributed to the reducing power of photo-generated electron in the conduction band of TiO_2. Anyway, the conduction band potential of Ag_3PO_4 is +0.45 eV, indicating the photo-generated electrons in Ag_3PO_4 conduction band do not have reducing power. Thus the Cr (VI) can not be reduced into Cr (III) and will maintain during the degradation of RhB-MO mixture dye. Nevertheless, the absorption peak of $Cr_2O_7^{2-}$ at

370 nm has decreased by 22% during the degradation process. It indicates that 22% $Cr_2O_7^{2-}$ could be adsorbed on the surface of Ag_3PO_4. As well as the effect of Cl^-, the adsorption of $Cr_2O_7^{2-}$ will compete with organic molecules for active sites, resulting in the reduction of degradation efficiency. Furthermore, the presence of brunet substance like $Cr_2O_7^{2-}$ can deepen the color of solution, resulting in the attenuation of light penetration [224]. Thus the utilization efficiency of visible light by Ag_3PO_4 would be decreased. That is also a reason for the reduction of degradation efficiency.

In summary, the K^+, Ba^{2+}, Cl^-, NO_3^- and SO_4^{2-} at low concentrations do not affect the degradation of organic dyes mixture over Ag_3PO_4. The exists of Cr^{6+} and Cl^- at high concentration level will significantly weaken the degradation efficiency of organic dyes due to the strong adsorption of $Cr_2O_7^{2-}$ and Cl^- on catalyst surface.

6.4 Stabilities and degradation mechanism

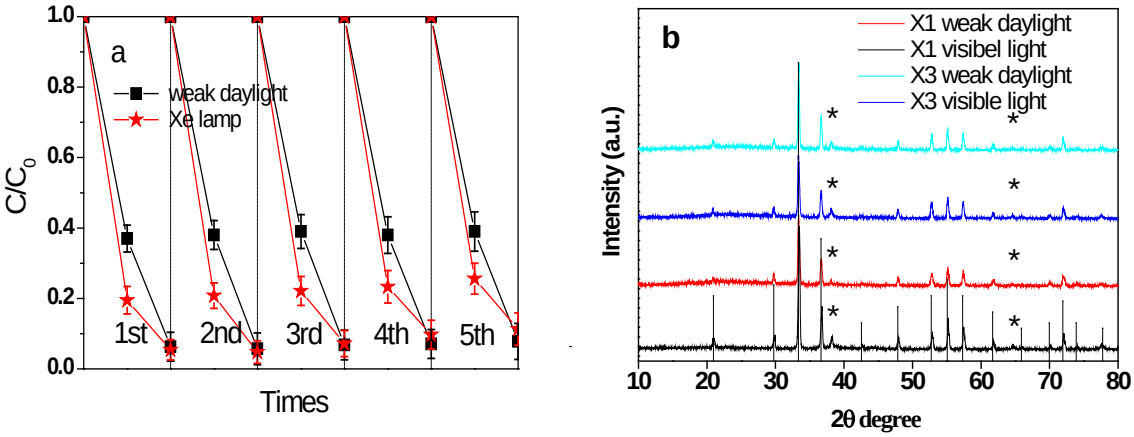

Fig 6.7 (a) Degradation curves of RhB by Ag_3PO_4 dendrites for 5 cycles under weak sunlight (24 h for each run) and artificial visible light (10 min for each run) (≧420 nm); (b) X-ray diffraction (XRD) patterns of Ag_3PO_4 dendrites (X1) and tetrapods (X3) after reactions under natural indoor weak daylight and Xe lamp (≧420 nm).

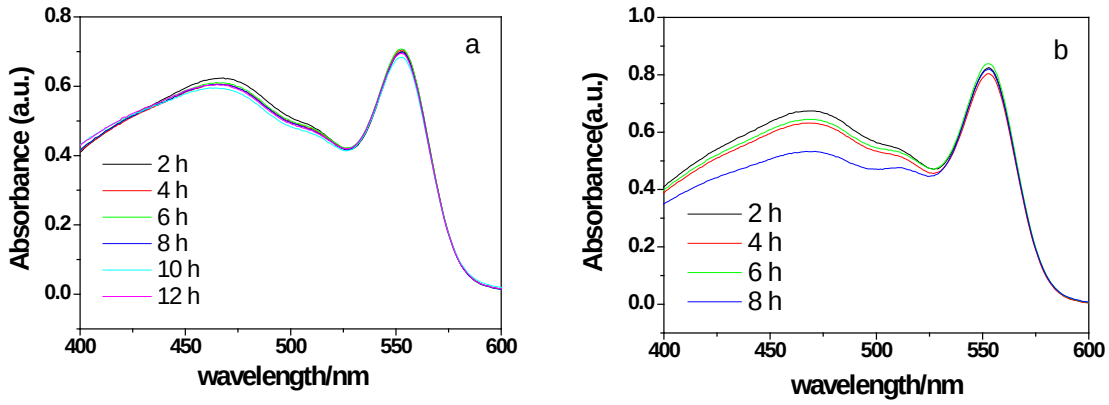

Fig 6.8 Absorption spectra of RhB/MO mixture dyes over Ag_3PO_4 at night (a light density of 28 cd): (a) Fresh Ag_3PO_4 dendrites; (b) Ag/Ag_3PO_4

The stabilities of silver salts-based catalysts are one of the biggest challenges in practical applications in different fields, because silver salts are easily decomposed by heating or exposure to light. For Ag_3PO_4, Ag^+ ion will be easily reduced into Ag by photon electron. It is acknowledged that metal silver does not have photocatalytic activity, thereby decreasing the activity of Ag_3PO_4. The stability of Ag_3PO_4 is even worse in aqueous solution owing to Ag_3PO_4 is slightly soluble in water. The free Ag^+ ion in aqueous solution can be easily reduced into Ag and precipitates on catalyst surface. To investigate the stability of Ag_3PO_4 under natural indoor weak light, the degrading experiment of RhB is repeated for 5 cycles by X1. From **Fig 6.7a**, it can be observed that there is only an insignificant loss in the photocatalytic activity after 5 cycles under natural indoor weak light, while a visual decrease of activity can be observed for visible light irradiation. The results indicate that under natural indoor weak light, the stability of Ag_3PO_4 is better than that under artificial light source. Under Xe lamp irradiation, the light density is thousand times as high as that under natural indoor weak light. As a result, a large number of the generated electrons would greatly reduce Ag (I) to decrease the quantity of Ag_3PO_4, thereby decreasing the activity. Under natural indoor weak light, the reduction reaction of Ag (I) is much weaker due to less electrons excited by the low density light. The rarely generated Ag

on catalyst surface would not decrease the activity of Ag_3PO_4, on the contrast, it could promote the absorption of visible and near-infrared light due to the Surface Plasmon Resonance (SPR). It has been reported [225, 226] that a charge-density oscillation may exist at the interface of two media with dielectric constants of opposite signs, causing extension of light response to the visible and near-infrared spectral regions. The SPR may happen on the Ag/Ag_3PO_4 composite surface, which endows the composite with absorption of near-infrared light. As shown in **Fig 6.8**, fresh Ag_3PO_4 did not show any photocatalytic activity for the degradation of dye under too dim light irradiation (light density of 28 cd). Nevertheless, the absorb intensities of RhB and MO are obviously decreased by the Ag_3PO_4 sample collected after natural indoor weak light irradiation. The results indicate that the Ag/Ag_3PO_4 composite exhibits a degradation activity under a too low light density of 28 cd which may be due to the good absorption of visible and near-infrared light. Therefore, although small amount of Ag emerged under natural indoor weak light, the SPR effect on Ag/Ag_3PO_4 composite could make up the loss of catalyst activity caused by decreasing of Ag_3PO_4. That could be the explanation of that no reduction of activity has been observed after 5 cycles under natural indoor weak light.

However, under strong Xe lamp irradiation, the great loss of activity can not be made up by the good absorption of visible and near-infrared light due to too much loss of Ag_3PO_4 substance. Hence the activity of Ag_3PO_4 has been reduced after cycle experiments under Xe lamp irradiation. Obviously, small amount of emerged Ag would enhance the absorptions of visible and near-infrared light, while large amount of emerged Ag would decrease the photocatalytic activity of Ag_3PO_4. The influence of emerged Ag amounts on photocatalytic activity will be investigated in our future work. The SEM and XRD characterizations of Ag_3PO_4 before and after photocatalytic

reaction also reveal that Ag_3PO_4 is more stable or has longer service life under natural indoor weak light than under artificial light source.

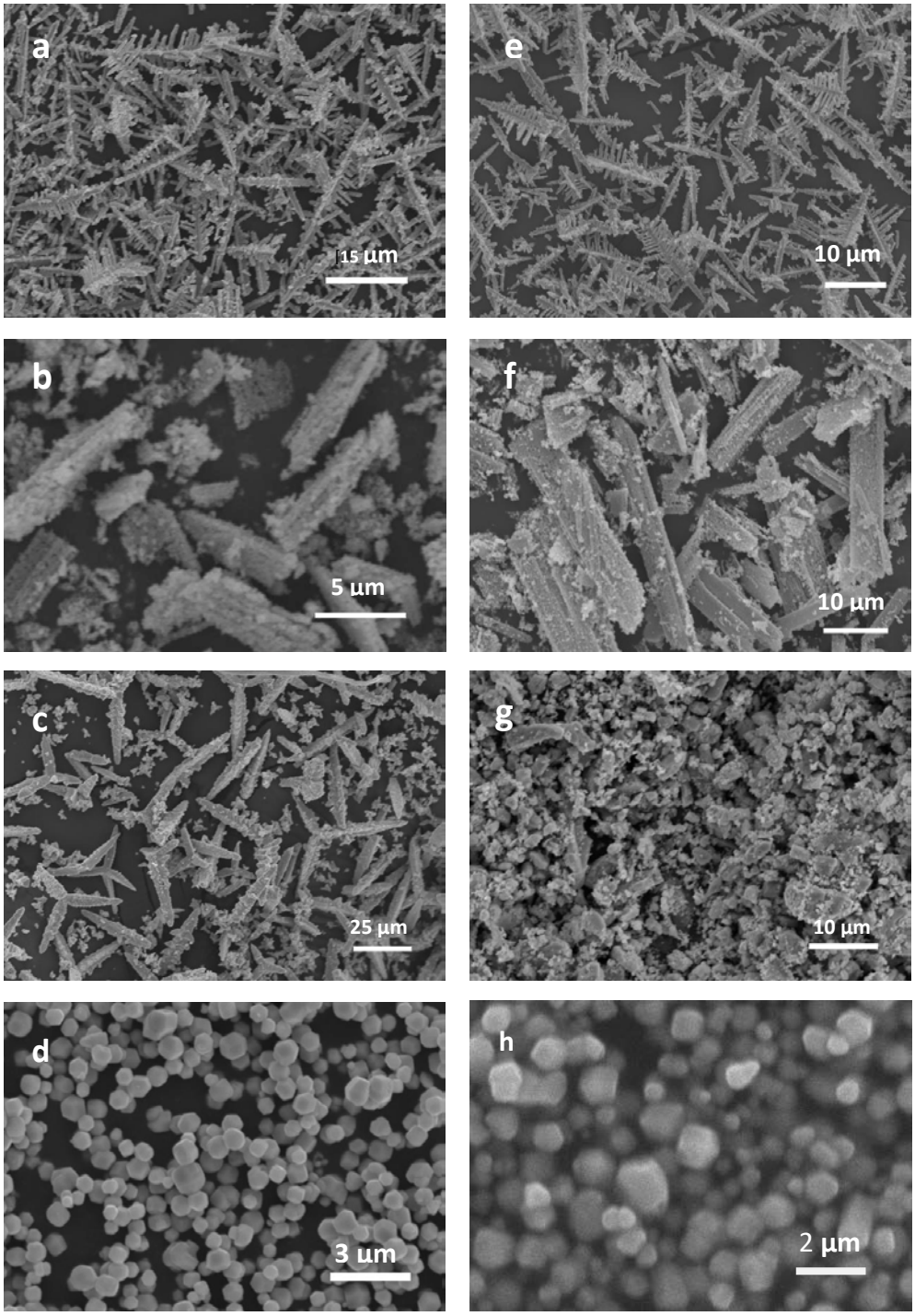

Fig 6.9 SEM images of Ag_3PO_4 samples collected after reactions under natural indoor weak light (a-d) and artificial Xe light source (e-h): (a,e) X1; (b,f) X2; (c,g) X3; (d,h) X4

As shown in **Fig 6.9**, no obvious morphology change of X1 is observed after photocatalytic reaction, indicating the consistent dendrite structure of Ag_3PO_4. In contrast, X2, X3 and X4 have changed or been destructed to different extents, especially under Xe lamp irradiation. Although the differences in SEM images of the samples between that irradiated by natural indoor light and by Xe lamp are not very obvious (especially for sample X1 and X2), it should be noticed that there is a big difference between the irradiation duration under Xe lamp and natural light. The irradiation time of sample under natural indoor light is over 10 days (2 days for each cycle, 5 cycles), while that under Xe lamp is at most 1 hour (10 min for one cycle, 5 cycles). The irradiation time of natural indoor light is 240 times that of Xe lamp, indicating the structure of Ag_3PO_4 is more stable under natural indoor weak light than under artificial light source. XRD patterns of X1 after reactions under natural indoor weak light and visible light are shown in **Fig 6.7b**. Two peaks do not belong to Ag_3PO_4 emerged at 38.1º and 64.4º for all the samples after degradation reactions, which are well in accord with silver (JCPDS no. 04-0783), indicating silver has generated due to light irradiation. However, it is worth noting that the obvious difference in the peak intensity ratio of Ag (38.1º) to Ag_3PO_4 ({110}) can be observed between samples by visible light and natural indoor weak light irradiations. The intensity ratio for the Ag peak and {110} peak is calculated to be 75% with visible light irradiation. In contrast, the intensity ratio for the Ag and {110} peaks is only 22% with weak light irradiation, further supporting that Ag_3PO_4 is more stable under weak light rather than artificial light source. Above all, Ag_3PO_4 may have longer service life under weak light irradiation, compared with that under artificial light source. Otherwise, the weight of Ag_3PO_4 after reaction was measured to be 0.092 g, indicating only 8% of photocatalyst was lost after the degradation process. To state,

the used Ag_3PO_4 was separated from solution by simple centrifugalization which is rough and less effective. In a word, the result indicates Ag_3PO_4 can be effectively separated and recovered after degradation process with small loss of weight, contributing to the effective separation and recovery of catalysts in industrial applications.

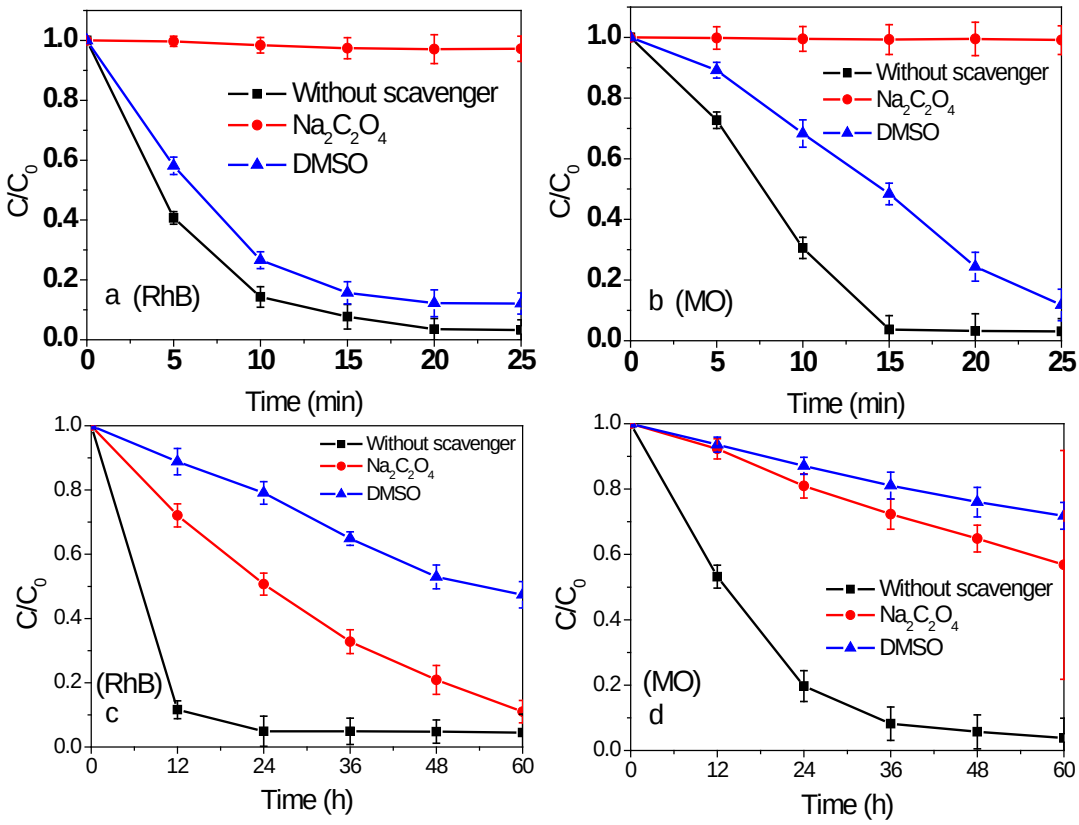

Fig 6.10 Degradation curves of RhB and MO with additions of scavengers ($Na_2C_2O_4$ for trapping hole and DMSO for trapping hydroxyl radical) by Ag_3PO_4 photocatalyst under visible light (a, b) and indoor weak daylight (c, d)

The positive valence band (+2.49 eV) of Ag_3PO_4 suggests that the photogenerated "hole" may have a strong oxidizing power, and/or that more hydroxyls can form. It has been reported that the dye pollutants can be degraded directly by holes for Ag_3PO_4 [227]. Herein, the degradation mechanism of organic dyes by Ag_3PO_4 is investigated. **Fig 6.10** shows the degradation curves of RhB and

MO by Ag_3PO_4 under visible light and weak light. When the hole scavenger ($Na_2C_2O_4$) was added (**Fig 6.10a, b**), the concentrations of both RhB and MO did not decrease, indicating hole plays the vital role in the degradation of organic dye under Xe lamp irradiation. And the addition of dimethyl sulfoxide can reduce the degradation rate of dyes, indicating hydroxyl radical acts as an assisted oxidizing agent in the degradation process. Under natural indoor weak light, however, the degradation continues with the captures of hole or hydroxide radical, demonstrating there could be other process contributing to the degradation of dyes under natural indoor weak light. We attribute the degradation of pollutants out from photocatalytic process to the self-degradation of organic dyes. As it is known, some organic dyes could absorb the light of region above 420 nm and react with dissolved oxygen to form $O_2^{\bullet -}$ and $dye^{\bullet +}$, thus provoking the self-attack to the organic dyes. The self-degradation requires a long induction period and it only occurs at long irradiation times [228]. In our experiments, the reaction time for visible light degradation is 25 minutes, which would be too short for the induction period of self-degradation process. Under the natural indoor weak light irradiation the reaction time is 60 hours, which is much longer than that under visible light. The long reaction time satisfies the condition of the occurrence of self-degradation process and the degradation of dyes becomes more apparent as the reaction progresses with the time.

6.5 Summary of Chapter 6

Ag_3PO_4 photocatalysts show excellent photocatalytic activity for the degradation of multi-component organic dyes under natural solar energy. The dye mixture (RhB 10 mg L^{-1}, MO 10 mg L^{-1}) is degraded by Ag_3PO_4 dendrites in 28 h by entirely using natural indoor weak light. The high-concentration Cl^- and Cr^{6+} ions in wastewater can

significantly decrease the degradation rate of dyes, while K^+, Ba^{2+}, NO^{3-} and SO_4^{2-} do not affect the degradation processes of dyes. Moreover, Ag_3PO_4 dendrites shows higher stability under natural indoor weak light compared with that by Xe lamp irradiation, since the reduction of Ag(I) into Ag is refrained obviously. This discovery could be a suitable, efficient strategy for the application of Ag-containing photocatalysts in actual wastewater purification, which could be extended to indoor air cleaning process.

Chapter 7 Conclusions and suggestions for future work

In this Chapter, an overall conclusion of the work presented in this thesis is given as the experimental results and the contribution has been made to the field. Suggestions for future work followed by this project are also presented.

7.1 Conclusions

The work conducted in this thesis aims to develop a silver phosphate catalyst with enhanced photocatalytic activity for the oxidation of industrial wastewaters containing organic dyes. The entire work can be divided into two stages as catalyst preparation and property evaluation. In the first stage, a Ag_3PO_4 catalyst with specific nanostructure and high photocatalyic activity has been fabricated and systematically investigated. In the second stage, the influences on organic dyes degradation by Ag_3PO_4 have been conducted. Particularly, the photocatalytic activity and stability of Ag_3PO_4 have been investigated by utilizing natural light, which contributes to practical application of Ag_3PO_4 by solar energy in industrial wastewater purification.

An efficient Ag_3PO_4 photocatalyst has been synthesized by a facile method at room temperature. The material was found with hollow tube-like structure and consist of large numbers of nanoparticles with an average diameter of 100 nm. The hollow structure, large surface area, small dimension endow the catalyst with greatly high photocatalytic activity for organic dyes degradation. PEG 200 as a solvent played a vital role in the crystal growth and the formation of nanostructure. It was found that the catalyst has excellent degradation efficiency for cationic organic dye due to its

surface property. Moreover, the effects of pH value on photocatalytic activity and stability of Ag_3PO_4 have been studied. The results indicate acidic condition favors for efficient oxidation of organic dyes, while neutral condition favors for the optimal balance of activity and stability of Ag_3PO_4.

Ag_3PO_4 semiconductors were found with high photocatalytic activity under natural light. A RhB-MO mixture dye (10 mg L^{-1} for each dye) has been completely degraded by Ag_3PO_4 in 28 hours entirely using solar energy. The intensity of light for photocatalytic reaction is as low as 72 cd, which is one-thousandth that of a standard Xe lamp ($68.2*10^3$ cd). Moreover, it was proved that the exists of Cr^{6+} and Cl^- at high concentration level significantly weaken the degradation efficiency of organic dyes due to the strong adsorption of $Cr_2O_7^{2-}$ and Cl^- on catalyst surface. The adsorbed $Cr_2O_7^{2-}$ and Cl^- will compete with organic molecules for active sites, resulting in the reduction of degradation efficiency. Finally, the photo stability of Ag_3PO_4 under indoor weak light was proved to be better than that under Xe lamp, which is attributed to the proper amount of generated Ag on catalyst surface.

In summary, Ag_3PO_4 microtubes with coarse particle surface were synthesized for the first time. The obtained specific morphology has further enhanced the photocatalytic activity of Ag_3PO_4, as well as the light utilization efficiency. And photocatalytic degradations of anionic and cationic dyes over Ag_3PO_4 by utilizing natural sunlight were performed, contributing to practical wastewater purification by photocatalysis.

7.2 Suggestions for future work

There are several problems should be taken into concern in the future work. The SPMs exhibited super-high acitivty for cationic dye degradation due to the specific surface property. In the next step, the surface property of SPMs should be further investigated. And SPMs could be expanded to the degradations of other cationic dyes in various types.

PEG 200 has been demonstrated playing a vital role in the formation of the tube-like structure. PEG with higher molecular weight should be applied in the preparation of Ag_3PO_4. The viscosity of the system will increase as PEG 300, 400 used as solvent. The increasing interaction force would slow the growth rate and obtain Ag_3PO_4 with other morphologies. The organic solvents other than PEG should also be used to explore novel Ag_3PO_4 photocatalyst with optimal morphology.

Photo-generated electrons on Ag_3PO_4 surface would reduce Ag^+ into Ag, resulting in reduction of photocatalytic activity. It could be an effective way to inhibit the reduction of activity by removing or exporting the electrons in the conduction band of Ag_3PO_4. Hence, experiments on coupling Ag_3PO_4 with semiconductors with suitable band gap structure should be considered. Otherwise, it is also a good choice to use a electrode to export the photo-genenrated electrons on Ag_3PO_4 surface. Thus, the stability of Ag_3PO_4 could be enhanced to meet the requirement of long service life.

Individual and mixed dyes of RhB and MO were degraded under either Xe lamp and natural sunlight in this work. The oxidizing products and intermediates of these

two organic dyes should be analyzed by high performance liquid chromatography (HPLC). The analysis of the oxidizing products and intermediates will help better understanding the degradation mechanism of Ag_3PO_4. Besides, the influence of anxillary compounds (sodium carbonate, surfactant, benzene and dispersant) used in dyeing process should also be concerned.

Reference

1. Tseng T K, Yi S L, Yi J C, et al. A Review of Photocatalysts Prepared by Sol-Gel Method for VOCs Removal. *Int. J. Mol. Sci.*, **2010**, 11(6):2336.
2. Wang M, Ioccozia J, Sun L, et al. Inorganic-modified semiconductor TiO_2 nanotube arrays for photocatalysis. *Energ. Environ. Sci.*, **2014**, 7(7):2182-2202.
3. Huang J Y, Zhang K Q, Lai Y K. Fabrication, Modification, and Emerging Applications of TiO_2 Nanotube Arrays by Electrochemical Synthesis: A Review. *Int. J. Photoenergy*, **2013**, 112(15):4696-701.
4. Martin D J, Liu G, Moniz S J A, et al. Efficient Visible Driven Photocatalyst, Silver Phosphate: Performance, Understanding and Perspective. *Chem. Soc. Rev.*, **2015**, 44(21):7808.
5. Huang L, Wang H, Chen J, et al. Synthesis, morphology control, and properties of porous metal–organic coordination polymers. *Micropor. Mesopor. Mat.*, **2003**, 58(2):105-114.
6. Ellis B, Wang H K, Makahnouk W R M, et al. Synthesis of nanocrystals and morphology control of hydrothermally prepared $LiFePO_4$. *J. Mater. Chem.*, **2007**, 17(30):3248-3254.
7. And X Y, Joachim Loos. Toward High-Performance Polymer Solar Cells: The Importance of Morphology Control. *Macromolecules*, **2007**, 40(5):1353-1362.
8. Kiang Y H, Gardner G B, Stephen Lee A, et al. Porous Siloxane Linked Phenylacetylene Nitrile Silver Salts from Solid State Dimerization and Low Polymerization. *J. Am. Chem. Soc.*, **2000**, 122(122):6871-6883.
9. Yi Z. An orthophosphate semiconductor with photooxidation properties under visible-light irradiation. *Nature. Mater.*, **2010**, 9(7):559-564.
10. Chen Z, Wang W, Zhang Z, et al. High-Efficiency Visible-Light-Driven Ag_3PO_4/AgI Photocatalysts: Z-Scheme Photocatalytic Mechanism for Their Enhanced Photocatalytic Activity. *J. Phys. Chem. C*, **2015**, 117(38):19346-19352.
11. Luo Y, Xu N, Liu X, et al. Photoactivity Enhanced and Photo-Corrosion Inhibited Ag_3PO_4/ZnO Visible Light Photocatalyst for the Degradation of Rhodamine B. *Energ. Environ. Focus.*, **2015**, 4(2):121-127(7).
12. Stephenson T. Membrane bioreactors for wastewater treatment. *London: IWA*, **2000**.

13. Lettinga G, Van Velsen A F M, Hobma S W, et al. Use of the up-flow sludge blanket (USB) reactor concept for biological wastewater treatment, especially for anaerobic treatment. *Biotechnol. Bioeng.*, **1980**, 22(4): 699-734.
14. Patterson J W. Industrial wastewater treatment technology. **1985**.
15. Henze M. Wastewater treatment: biological and chemical processes. *Springer. Sci. Bus. Med.*, **2002**.
16. Ngah W S W, Hanafiah M. Removal of heavy metal ions from wastewater by chemically modified plant wastes as adsorbents: a review. *Bioresource. Technol.*, **2008**, 99(10): 3935-3948.
17. Robinson T, McMullan G, Marchant R, et al. Remediation of dyes in textile effluent: a critical review on current treatment technologies with a proposed alternative. *Bioresource. Technol.*, **2001**, 77(3): 247-255.
18. Meyer F, Meyer-Hofmeister E. On the elusive cause of cataclysmic variable outbursts. *Astron. Astrophy*., **1981**, 104: L10.
19. Zollinger H. *Color. Chem.*, **1987**.
20. Zollinger H. Synthesis, properties and applications of organic dyes and pigments. *Color. Chem*., **2002**.
21. Weber E J, Stickney V C. Hydrolysis kinetics of reactive blue 19-vinyl sulfone. *Water. Res*., **1993**, 27(1): 63-67.
22. Houas A, Lachheb H, Ksibi M, et al. Photocatalytic degradation pathway of methylene blue in water. *Appl. Catal. B: Environ.*, **2001**, 31(2): 145-157.
23. Poots V J P, McKay G, Healy J J. The removal of acid dye from effluent using natural adsorbents: I peat. *Water. Res.*, **1976**, 10(12): 1061-1066.
24. Zhang N, Zhao M, Wang C, et al. Decolorization of dyes by recombinase CotA from Escherichia coli BL21 (DE3) and characterization of the purified enzyme. *Afr. J. Biotechnol.*, **2012,**(24):6603-6611.
25. Grines C L, Cox D A, Stone G W, et al. Coronary angioplasty with or without stent implantation for acute myocardial infarction. *New. Engl. J. Med.*, **1999**, 341(26): 1949-1956.
26. Hadi M, Samarghandi M R, Mckay G. Simplified Fixed Bed Design Models for the Adsorption of Acid Dyes on Novel Pine Cone Derived Activated Carbon. *Water, Air, & Soil*

Pollution, **2011**, 218(1):197-212.

27. Ip A W M, Barford J P, Mckay G. Reactive Black dye adsorption/desorption onto different adsorbents: Effect of salt, surface chemistry, pore size and surface area. *J. Colloid. Interf. Sci.*, **2009**, 337(1):32-38.
28. Berenguer R, Marco-Lozar J P, Quijada C, et al. Electrochemical regeneration and porosity recovery of phenol-saturated granular activated carbon in an alkaline medium. *Carbon*, **2010**, 48(10):2734-2745.
29. Lampinen R. waste waters treatment produced in connection with papermaking, by dehydration and mixing with solid fuel such as peat, bark, wood chips, sawdust, then burning in a power boiler; heat transfer; cost efficiency: US, US 7575657 B2. **2009**.
30. Kałużna–Czaplińska J, Gutowska A, Jóźwiak W K. The chemical degradation of C.I. Acid Brown 349 in aqueous solution using hydrogen peroxide and sodium hypochlorite and its implications for biodegradation. *Dyes Pigments*, **2010**, 87(1):62-68.
31. Mikutta R. Review: organic matter removal from soils using hydrogen peroxide, sodium hypochlorite, and disodium peroxodisulfate. *Soil. Sci. Soc. Am. J.*, **2005**, 69(1):120-135.
32. Mascolo G, Spinosa L, Lotito V, et al. Lab-scale evaluations on formation of products of incomplete combustion in hazardous waste incineration: Influence of process variables. *Wat. Sci. Technol.*, **1997**, 36(11):219-226.
33. Naito S, Tanaka K, Koga H, et al. Cancer occurrence among dyestuff workers exposed to aromatic amines: A long term follow-up study. *Cancer*, **1995**, 76(8):1445.
34. Buschmann H J, Cleve E, Schollmeyer E, Cucurbituril as a ligand for the complexation of cations in aqueous solutions. *Inorg. Chim. Acta*, **1992**, 193(1): 93-97.
35. Barr D P, Aust S D. Mechanisms white rot fungi use to degrade pollutants. *Environ. Sci. Technol*., **1994**, 28(2): 78A-87A.
36. Oppenländer T. Photochemical Purification of Water and Air: Advanced oxidation processes: principles, reaction mechanisms, reactor concepts. *John Wiley Sons*, **2003**.
37. Stasinakis A S. Use of selected advanced oxidation processes for wastewater treatment: a mini review. *Glob. NEST J.*, **2008**, 10(3): 376-385.
38. Fujishima A, Rao T N, Tryk D A. Titanium dioxide photocatalysis. *J. Photoch. Photobio. C: Photochem. Rev.*, **2000**, 1(1): 1-21.

39. Chen X, Mao S S. Titanium dioxide nanomaterials: synthesis, properties, modifications, and applications. *Chem. Rev.*, **2007**, 107(7): 2891-2959.
40. Carp O, Huisman C L, Reller A. Photoinduced reactivity of titanium dioxide. *Prog. Solid. State. Chem.*, **2004**, 32(1): 33-177.
41. Bickley R I, Gonzalez-Carreno T, Lees J S, et al. A structural investigation of titanium dioxide photocatalysts. *J. Solid. State. Chem.*, **1991**, 92(1): 178-190.
42. Kato S, Masuo F. Titanium dioxide photocatalyzed liquid phase oxidation of tetralin, *Kogyo Kagaku Zasshi*, **1964**, 67: 1136-1140.
43. Fujishima A, Honda K. Photolysis-decomposition of water at the surface of an irradiated semiconductor. *Nature*, **1972**, 238(5385): 37-38.
44. Fujishima A, Ohtsuki J, Yamashita T, et al. Behavior of tumor cells on photoexcited semiconductor surface. *Photomed. Photobiol.*, **1986**, 8: 45-46.
45. O'regan B, Grätzel M. A low-cost, high-efficiency solar cell based on dye-sensitized colloidal TiO2 films. *Nature*, **1991**, 353(6346): 737-740.
46. Wang R, Hashimoto K, Fujishima A, et al. Light-induced amphiphilic surfaces. *Nature*, **1997**, 388: 431-432.
47. Sonawane R S, Kale B B, Dongare M K. Preparation and photo-catalytic activity of Fe TiO2 thin films prepared by sol–gel dip coating. *Mater. Chem. Phys*., **2004**, 85(1): 52-57.
48. Mizukoshi Y, Ohtsu N, Semboshi S, et al. Visible light responses of sulfur-doped rutile titanium dioxide photocatalysts fabricated by anodic oxidation. *Appl. Catal. B: Environ.*, **2009**, 91(1): 152-156.
49. Li R H, Chen W X, Kobayashi H, et al. Platinum-nanoparticle-loaded bismuth oxide: an efficient plasmonic photocatalyst active under visible light. *Green. Chem.*, **2010**, 12(2):212-215.
50. Zhang S, Li J, Zeng M, et al. In situ synthesis of water-soluble magnetic graphitic carbon nitride photocatalyst and its synergistic catalytic performance. *Acs. Appl. Mater. Interf.*, **2013**, 5(23):12735.
51. Van Doorslaer X, Demeestere K, Heynderickx P M, et al. UV-A and UV-C induced photolytic and photocatalytic degradation of aqueous ciprofloxacin and moxifloxacin: reaction kinetics and role of adsorption. *Appl. Catal. B: Environ.*, **2011**, 101(3): 540-547.

52. Stafford U, Gray K A, Kamat P V. Radiolytic and TiO_2-assisted photocatalytic degradation of 4-chlorophenol. A comparative study. *J. Phys. Chem.*, **1994**, 98(25): 6343-6351.
53. Chatterjee D, Patnam V R, Sikdar A, et al. Kinetics of the decoloration of reactive dyes over visible light-irradiated TiO_2 semiconductor photocatalyst. *J. Hazard. Mater.*, **2008**, 156(1): 435-441.
54. Byrappa K, Yoshimura M. Physical Chemistry of Hydrothermal Growth of Crystals - Handbook of Hydrothermal Technology - 4. *Handbook of Hydrotherm. Technol.*, **2001**:161–197.
55. Bunsen R. Bemerkungen zu einigen Einwürfen gegen mehrere Ansichten über die chemisch-geologischen Erscheinungen in Island. *Eur. J. Org. Chem.*, **2010**, 65(1):70-85.
56. Riesco M R, Martínez-Casado F J, Cheda J A R, et al. Study of the Polymorphism in Copper(II) Decanoate through Its Phase Diagram with Decanoic Acid, and Texture of the Columnar Thermotropic Liquid Crystal Developable Domains in This and Similar Systems. *Cryst. Growth. Des.*, **2015**, 15(1).
57. Yu J, Yu X. Hydrothermal synthesis and photocatalytic activity of zinc oxide hollow spheres. *Environ. Sci. Technol*., **2008**, 42(13): 4902-4907.
58. Lu F, Cai W, Zhang Y. ZnO hierarchical micro/nanoarchitectures: solvothermal synthesis and structurally enhanced photocatalytic performance. *Adv. Funct. Mater.*, **2008**, 18(7): 1047-1056.
59. Joshi U A, Jang J S, Borse P H, et al. Microwave synthesis of single-crystalline perovskite $BiFeO_3$ nanocubes for photoelectrode and photocatalytic applications. *Appl. Phys. Lett.*, **2008**, 92(24): 242106-242106.
60. Fey G T K, Yang H Z, Kumar T P, et al. A simple mechano-thermal coating process for improved lithium battery cathode materials. *J. Power. Sources.*, **2004**, 132(1): 172-180.
61. Hou X, Feng J, Xu X, et al. Synthesis and characterizations of spinel $MnFe_2O_4$ nanorod by seed–hydrothermal route. *J. Alloy. Comp.*, **2010**, 491(1): 258-263.
62. Cahn J W. Theory of Crystal Growth and Interface Motion in Crystalline Materials. *Acta Metallurgica*, **1960**, 8(8):554-562.
63. Pan C S. New type of $BiPO_4$ oxy-acid salt photocatalyst with high photocatalytic activity on degradation of dye. *Environ. Sci. Technol.*, **2010**, 44(14):5570.

64. Livage J. Basic Principles of Sol-Gel Chemistry Sol-Gel Technologies for Glass Producers and Users. *Springer US*, **2004**:3-14.

65. Dislich H, Hinz P. History and principles of the sol-gel process, and some new multicomponent oxide coatings. *J. Non-Cryst. Solids*, **1982**, 48(1):11-16.

66. Yoldas B E. A Transparent Porous Alumina. *Am. Ceram. Soc. Bull.*, **1975**, 54(3):286-288.

67. Ling J H, Zhang Y Y, Wang S Y. Synthesis and Crystal Structure of Dichloro (2,6-dimethylpyridine) Copper(II) [Cu $(C_7H_9N)_2]Cl_2$. *J. Qingdao I. Chem. Technol.*, **2000**.

68. Weber E J, Stickney V C. Hydrolysis kinetics of reactive blue 19-vinyl sulfone. *Water .Res.*, **1993**, 27(1): 63-67.

69. Houas A, Lachheb H, Ksibi M, et al. Photocatalytic degradation pathway of methylene blue in water. *Appl. Catal. B: Environ.*, **2001**, 31(2): 145-157.

70. Bloemen L J, Youk A, Bradley T D, et al. Lymphohaematopoietic cancer risk among chemical workers exposed to benzene. *Occup. Environ. Med.*, **2004**, 61(3): 270-274.

71. Huang Y, Ho S S, Lu Y, et al. Removal of Indoor Volatile Organic Compounds via Photocatalytic Oxidation: A Short Review and Prospect. *Molecules*, **2016**, 21(1):56.

72. Lin L, Chai Y, Zhao B, et al. Photocatalytic oxidation for degradation of VOCs. *J. Inorg. Chem.*, **2013**, 03(1):14-25.

73. Thiruvenkatachari R, Vigneswaran S, Moon I S. A review on UV/TiO_2 photocatalytic oxidation process. *Korean. J. Chem. Eng*., **2008**, 25(1): 64-72.

74. Matthews R W, McEvoy S R. Photocatalytic degradation of phenol in the presence of near-UV illuminated titanium dioxide. *J. Photochem. Photobio. A: Chem*., **1992**, 64(2): 231-246.

75. Li Puma G, Yue P L. Photocatalytic oxidation of chlorophenols in single-component and multicomponent systems. *Ind. Eng. Chem. Res.*, **1999**, 38(9): 3238-3245.

76. Shon H. Ultrafiltration and nanofiltration hybrid systems in wastewater treatment and reuse. *University of Technology, Sydney*, **2005**.

77. Haarstrick A, Kut O M, Heinzle E. TiO_2-assisted degradation of environmentally relevant organic compounds in wastewater using a novel fluidized bed photoreactor. *Environ. Sci. Technol*., **1996**, 30(3): 817-824.

78. Nishikiori H, Qian W, El-Sayed M A, et al. Change in titania structure from amorphousness to

crystalline increasing photoinduced electron-transfer rate in dye-titania system. *J. Phys. Chem. C*, **2007**, 111(26): 9008-9011.

79. Fu H, Zhang S, Xu T, et al. Photocatalytic degradation of RhB by fluorinated Bi_2WO_6 and distributions of the intermediate products. *Environ. Sci. Technol.*, **2008**, 42(6):2085.
80. Li X Z, Zhao W, Zhao J C. Visible light-sensitized semiconductor photocatalytic degradation of 2,4-dichlorophenol. *Sci. China. Ser. B:Chem*., **2002**, 45: 421–425
81. www.flickr.com/photos/53465598@N07/5113266175
82. Pacheco-Torgal F, Jalali S. Nanotechnology: advantages and drawbacks in the field of construction and building materials. *Constr. Build. Mater*., **2011**, 25(2): 582-590.
83. Chen J, Poon C. Photocatalytic construction and building materials: from fundamentals to applications. *Build. Environ*., **2009**, 44(9): 1899-1906.
84. Ohama Y, Van Gemert, Application of titanium dioxide photocatalysis to construction materials: state-of-the-art report of the RILEM technical committee 194-TDP. *Springer Sci. Bus. Media.*, **2011**.
85. Watanabe T, Nakajima A, Wang R, et al. Photocatalytic activity and photoinduced hydrophilicity of titanium dioxide coated glass. *Thin. Solid. Films*., **1999**, 351(1): 260-263.
86. Benedix R, Dehn F, Quaas J, et al. Application of titanium dioxide photocatalysis to create self-cleaning building materials. *Lacer*, **2000**, 5: 157-168.
87. Wang R, Hashimoto K, Fujishima A, et al. Photogeneration of highly amphiphilic TiO 2 surfaces. *Advan. Mater.*, **1998**, 10(2): 135-138.
88. Bekbölet M. Photocatalytic bactericidal activity of TiO_2 in aqueous suspensions of E. coli. *Water. Sci. Technol.*, **1997**, 35(11): 95-100.
89. Dadjour M F, Ogino C, Matsumura S, et al. Kinetics of disinfection of Escherichia coli by catalytic ultrasonic irradiation with TiO_2. *Biochem. Eng. J*., **2005**, 25(3): 243-248.
90. Saito T, Iwase T, Horie J, et al. Mode of photocatalytic bactericidal action of powdered semiconductor TiO_2 on mutans streptococci. *J. Photochem. Photobio. B: Bio*l., **1992**, 14(4): 369-379.
91. Huang Z, Maness P C, Blake D M, et al. Bactericidal mode of titanium dioxide photocatalysis. *J. Photochem. Photobio. A: Chem.*, **2000**, 130(2): 163-170.
92. Fujishima A, Hashimoto K, Watanabe T. TiO_2 Photocatalysis, Bkc. Inc., *Tokyo, Japan*, **1999**.

93. Ma X, Wu Y, Lu Y, et al. Effect of Compensated Codoping on the Photoelectrochemical Properties of Anatase TiO_2 Photocatalyst. *J. Phys. Chem. C*, **2011**, 115(34):16963-16969.

94. Martin D J, Umezawa N, Chen X, et al. Facet engineered Ag_3PO_4 for efficient water photooxidation. *Energ. Environ. Sci.*, **2013**, 6(11):3380-3386.

95. Jiang B, Wang Y, Wang J Q, et al. In Situ Fabrication of Ag/Ag_3PO_4/Graphene Triple Heterostructure Visible Light Photocatalyst through Graphene-Assisted Reduction Strategy. *ChemCatChem*, **2013**, 5(6): 1359-1367.

96. Zhang H, Huang H, Ming H, et al. Carbon quantum dots/Ag_3PO_4 complex photocatalysts with enhanced photocatalytic activity and stability under visible light. *J. Mater. Chem.*, **2012**, 22(21): 10501-10506.

97. Yao W, Zhang B, Huang C, et al. Synthesis and characterization of high efficiency and stable Ag_3PO_4/TiO_2 visible light photocatalyst for the degradation of methylene blue and rhodamine B solutions. *J. Mater. Chem*., **2012**, 22(9): 4050-4055.

98. Liang Q, Shi Y, Ma W, et al. Enhanced photocatalytic activity and structural stability by hybridizing Ag_3PO_4 nanospheres with graphene oxide sheets. *Phys. Chem. Chem. Phys*., **2012**, 14(45): 15657-15665.

99. Yang X, Cui H, Li Y, et al. Fabrication of Ag_3PO_4-graphene composites with highly efficient and stable visible light photocatalytic performance. *ACS. Catal*., **2013**, 3(3): 363-369.

100. Yang H G, Sun C H, Qiao S Z, et al. Computational and experimental studies of non-metal-terminated surfaces of anatase and rutile TiO_2. *Nanotech*., **2008**, 1:755-757.

101. Yang Z, Tao Y, Xin T, et al. SDS-assisted solvothermal synthesis of rose-like BiOBr partially enclosed by {111} facets and enhanced visible-light photocatalytic activity. *Dalton Transactions*, **2015**, 44(47):20475-20483.

102. Wang X, Liu C, Zheng B, et al. Controlled Synthesis of Concave Cu_2O Microcrystals Enclosed by hhl High-index Facets and Enhanced Catalytic Activity. *J. Mater. Chem.*, **2013**, 1(2):282-287.

103. Wang W, Lu C, Ni Y, et al. A new sight on hydrogenation of F and N-F doped {001} facets dominated anatase TiO_2, for efficient visible light photocatalyst. *Appl. Catal. B Environ.*, **2012**, 127(43):28-35.

104. Li X, Zhu J, Li H. Influence of crystal facets and F-modification on the photocatalytic

performance of anatase TiO_2. *Catal. Commun.*, **2012**, 24(26):20-24.

105. Reinhold C. The many faces of Pt nanoparticles : Nanotechnology. *Mater. Today*, **2007**, 10(7):10-10.

106. Jiao Z, Zhang Y, Yu H, et al. Concave trisoctahedral Ag_3PO_4 microcrystals with high-index facets and enhanced photocatalytic properties. *Chem. Commun.*, **2013**, 49(6):636.

107. Yu J, Low J, Xiao W, et al. Enhanced photocatalytic CO_2-reduction activity of anatase TiO_2 by coexposed {001} and {101} facets. *J. Am. Chem. Soc.*, **2014**, 136(25):8839-42.

108. Dinh C T, Nguyen T D, Kleitz F, et al. Shape-Controlled Synthesis of Highly Crystalline Titania Nanocrystals. *Acs. Nano.*, **2009**, 3(11):3737.

109. Dong P, Wang Y, Li H, et al. Shape-controllable synthesis and morphology-dependent photocatalytic properties of Ag_3PO_4 crystals. *J. Mater. Chem. A*, **2013**, 1(15):4651-4656.

110. Amornpitoksuk P, Intarasuwan K, Suwanboon S, et al. Effect of Phosphate Salts (Na_3PO_4, Na_2HPO_4, and NaH_2PO_4) on Ag_3PO_4 Morphology for Photocatalytic Dye Degradation under Visible Light and Toxicity of the Degraded Dye Products. *Ind. Eng. Chem. Res.*, **2013**, 52(49):17369-17375.

111. Dong L, Wang P, Wang S, et al. A simple way for Ag_3PO_4, tetrahedron and tetrapod microcrystals with high visible-light-responsive activity. *Mater. Lett.*, **2014**, 134(11):158-161.

112. Vu T A, Dao C D, Hoang T T T, et al. Highly photocatalytic activity of novel nano-sized Ag_3PO_4, for Rhodamine B degradation under visible light irradiation. *Mater. Lett.*, **2013**, 92(1):57-60.

113. Yan X, Gao Q, Qin J, et al. Morphology-controlled synthesis of Ag_3PO_4, microcubes with enhanced visible-light-driven photocatalytic activity. *Ceram. Int.*, **2013**, 39(8):9715-9720.

114. Kai W, Xu J, Xia H, et al. Highly efficient photodegradation of RhB-MO mixture dye wastewater by Ag_3PO_4, dodecahedrons under acidic condition. *J. Mol. Catal. A Chem.*, **2014**, 393(18):302-308.

115. Wang J, Teng F, Chen M, et al. Facile synthesis of novel Ag_3PO_4 tetrapods and the {110} facets-dominated photocatalytic activity. *Crystengcomm*, **2012**, 15(1):39-42.

116. Xu Y S, Zhang W D. Morphology-controlled synthesis of Ag_3PO_4 microcrystals for high performance photocatalysis. *Crystengcomm*, **2013**, 15(27):5407-5411.

117. Li M. Branching growth of novel silver phosphate dendrites and the greatly improved

photocatalytic activity by the active {110} facets. *Crystengcomm*, **2014**, 16(7):1237-1240.

118. Bi Y, Hu H, Jiao Z, et al. Two-dimensional dendritic Ag_3PO_4 nanostructures and their photocatalytic properties. *Phys. Chem. Chem. Phys.*, **2012**, 14(42):14486.

119. Li X Z, Wu K L, Dong C, et al. Size-controlled synthesis of Ag_3PO_4, nanorods and their high-performance photocatalysis for dye degradation under visible-light irradiation. *Mater. Lett.*, **2014**, 130(5):97-100.

120. Pang F, Liu X T, He M Y, et al. Ag_3PO_4 colloidal nanocrystal clusters with controllable shape and superior photocatalytic activity. *Nano. Res.*, **2015**, 8(1):106-116.

121. Yang Z M, Tian Y, Huang G F, et al. Novel 3D flower-like Ag_3PO_4, microspheres with highly enhanced visible light photocatalytic activity. *Mater. Lett.*, **2014**, 116(2):209-211.

122. Menezes P W, Indra A, Littlewood P, et al. Nanostructured manganese oxides as highly active water oxidation catalysts: a boost from manganese precursor chemistry. *Chemsuschem*, **2014**, 7(8):2202-2211.

123. Jiang B, Wang Y, Wang J Q, et al. In Situ Fabrication of Ag/Ag_3PO_4 /Graphene Triple Heterostructure Visible-Light Photocatalyst through Graphene-Assisted Reduction Strategy. *Chemcatchem*, **2013**, 5(6):1359–1367.

124. Dong P, Wang Y, Cao B, et al. Ag_3PO_4 /reduced graphite oxide sheets nanocomposites with highly enhanced visible light photocatalytic activity and stability. *Appl. Catal. B Environ.*, **2013**, s 132–133(9):45-53.

125. Lou Z, Huang B, Wang Z, et al. Fast-generation of Ag_3PO_4 concave microcrystals from electrochemical oxidation of bulk silver sheet. *Crystengcomm*, **2013**, 15(25):5070-5075.

126. Peng Liu, Wangdong Qi, Yue Zhang, et al. On the Unambiguous Distance of Multi-Carrier Phase Ranging with Random Hopped Frequencie. **2017**.

127. Wagner P, Gordon I, Mangin S, et al. Influence of the cooperative Jahn-Teller effect on the transport and magnetic properties of single crystals. *Phys. Rev. B Condens. Mat.*, **2000**, 61(1):529-537.

128. Sakaguchi K, Shimakawa K, Hatanaka Y. Transport and recombination of photo-carriers under potential fluctuation in TiOx, films prepared by rf magnetron sputtering method. *Phys. Status. Solidi.*, **2011**, 8(9):2796–2799.

129. Müller J G, Lupton J M, Feldmann J, et al. Ultrafast dynamics of charge carrier

photogeneration and geminate recombination in conjugated polymer: Fuller. Sol. C. **2005**, 72(19):5208.

130. Li C, Zhang P, Lv R, et al. Selective Deposition of Ag_3PO_4, on Monoclinic $BiVO_4$ (040) for Highly Efficient Photocatalysis. *Small*, **2013**, 9(23):3951–3956.

131. Zhang S, Zhang S, Song L. Super-high activity of Bi^{3+}, doped Ag_3PO_4, and enhanced photocatalytic mechanism. *Appl. Catal. B Environ.*, **2014**, s 152–153(12):129-139.

132. Wu Q, Diao P, Sun J, et al. Draining the photoinduced electrons away from an anode: the preparation of Ag/Ag_3PO_4 composite nanoplate photoanodes for highly efficient water splitting. *J. Mater. Chem. A*, **2015**, 3(37):18991-18999.

133. Liu L, Liu J, Sun D D. Graphene oxide enwrapped Ag_3PO_4 composite: towards a highly efficient and stable visible-light-induced photocatalyst for water purification. *Catal. Sci. Technol.*, **2012**, 2(12):2525-2532.

134. Bo C, Jing L, Qian X. Reduced Graphene Oxide Grafted Ag_3PO_4 Composites with Efficient Photocatalytic Activity under Visible-Light Irradiation. *Ind. Eng. Chem. Res.*, **2014**, 53(21):8744–8752.

135. Bi Y, Hu H, Ouyang S, et al. Selective Growth of Metallic Ag Nanocrystals on Ag3PO4 Submicro-Cubes for Photocatalytic Applications. *Chem. Eur. J.*, **2012**, 18(45):14272-14275.

136. Wang J D, Liu J K, Luo C X, et al. Light-dependent controlled synthesis and photocatalytic properties of stable Ag 3, nanocrystals. *Mater. Res. Bull.*, **2014**, 60(1):783-793.

137. Yan T, Zhang H, Liu Y, et al. Fabrication of robust M/Ag3PO4 (M = Pt, Pd, Au) Schottky-type heterostructures for improved visible-light photocatalysis. *Rsc Adv.*, **2014**, 4(70):37220-37230.

138. Ying P X, Guo S W. Visible light responsive porous Lanthanum-doped Ag_3PO_4, photocatalyst with high photocatalytic water oxidation activity. *J. Colloid. Interf. Sci.*, **2014**, 430:1-5.

139. Yu H, Cao G, Chen F, et al. Enhanced photocatalytic performance of Ag_3PO_4, by simutaneous loading of Ag nanoparticles and Fe(III) cocatalyst. *Appl. Catal. B Environ.*, **2014**, s 160–161(1):658-665.

140. Li C, Long Q, Yin C. Synthesis and characterization of high photocatalytic activity and stable Ag_3PO_4/TiO_2, fibers for photocatalytic degradation of black liquor. *Appl. Surf. Sci.*, **2014**, 319(1):60-67.

141. Rawal S B, Sang D S, Wan I L. Novel Ag_3PO_4/TiO_2, composites for efficient decomposition of gaseous 2-propanol under visible-light irradiation. *Catal. Commun.*, **2012**, 17(1):131-135.

142. Teng W, Li X, Zhao Q, et al. Fabrication of $Ag/Ag_3PO_4/TiO_2$ heterostructure photoelectrodes for efficient decomposition of 2-chlorophenol under visible light irradiation. *J. Mater. Chem. A*, **2013**, 1(32):9060-9068.

143. Xu J W, Gao Z D, Han K, et al. Synthesis of magnetically separable $Ag_3PO_4/TiO_2/Fe_3O_4$ heterostructure with enhanced photocatalytic performance under visible light for photoinactivation of bacteria. *Acs Appl. Mater. Interf.*, **1944**, 6(17):15122.

144. Bi Y, Ouyang S, Cao J, et al. Facile synthesis of rhombic dodecahedral AgX/Ag_3PO_4 (X = Cl, Br, I) heterocrystals with enhanced photocatalytic properties and stabilities. *Phys. Chem. Chem. Phys.*, **2011**, 13(21):10071-10075.

145. Nagaveni K, Hegde M S, Ravishankar N, et al. Synthesis and Structure of Nanocrystalline TiO_2 with Lower Band Gap Showing High Photocatalytic Activity. *Langmuir*, **2004**, 20(7):2900-2907.

146. Li H, Wu T, Cai B, et al. Efficiently photocatalytic reduction of carcinogenic contaminant Cr (VI) upon robust AgCl/Ag hollow nanocrystals. *Appl. Catal. B Environ.*, **2015**, 164(17):344-351.

147. Zhang X, Liu J, Wang Y, et al. Synthesis,Photocatalytic Activity and Regeneration of AgBr/CuO Heterojunction Photocatalyst. *Chem. J. Chinese. U.*, **2016**.

148. Pan C S. New type of $BiPO_4$ oxy-acid salt photocatalyst with high photocatalytic activity on degradation of dye. *Environ. Sci. Technol.*, **2010**, 44(14):5570.

149. Chen L, Yin S F, Huang R, et al. Facile synthesis of BiOCl nano-flowers of narrow band gap and their visible-light-induced photocatalytic property. *Catal. Commun.*, **2012**, 23(21):54-57.

150. Ansari S A, Khan M M, Ansari M O, et al. Band gap engineering of CeO_2 nanostructure using an electrochemically active biofilm for visible light applications. *Rsc Adv.*, **2014**, 4(32):16782-16791.

151. Yamamoto T, Katayama-Yoshida H. Unipolarity of ZnO with a wide-band gap and its solution using codoping method. *J. Cryst. Growth.*, **2000**, s 214–215(00):552-555.

152. Guo J, Ouyang S, Zhou H, et al. $Ag_3PO_4/In(OH)_3$ Composite Photocatalysts with Adjustable Surface-Electric Property for Efficient Photodegradation of Organic Dyes under Simulated

Solar-Light Irradiation. *J. Phys. Chem. C*, **2013**, 117(34):17716–17724.

153. Guo J, Ouyang S, Li P, et al. A new heterojunction Ag_3PO_4/Cr-$SrTiO_3$, photocatalyst towards efficient elimination of gaseous organic pollutants under visible light irradiation. *Appl. Catal. B Environ.*, **2013**, s 134–135(s 134–135):286-292.

154. Lin T H, Chen T T, Cheng C L, et al. Selectively enhanced band gap emission in ZnO/Ag_2O nanocomposites. *Opt. Express.*, **2009**, 17(17):4342-4347.

155. Gonzálezborrero P P, Sato F, Medina A N, et al. Optical band-gap determination of nanostructured WO_3 film. *Appl. Phys. Lett.*, **2010**, 96(6):201.

156. Banerjee R, Jayakrishnan R, Banerjee R, et al. Effect of the size-induced structural transformation on the band gap in CdS nanoparticles. *J. Phys. Condens. Mat.*, **2000**, 12(50):10647.

157. Wang Y, Lopata K, Chambers S A, et al. Optical Absorption and Band Gap Reduction in $(Fe1–xCrx)_2O_3$ Solid Solutions: A First-Principles Study. *J. Phys. Chem. C*, **2015**, 117(48):25504–25512.

158. Li J, Liu X, Zhuo S, et al. Novel Bi_2MoO_6/TiO_2, heterostructure microspheres for degradation of benzene series compound under visible light irradiation. *J. Colloid. Interf. Sci.*, **2015**, 463:145-153.

159. Thalluri S M. Insights from crystal size and band gap on the catalytic activity of monoclinic $BiVO_4$. *Int. J. Chem. Eng. Appl.*, **2013**, 4(5).

160. Zamiri R, Ahangar H A, Zakaria A, et al. The structural and optical constants of Ag_2S semiconductor nanostructure in the Far-Infrared. *Chem. Cent. J.*, **2015**, 9(1):1-6.

161. Tang J, Gong W, Cai T, et al. Novel visible light responsive Ag@(Ag_2S/Ag_3PO_4) photocatalysts: synergistic effect between Ag and Ag_2S for their enhanced photocatalytic activity. *Rsc Advances*, **2013**, 3(8):2543-2547.

162. Li C, Zhang P, Lv R, et al. Photocatalysis: Selective Deposition of Ag_3PO_4 on Monoclinic $BiVO_4$ (040) plane for Highly Efficient Photocatalysis. *Small*, **2013**, 9(23):3951–3956.

163. Xu Y S, Zhang W D. Monodispersed Ag_3PO_4 nanocrystals loaded on the surface of spherical Bi_2MoO_6 with enhanced photocatalytic performance. *Dalton Transactions*, **2012**, 42(4):1094-1101.

164. Spadavecchia F, Cappelletti G, Ardizzone S, et al. Role of Pr on the Semiconductor Properties

of Nanotitania: An Experimental and First-Principles Investigation. *J. Phys. Chem. C*, **2012**, 116(43):23083.

165. Petritz R L. Theory of an Experiment for Measuring the Mobility and Density of Carriers in the Space-Charge Region of a Semiconductor Surface. *Phys. Rev.*, **1958**, 110(6):1254-1262.

166. Wu S, Zheng H, Wu Y, et al. Hydrothermal synthesis and visible light photocatalytic activity enhancement of $BiPO_4/Ag_3PO_4$, composites for degradation of typical dyes. *Ceram. Int.*, **2014**, 40(9):14613-14620.

167. Lin H, Ye H, Xu B, et al. Ag_3PO_4 quantum dot sensitized $BiPO_4$: A novel p–n, junction $Ag_3PO_4/BiPO_4$ with enhanced visible-light photocatalytic activity. *Catal. Commun.*, **2013**, 37(13):55-59.

168. Cao B, Dong P, Cao S, et al. $BiOCl/Ag_3PO_4$, Composites with Highly Enhanced Ultraviolet and Visible Light Photocatalytic Performances. *J. Am. Ceram. Soc.*, **2013**, 96(2):544–548.

169. Zhang J, Yu K, Yu Y, et al. Highly effective and stable Ag_3PO_4/WO_3 photocatalysts for visible light degradation of organic dyes. *J. Mol. Catal. A Chem.*, **2014**, 391(1):12-18.

170. Yun K J, Kim I Y, Lee J M, et al. Surface-anchored $CdS@Ag_3PO_4$, nanocomposite with efficient visible light photocatalytic activity. *Mater. Lett.*, **2014**, 114(1):152-155.

171. Yang Z M, Huang G F, Huang W Q, et al. Novel Ag_3PO_4/CeO_2 composite with high efficiency and stability for photocatalytic applications. *J. Mater. Chem. A*, **2013**, 2(6):1750-1756.

172. Zhang L, Zhang H, Huang H, et al. Ag_3PO_4/SnO_2 semiconductor nanocomposites with enhanced photocatalytic activity and stability. *New. J. Chem.*, **2012**, 36(8):1541-1544.

173. Yan Y, Guan H, Liu S, et al. Ag_3PO_4/Fe_2O_3, composite photocatalysts with an n–n heterojunction semiconductor structure under visible-light irradiation. *Ceram. Int.*, **2014**, 40(7):9095-9100.

174. Zhang S, Zheng M, Cao J, et al. Porous Carbon/Sulfur Composite Cathode Materials for Lithium-Sulfur Batteries. *Prog. Chem.*, **2016**.

175. Dyjak S, Kiciński W, Norek M, et al. Hierarchical, nanoporous graphenic carbon materials through an instant, self-sustaining magnesiothermic reduction. *Carbon*, **2016**, 96:937-946.

176. Xiang Q, Di L, Shen T, et al. Graphene-modified nanosized Ag_3PO_4, photocatalysts for enhanced visible-light photocatalytic activity and stability. *Appl. Catal. B Environ.*, **2015**, 162:196-203.

177. Yang X, Qin J, Jiang Y, et al. Bifunctional TiO_2/Ag_3PO_4/graphene composites with superior visible light photocatalytic performance and synergistic inactivation of bacteria. *Rsc Adv.*, **2014**, 4(36):18627.

178. Hou Y, Zuo F, Ma Q, et al. Ag_3PO_4 Oxygen Evolution Photocatalyst Employing Synergistic Action of Ag/AgBr Nanoparticles and Graphene Sheets. *J. Phys. Chem. C*, **2015**, 116(38):20132–20139.

179. Xu L, Huang W Q, Wang L L, et al. Mechanism of Superior Visible-Light Photocatalytic Activity and Stability of Hybrid Ag_3PO_4/Graphene Nanocomposite. *J. Phys. Chem. C*, **2014**, 118(24):12972–12979.

180. Chen G, Sun M, Wei Q, et al. Ag_3PO_4/graphene-oxide composite with remarkably enhanced visible-light-driven photocatalytic activity toward dyes in water. *J. Hazard. Mater.*, **2013**, 244-245(2):86.

181. Yang X, Qin J, Yan J, et al. Fabrication of P25/Ag_3PO_4 /graphene oxide heterostructures for enhanced solar photocatalytic degradation of organic pollutants and bacteria. *Appl. Catal. B Environ.*, **2015**, 166-167:231-240.

182. Chai B, Li J, Xu Q, et al. Facile synthesis of reduced graphene oxide/WO_3, nanoplates composites with enhanced photocatalytic activity. *Mater. Lett.*, **2014**, 120(120):177-181.

183. Xu H, Wang C, Song Y, et al. CNT/Ag_3PO_4, composites with highly enhanced visible light photocatalytic activity and stability. *Chem. Eng. J.*, **2014**, 241(4):35-42.

184. Wang Z, Lu Y, Zhang M, et al. Synthesis and characterization of Ag_3PO_4/multiwalled carbon nanotube composite photocatalyst with enhanced photocatalytic activity and stability under visible light. *J. Mater. Sci.*, **2014**, 49(4):1585-1593.

185. Tian J, Li H, Xing Z, et al. Facile synthesis of MWCNTs/Ag_3PO_4: novel photocatalysts with enhanced photocatalytic activity under visible light. *J. Nanopart. Res.*, **2013**, 15(3):1-7.

186. Liu B, Li Z, Xu S, et al. in situ synthesis of Ag@Ag_3PO_4/MWCNT triples hetero-photocatalyst for degradation of malachite green. *Mater. Lett.*, **2014**, 131(12):229-232.

187. Yang Y, Guo Y, Liu F, et al. Preparation and enhanced visible-light photocatalytic activity of silver deposited graphitic carbon nitride plasmonic photocatalyst. *Appl. Catal. B Environ.*, **2013**, s 142–143(2013):828-837.

188. Kumar S, Surendar T, Baruah A, et al. Synthesis of a novel and stable g-C_3N_4-Ag_3PO_4 hybrid

nanocomposite photocatalyst and study of the photocatalytic activity under visible light irradiation. *J. Mater. Chem. A*, **2013**, 1(17):5333-5340.

189. Zhang F J, Xie F Z, Zhu S F, et al. A novel photofunctional g-C_3N_4/Ag_3PO_4, bulk heterojunction for decolorization of RhB. *Chem. Eng. J.*, **2013**, 228(12):435-441.
190. Li L, Qi Y, Lu J, et al. A stable Ag_3PO_4@g-C_3N_4, hybrid core@shell composite with enhanced visible light photocatalytic degradation. *Appl. Catal. B Environ.*, **2016**, 183:133-141.
191. Bi Y, Ouyang S, Umezawa N, et al. Facet effect of single-crystalline Ag_3PO_4 sub-microcrystals on photocatalytic properties. *J. Am. Chem. Soc*., **2011**, 133(17): 6490-6492.
192. Mitoraj D, Kisch H. The Nature of nitrogen-modified titanium dioxide photocatalysts active in visible light. *Angew. Chem. Int. Edi*., **2008**, 47(51): 9975-9978.
193. Liang Q, Shi Y, Ma W, et al. Enhanced photocatalytic activity and structural stability by hybridizing Ag_3PO_4 nanospheres with graphene oxide sheets. *Phys. Chem. Chem. Phys*., **2012**, 14(45): 15657-15665.
194. Zhang L, Zhu Y, He Y, et al. Preparation and performances of mesoporous TiO_2 film photocatalyst supported on stainless steel. *Appl. Catal. B: Environ*., **2003**, 40(4): 287-292.
195. Borel J P, Châtelain A. Surface stress and surface tension: Equilibrium and pressure in small particles. *Surf. Sci.*, **1985**, 156(156):572-579.
196. Yildiz M, Dost S. Incorporation of surface tension to interface energy balance in crystal growth. *Cryst. Res. Technol.*, **2010**, 42(9):914-919.
197. Bi Y, Hu H, Ouyang S, et al. Selective growth of Ag_3PO_4 submicro-cubes on Ag nanowires to fabricate necklace-like heterostructures for photocatalytic applications. *J. Mater. Chem.*, **2012**, 22(30):14847-14850.
198. Chiou M S, Chuang G S. Competitive adsorption of dye metanil yellow and RB15 in acid solutions on chemically cross-linked chitosan beads. *Chemosphere*, **2006**, 62(5): 731-740.
199. Moon J, Yun C Y, Chung K W, et al. Photocatalytic activation of TiO_2 under visible light using Acid Red 44. *Catal. Today*, **2003**, 87(1): 77-86.
200. Song Z, Gao L, Li Q. Study on the surface status and agglomeration of TiO_2 nano-powder. *J. Inorg. Mater.*, **1997**, 33(9):1969-1969.
201. Guo C, Xu J, He Y, et al. Photodegradation of rhodamine B and methyl orange over one-dimensional TiO_2 catalysts under simulated solar irradiation. *Appl. Surf. Sci.*, **2011**,

257(8): 3798-3803.

202. Wongkalasin P, Chavadej S, Sreethawong T. Photocatalytic degradation of mixed azo dyes in aqueous wastewater using mesoporous-assembled TiO_2 nanocrystal synthesized by a modified sol–gel process. *Colloid. Surface. A*, **2011**, 384(1): 519-528.

203. Qian J, Liu P, Xiao Y, et al. TiO_2-coated multilayered SnO_2 hollow microspheres for dye-sensitized solar cells. *Adv. Mater.*, **2009**, 21(36): 3663-3667.

204. Bertelli M, Selli E. Kinetic analysis on the combined use of photocatalysis, H_2O_2 photolysis, and sonolysis in the degradation of methyl tert-butyl ether. *Appl. Catal. B- Environ.*, **2004**, 52(3): 205-212.

205. Davydov L, Smirniotis P G, Pratsinis S E. Novel differential reactor for the measurement of overall quantum yields. *Ind. Eng. Chem. Res.*, **1999**, 38(4): 1376-1383.

206. Davydov L, Reddy E P, France P, et al. Sonophotocatalytic destruction of organic contaminants in aqueous systems on TiO_2 powders. *Appl. Catal. B- Environ.*, **2001**, 32(1): 95-105.

207. Konstantinou I K, Albanis T A. TiO_2-assisted photocatalytic degradation of azo dyes in aqueous solution: kinetic and mechanistic investigations: a review. *Appl. Catal. B- Environ.*, **2004**, 49(1): 1-14.

208. Hachem C, Bocquillon F, Zahraa O, et al. Decolourization of textile industry wastewater by the photocatalytic degradation process. *Dyes Pigments*, **2001**, 49(2): 117-125.

209. Hirakawa T, Nosaka Y. Properties of $O_2^-$and OH formed in TiO_2 aqueous suspensions by photocatalytic reaction and the influence of H_2O_2 and some ions. *Langmuir*, **2002**, 18(8): 3247-3254.

210. Li G, Wong K H, Zhang X, et al. Degradation of Acid Orange 7 using magnetic AgBr under visible light: the roles of oxidizing species. *Chemosphere*, **2009**, 76(9): 1185-1191.

211. Cao J, Luo B, Lin H, et al. Visible light photocatalytic activity enhancement and mechanism of AgBr/Ag_3PO_4 hybrids for degradation of methyl orange. *J. Hazard. Mater.*, **2012**, 217: 107-115.

212. Devi L G, Kumar S G, Reddy K M, et al. Photo degradation of methyl orange an azo dye by advanced Fenton process using zero valent metallic iron: influence of various reaction parameters and its degradation mechanism. *J. Hazard. Mater.*, **2009**, 164(2): 459-467.

213. Faria P C, Orfão J J, Pereira M F. Adsorption of anionic and cationic dyes on activated carbons with different surface chemistries. *Water Research*, **2004**, 38(8):2043-2052.

214. Zheng Y, Wang W. Electrospun nanofibers of Er^{3+}-doped TiO_2 with photocatalytic activity beyond the absorption edge. *J. Solid. State. Chem.*, **2014**, 210(1): 206-212.

215. Lei P, Chen C, Yang J, et al. Degradation of dye pollutants by immobilized polyoxometalate with H_2O_2 under visible-light irradiation. *Environ. Sci. Technol.*, **2005**, 39(21): 8466-8474.

216. Matsuo S, Sakaguchi N, Yamada K, et al. Role in photocatalysis and coordination structure of metal ions adsorbed on titanium dioxide particles: a comparison between lanthanide and iron ions. *Appl. Surf. Sci.*, **2004**, 228(1): 233-244.

217. Wiszniowski J, Robert D, Surmacz-Gorska J, et al. Solar photocatalytic degradation of humic acids as a model of organic compounds of landfill leachate in pilot-plant experiments: influence of inorganic salts. *Appl. Catal. B: Environ.*, **2004**, 53(2): 127-137.

218. Muthukumar M, Selvakumar N. Studies on the effect of inorganic salts on decolouration of acid dye effluents by ozonation. *Dyes Pigments*, **2004**, 62(3): 221-228.

219. Guillard C, Lachheb H, Houas A, et al. Influence of chemical structure of dyes, of pH and of inorganic salts on their photocatalytic degradation by TiO_2 comparison of the efficiency of powder and supported TiO_2. *J. Photoch. Photobio. A*, **2003**, 158(1): 27-36.

220. Wang K H, Hsieh Y H, Wu C H, et al. The pH and anion effects on the heterogeneous photocatalytic degradation of o-methylbenzoic acid in TiO_2 aqueous suspension. *Chemosphere*, **2000**, 40(4): 389-394.

221. Piscopo A, Robert D, Weber J V. Influence of pH and chloride anion on the photocatalytic degradation of organic compounds: Part I. Effect on the benzamide and para-hydroxybenzoic acid in TiO_2 aqueous solution. *Appl. Catal. B: Environ.*, **2001**, 35(2): 117-124.

222. Ordal M A, Long L L, Bell R J, et al. Optical properties of the metals Al, Co, Cu, Au, Fe, Pb, Ni, Pd, Pt, Ag, Ti, and W in the infrared and far infrared. *Appl. Optics.*, **1983**, 22(7): 1099-1119.

223. Antonopoulou M, Giannakas A, Konstantinou I. Simultaneous Photocatalytic Reduction of Cr(VI) and Oxidation of Benzoic Acid in Aqueous N-F-Codoped TiO_2 Suspensions: Optimization and Modeling Using the Response Surface Methodology. *Int. J. Photoenergy*, **2012, 2012**(1):119-135.

224. Ssanyu G A, Schagerl M. Phytoplankton productivity in newly dug fish ponds within Lake Victoria wetlands (Uganda). *Afr. J. Environ. Sci. Technol.*, **2010**, 4(6):365-370.

225. Ge M, Zhu N, Zhao Y, et al. Sunlight-assisted degradation of dye pollutants in Ag_3PO_4 suspension. *Ind. Eng. Chem. Res.*, **2012**, 51(14): 5167-5173.

226. Homola J, Yee S S, Gauglitz G. Surface plasmon resonance sensors: review. *Sensor. Actuat. B: Chem*., **1999**, 54(1): 3-15.

227. Alvaro M, Carbonell E, García H. Photocatalytic degradation of sulphur-containing aromatic compounds in the presence of zeolite-bound 2, 4, 6-triphenylpyrylium and 2, 4, 6-triphenylthiapyrylium. *Appl. Catal. B: Environ*., **2004**, 51(3): 195-202.

228. Jiuhui Q U. Research progress of novel adsorption processes in water purification: A review. *J. Environ. Sci*., **2008**, 20(1): 1-13.

Appendices

Appendix A: Indoor weak light

The reaction process of indoor weak light degradation is conducted in a clean room with two 120×200 cm windows. A ventilator is used to ensure the air circulating of the room. The indoor weak light used in this work is entirely provided by natural light through the window glass, without any other artificial light source. The average light density of the indoor weak light is measured to be approximately 72 cd at daytime and 28 cd at night.

Appendix B: Physical Constants

h…….Planck Constant……..6.626176×10^{-34} J·s

E_g……Irregular Silver phosphate Band Gap……..2.44 eV

c……..Light Speed……299792 km·s^{-1}

N…….Avogadro constant…….6.022140857×10^{23} mol^{-1}